

# CFD-DEM Simulation of a Hot Melt Fluidized Bed Coating Process

Roland Kober, BSc

0273133



Roland Kober, BSc

# CFD-DEM Simulation of a Hot Melt Fluidized Bed Coating Process

## Masterarbeit

zur Erlangung des akademischen Grades eines

Diplom-Ingenieur

Verfahrenstechnik

eingereicht an der

Technischen Universität Graz

BetreuerIn:

Univ. -Prof. Dipl.-Ing. Dr.techn. Johannes Khinast<sup>a</sup>

Dipl.Ing Peter Böhling<sup>b</sup>

Dr. Sharareh Salar-Behzadi<sup>b</sup>

<sup>a</sup>Institute of Process and Particle Engineering, Graz University of Technology, Graz,  
Austria

<sup>b</sup>Research Center Pharmaceutical Engineering GmbH, Graz, Austria

Graz, June 2019



Deutsche Fassung:

Beschluss der Curricula-Kommission für Bachelor-, Master- und Diplomstudien vom 10.11.2008

Genehmigung des Senates am 1.12.2008

## EIDESSTATTLICHE ERKLÄRUNG

Ich erkläre an Eides statt, dass ich die vorliegende Arbeit selbstständig verfasst, andere als die angegebenen Quellen/Hilfsmittel nicht benutzt, und die den benutzten Quellen wörtlich und inhaltlich entnommenen Stellen als solche kenntlich gemacht habe.

Graz, am .....

.....

(Unterschrift)

Englische Fassung:

## STATUTORY DECLARATION

I declare that I have authored this thesis independently, that I have not used other than the declared sources / resources, and that I have explicitly marked all material which has been quoted either literally or by content from the used sources.

Graz, .....

.....

date

(signature)



## Abstract

In this work experiments on fluid bed hot melt coating process are performed and compared to a CFD-DEM simulation. The goal is to investigate the influence of particle temperature on the polymorphic behaviour of hot melt coat.

The hot melt coating studies are done using a fluid bed coater Ventilus V2.5 with around  $13 \cdot 10^6$  N-acetylcystein particles coated with Tristearin or a Tristearin-Polysorbate 65 mixture. The airflow temperature and flow rate are varied to understand the temperature influence of the polymorphic behaviour of Tristearin. Using pure Tristearin as coating material, the lipid was recrystallized in  $\alpha$ - and  $\beta$ -form by applying an inlet air temperature of 30 °C and 60°C, respectively. For the experiments with the mixture of Tristearin and Polysorbate 65 the transformation of  $\alpha$ - to  $\beta$ -form occurred immediately after recrystallization of lipid on the surface of particles and after coating process only  $\beta$ -form was detectable, which is due to the influence of the emulsifier Polysorbate 65.

With the temperature-crystal morphology correlation the CFD-DEM simulations are calculated to produce a system of particles that represent the needed particle surface temperature to obtain the same morphology results. 10 seconds of each experimental variation are performed. Start-up simulations with a cold geometry (30°C) and also in process simulations (geometry temperature matches particle temperature) were done. In all simulations the particle surface temperature was in a range to produce the former set crystal morphology.



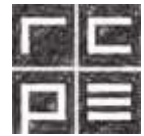
## Abstraktum

In dieser Arbeit werden ein Wirbelschicht Hot Melt Coating Prozess mit einer CFD-DEM Simulation verglichen. Das Ziel war den Einfluss der Partikeltemperatur auf die Kristallmorphologie zu untersuchen. Die Hot Melt Coating Versuche werden in einem Ventulus V2.5 Fluid Bed Coater mit zirka 13 Millionen Partikel durchgeführt. Die Partikel werden entweder mit Tristearin oder einer Mischung aus Tristearin und Polysorbate 65 gecoated. Die Temperatur der strömenden Luft und ihr Durchsatz werden variiert um den Einfluss auf die Kristallmorphologie zu verstehen. In den Versuchen mit reinem Tristerin wurden 2 Kristallformen festgestellt: Alpha Form bei Coatingversuche mit einer Zulufttemperatur von 30°C und Beta Form, wenn die Zulufttemperatur bei 60°C eingestellt war. Die Experimente mit der Tristearin-Polysorbate 65 Mixtur lieferten eine schnelle Transformation von Alpha Form in der Beta Form, was auf den Einfluss des Emulgators Polysorbate 65 zurückzuführen ist. Mit der Korrelation aus Kristallmorphologie und Temperatur wurden CFD-DEM Simulationen gemacht, die jene Bedingungen für die 2 Kristallformen bezüglich der Partikeloberflächentemperatur darstellen. Simulationen mit kalter Geometrie (30°C) also auch Simulationen mit der Geometrie in stationärem Zustand (30°C, 45°C, 60°C) wurden durchgeführt. Alle Simulationen konnten die Partikeloberflächentemperatur erreichen um die, im Experiment erhaltenen Kristallformen zu erzeugen.



<b>ABSTRACT</b>	<b>VII</b>
<b>ABSTRAKTUM</b>	<b>IX</b>
<b>1 INTRODUCTION</b>	<b>1</b>
<b>2 FLUIDIZED BED COATING</b>	<b>3</b>
2.1 CHARACTERIZATION OF THE STATE OF A FLUIDIZED BED	3
2.2 DESCRIPTION OF THE FLUID BED	7
2.2.1 ADVANTAGES OF FLUID BED SYSTEM	7
2.2.2 BATCH COATING OF POWDERS	8
2.3 OPTIMISATION OF THE COATING SYSTEM	9
2.3.1 DEFINITION OF PERFORMANCE CRITERIA	9
2.3.2 CHOOSING THE RIGHT TYPE OF FLUID BED METHOD FOR BATCH FLUID BEDS	10
<b>3 HOT MELT COATING</b>	<b>13</b>
3.1 PHYSIOCHEMICAL CHARACTERISATION AND FUNCTIONALITY OF HOT MELT COATING EXCIPIENTS	14
3.1.1 MOLECULAR WEIGHT	14
3.1.2 HYDROPHOBICITY	14
3.1.3 THERMAL BEHAVIOUR	15
3.1.4 ENTHALPY OF SOLIDIFICATION	15
3.1.5 RHEOLOGICAL BEHAVIOUR	16
3.1.6 EXPANSION CAPACITY	16
3.1.7 CHARACTERISATION OF COATED SUBSTANCES	16
3.1.8 PARTICLE SIZE	17
3.1.9 PARTICLE SHAPE	17
3.1.10 BULK DENSITY	17
3.1.11 SUBSTRATE STABILITY	17
3.1.12 POLYMORPHIC BEHAVIOUR	17
3.1.13 POLYMORPHIC BEHAVIOUR OF TRIACYLGLYCEROLS	18
<b>4 COMPUTATIONAL FLUID DYNAMICS</b>	<b>19</b>
4.1 PRINCIPLES OF FLUID DYNAMICS	19
4.2 IMPORTANT STEPS TO DEVELOP NUMERICAL SOLUTION METHODS	20
4.3 NAVIER-STOKES AND EULER EQUATIONS	21
4.4 DISCRETIZATION	22
4.4.1 FINITE DIFFERENCE METHOD	22
4.4.2 FINITE VOLUME METHOD	22
4.4.3 FINITE ELEMENT METHOD	23
4.4.4 USED DIFFERENCING SCHEMES	23
<b>5 DISCRETE ELEMENT METHOD</b>	<b>26</b>
5.1 INTRODUCTION	26
5.2 EQUATIONS AND FORCE MODELS	26
5.2.1 CONTACT FORCES	28
5.2.2 NON-CONTACT FORCES	29
5.2.3 PARTICLE-FLUID INTERACTIONS	31
<b>6 CFD-DEM MODELLING</b>	<b>33</b>
6.1 CONTINUOUS PHASE MODELLING	33
6.2 DISPERSE PHASE AND DRAG FORCE MODELLING	33
6.3 PARTICLE-PARTICLE & PARTICLE-WALL INTERACTION MODELS	35
6.3.1 LINEAR SPRING-DASHPOT	35

6.3.2	MEPA (MACROSCOPIC ELASTO-PLASTIC ADHESIVE) CONTACT MODEL	37
6.3.3	CFD-DEM COUPLING DATA MANAGEMENT	39
<b>7</b>	<b>MATERIALS AND METHODS</b>	<b>40</b>
<b>7.1</b>	<b>INNOJET VENTILUS 2.5 EQUIPPED WITH A HOT MELT DEVICE (ROMACO INNOJET, GERMANY)</b>	<b>40</b>
7.1.1	IHD HOT MELT DEVICE:	40
7.1.2	VENTILUS V-2.5/1 FLUID BED DEVICE:	40
7.1.3	PIPING & INSTRUMENTATION DIAGRAM (P&ID) INNOJET VENTILUS V-2.5/1	43
<b>7.2</b>	<b>ACTIVE PHARMACEUTICAL INGREDIENT (API)</b>	<b>44</b>
7.2.1	N-ACETYLCYSTEIN (NAC)	44
<b>7.3</b>	<b>EXCIPIENTS</b>	<b>44</b>
7.3.1	TRISTEARIN (DYNASAN 118)	44
7.3.2	POLYSORBAT 65 (TWEEN 65)	45
<b>7.4</b>	<b>EXPERIMENTAL METHODS</b>	<b>45</b>
7.4.1	HOT MELT COATING	45
<b>7.5</b>	<b>SIMULATION IN AVL FIRE® AND XPS</b>	<b>47</b>
<b>7.6</b>	<b>ANALYTICAL METHODS</b>	<b>48</b>
7.6.1	PARTICLE SIZE MEASUREMENT	48
7.6.2	SMALL ANGLE X-RAY SPECTROSCOPY (SAXS)	48
7.6.3	DIFFERENTIAL SCANNING CALORIMETRY (DSC)	48
7.6.4	DISSOLUTION	48
7.6.5	HIGH PRESSURE LIQUID CHROMATOGRAPHY (HPLC)	49
<b>8</b>	<b>RESULTS &amp; DISCUSSION</b>	<b>50</b>
<b>8.1</b>	<b>DSC AND WAXS MEASUREMENTS</b>	<b>50</b>
8.1.1	MODEL FIT: MORPHOLOGY	52
<b>8.2</b>	<b>DISSOLUTION</b>	<b>54</b>
8.2.1	MODEL FIT: TASTE MASKING AND IMMEDIATE RELEASE BEHAVIOUR	55
<b>8.3</b>	<b>CFD –SIMULATIONS</b>	<b>58</b>
<b>8.4</b>	<b>CFD-DEM COUPLED SIMULATIONS</b>	<b>59</b>
8.4.1	PARTICLE SIZE DISTRIBUTION	59
8.4.2	PARTICLE MEAN VELOCITY MAGNITUDE	60
8.4.3	MIXING RADIAL	61
8.4.4	MIXING AXIAL	64
8.4.5	INFLUENCE OF INITIAL AND AIRFLOW TEMPERATURE	67
8.4.6	PARTICLE COATING	72
<b>9</b>	<b>SUMMARY</b>	<b>77</b>
<b>10</b>	<b>OUTLOOK</b>	<b>78</b>
<b>11</b>	<b>LITERATURE</b>	<b>79</b>
<b>12</b>	<b>LIST OF FIGURES</b>	<b>83</b>
<b>13</b>	<b>APPENDIX</b>	<b>85</b>



## 1 Introduction

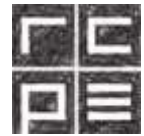
In the pharmaceutical industry coating is very important to mask the taste and odor, to improve the stability by preventing physical or chemical degradation due to environmental influences and providing controlled release of active substances (Teunou & Poncelet, 2001). Moreover physical properties like flowability, compressability, particle size and density can be improved (Dezarn, 1995). In the particle coating process solid particles are coated with a thin layer of polymer or with lipid-based excipients via film coating or hot melt coating, to change the upper mentioned properties (Teunou & Poncelet, 2001).

The main equipment in use are pan (or drum) coaters and fluidized bed coaters in various configurations, mostly in batch size. For pan coating the tablets are filled in a rotating drum. The rotational movement leads to radial and axial mixing. Due to the fact that the axial mixing is slower in pan coaters baffles are added to counteract this drawback. Drum coaters are mainly distinguished due to the airflow through the drum and baffle arrangement (Toschkoff & Khinast, 2013).

In a fluidized bed coater a mixture of solid particles is dispersed by gas flowing vertically or tangentially based on the configuration of base plate through the device. The advantages of particle fluidization are increased particle transport rates, good particle mixing and higher mass and heat exchange (Crow, 2006). Only in the last decade continuous coating processes are being introduced and explored to extinguish the disadvantages of the batch concept such as scale up problems and low production rate (Teunou & Poncelet, 2001).

For processes that involve particular matter it is of great interest to get a better understanding and insight of process, in order to further develop equipment design, process efficiency and the scale up process. With the advances in computational power and availability process modelling becomes common and an important tool to increase insight in these complex processes with the use of, for example Computational Fluid Dynamics (CFD), Finite Element Method (FEM), Discrete Element Method (DEM) etc.

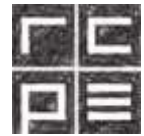
In Computational Fluid Dynamics (CFD) the main goal is to describe fluid motion by numerical solving of partial differential equations, which describe physical events like dissipation, diffusion, etc. The fluid is treated as a continuum and the CFD simulation



solves the mass-, momentum- and energy balances numerically (Eulerian approach) (Ketterhagen, Am Ende, & Hancock, 2008).

The partial differential equations to describe the previously mentioned balances (Conservation Laws) are mathematically characterized in the Navier Stokes equations (Lomax, Pulliam, & Zingg, 1999). The partial differential equations must be discretised to get a set of algebraic equations solved using a computer (Ferziger & Peric, 2002) In Discrete Element Method (DEM) the individual particle motion is calculated with the integration of Newton's Second law. Thereby the external forces (contact and non-contact forces) can be solved for every particle (so called Lagrangian approach) (Nakamura, Iwasaki, & Watano, 2006).

Furthermore for the combination (Euler-Lagrangian approach) of the individual particle motion and their interactions in DEM and the numerical method of CFD seems to be very promising due to the further rise in computational power. Due to the usage of Computer Unified Device Architecture (CUDA) it is possible to perform DEM-simulations with several million particles on a single Graphics Processor Unit (GPU). The CFD and DEM code are coupled together and the momentum, energy and mass transfer between the two phases (fluid and granular) are exchanged between two simulation time steps. (Jajcevic, Siegmann, Radeke, & Khinast, 2013)



## 2 Fluidized bed coating

In a Fluidized bed coater a mixture of solid particles is dispersed by gas flowing vertically or tangentially based on the configuration of base plate through the device. Using perforated base plates, when the gas velocity is increased a change of the fluidization regime within the bed can be observed. The particle bed starts as a fixed bed and while gas velocity is increased it changes to a bubbling and later on to a conveying regime. The advantages of particle fluidization are increased particle transport rates, better particle mixing and higher mass and heat exchange. Fluidized bed reactors are used in industry applications like chemical, food and pharmaceutical production, as well as in energy applications, like fluidized bed combustion (Lyngfelt, Leckner, & Mattisson, 2000).

### 2.1 Characterization of the state of a fluidized bed

One of the first classification schemes for characterisation of particle flow is the Geldart chart, as seen in Figure 1. It refers to four different groups of particle behaviour at standard conditions (20°C & 1bar):

- A (Aeratable): e.g. heterogeneous solid catalyst; excellent fluidization behaviour, small bubble, slowly deaerating (when gas flow is stopped), high bed expansion, rapid particle mixing
- B (Bubbles immediately): e.g. sand; deaerate fast after gas is stopped, large bubbles, intermediate solid mixing
- C (Cohesive): e.g. flour; poorly fluidizable due to strong inter-particle forces
- D (Dominantly inertial): e.g. peas; deaerate fast after gas is stopped, large bubbles, poor solid mixing

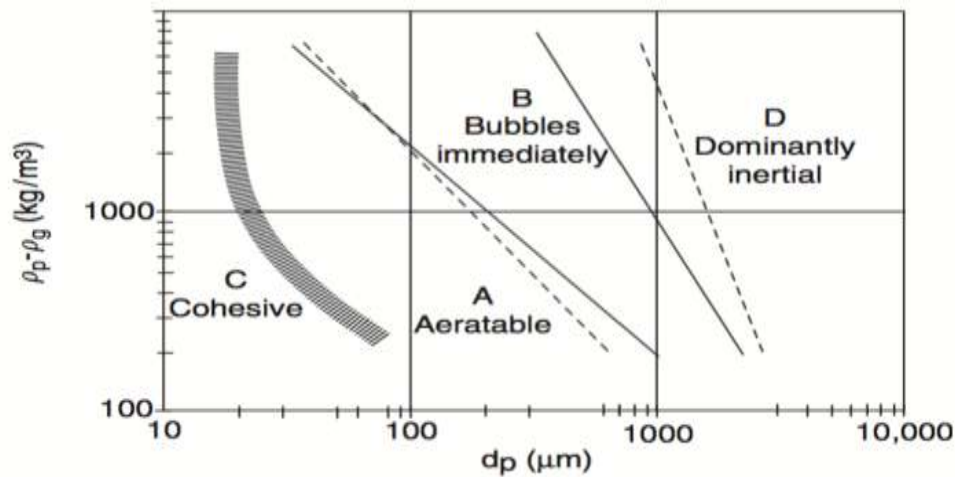
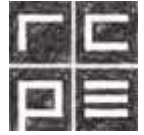


Figure 1: Geldart chart for characterization of particle fluidization behaviour in the 4 groups A, B, C, D. With the particle diameter [ $d_p$ ] ( $\mu\text{m}$ ) on the x-axis and the density difference between particle  $\rho_p$  and gas [ $\rho_{pg}$ ] ( $\text{kg}/\text{m}^3$ ) (Crow, 2006)

The extension of the Geldart classification is the “Grace Chart” (Figure 2). It covers gases other than air and temperatures and pressures other than the standard conditions. In this chart the dimensionless quantities  $U^*$  and  $d_p^*$  are plotted against each other. The dimensionless velocity  $U^*$  describes the fluid capability to lift particles in the fluidized bed.  $d_p^*$  can be determined as the cube root of  $Ar$  (Archimedes number).  $U^*$  depends on the fluid velocity  $U_0$ , the fluid density  $\rho_f$ , the particle density  $\rho_p$  and the fluid viscosity  $\mu_f$

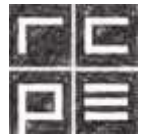
$$U^* = \sqrt[3]{\frac{\rho_f^2}{(\rho_p - \rho_f) \cdot g \cdot \mu_f}} \cdot U_0 \quad (1)$$

with

$$U_0 = \frac{\dot{V}_f}{A_{\text{cross}}} \quad (2)$$

as the superficial fluid velocity is defined by the fluid flow rate  $\dot{V}_f$  divided by the cross-sectional area of the fluidized bed  $A_{\text{cross}}$ .

- Archimedes number:



$$Ar = \frac{g \cdot \rho_g \cdot (\rho_p - \rho_g) \cdot d_v^3}{\mu_f^2} \tag{3}$$

The Archimedes number  $Ar$  is the ratio of lift force to friction force (Crow, 2006).

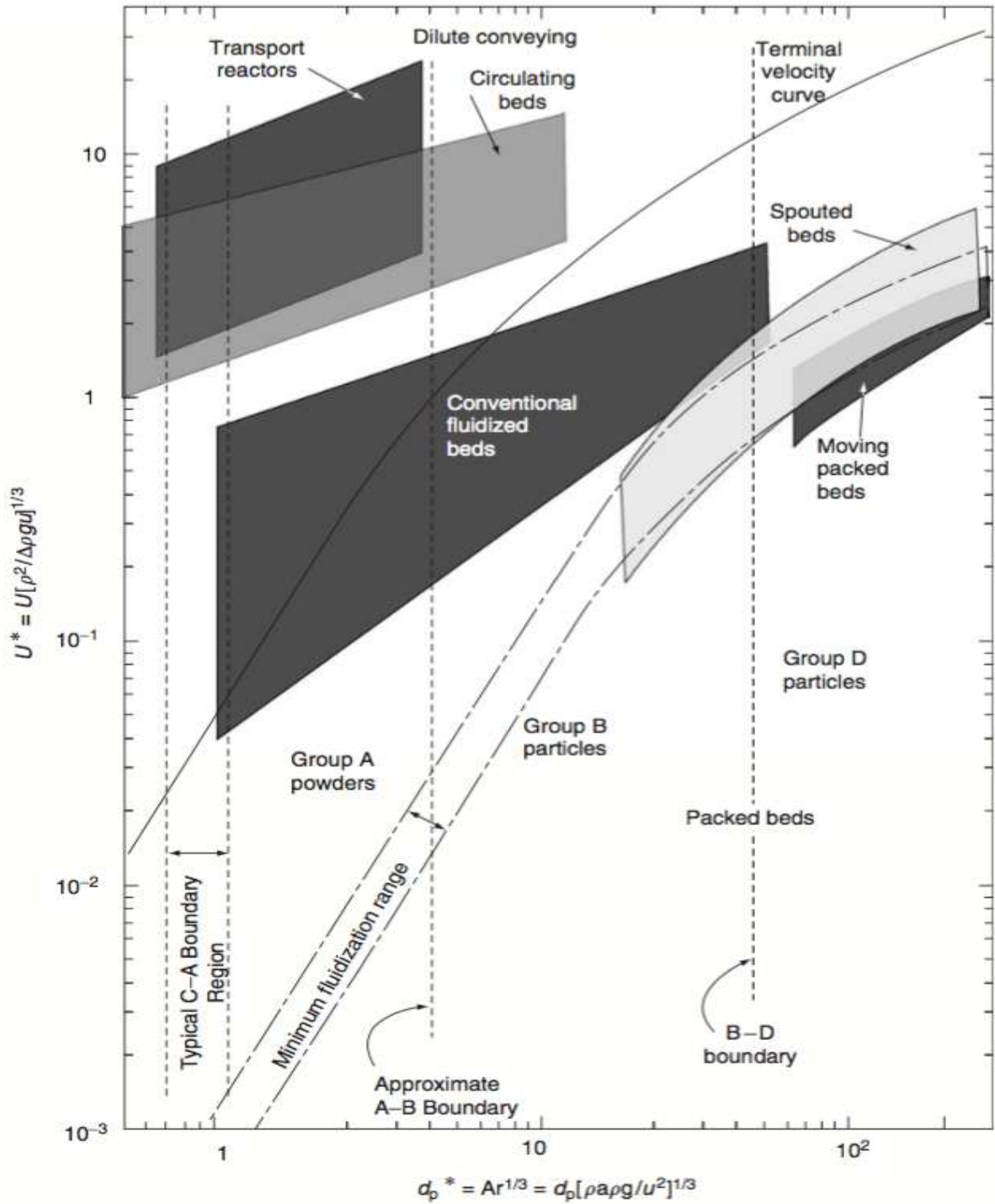
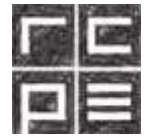


Figure 2: Dimensionless Grace chart for upward flow regime through solid particles to characterize the state of a fluidized bed (Crow, 2006)



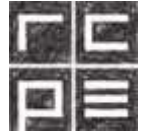
In Table 1 the desirable properties for particles and gases for fluidization are shown.

**Table 1: Desirable properties for particles and gases for fluidization (Crow, 2006)**

Property	Desirable Range	Comments
<b>Particle Properties</b>		
<b>Mean diameter</b> <sup>a</sup>	50 μm - 1,6 mm	Finer particles are too cohesive; coarser ones have less desirable fluidization properties
<b>Size distribution</b> <sup>b</sup>	Neither too narrow nor too broad	Too narrow gives bad fluidisation properties; too broad may lead to segregation
<b>Density</b>	Uniform from particle to particle	Large density differences may cause segregation, very low density materials (<500kg/m <sup>3</sup> ) may be difficult to retain in the bed
<b>Shape</b>	Rounded and with length to thickness ratio smaller than 3	Disks and needles inhibit fluidisation; sharp corners and edges cause excessive wear of surfaces
<b>Surface roughness</b>	Smooth	Some roughness is tolerable
<b>Surface stickiness</b>	Avoid sticky surfaces	Sticky surfaces cause agglomeration and fouling
<b>Attrition resistance</b>	As strong as possible	Particles need to withstand the stresses in the particle bed over a couple of hours
<b>Hardness</b>	Avoid resilience, but also excessive hardness	Compressible particles give excessive inter particle forces; very hard ones tend to cause wear of surfaces and equipment
<b>Gas Properties</b>		
<b>Density</b>	No restriction, but higher values improve properties	High pressure results in improved fluidization characteristics
<b>Viscosity</b>	No restriction	
<b>Relative humidity</b>	Typically between 10 and 90%	Below 10% electrostatics may be excessive and above 90% capillary forces tend to be dominant

<sup>a</sup> The mean diameter is conventionally defined as  $1 / \sum \frac{x_i}{d_{pi}}$ .  $x_i$  is the mass fraction of particles of the mean size  $d_{pi}$ , usually obtained from arithmetic average sieve opening in a sieve analysis.

<sup>b</sup> Note that the size distribution in the bed at any point will, in general, differ from the feed or original size distribution due to such factors as attrition, elutriation and agglomeration.



## 2.2 Description of the fluid bed

As described above, the state of the fluidized bed is a function of air velocity and powder properties. The two most important gas velocities for a fluidized bed are the minimum fluidization velocity [ $U_{mf}$ ] (m/s) and the terminal settling velocity [ $U_t$ ] (m/s). The minimum fluidization velocity leads to a stable flowing fluidized bed and is used for unit operations such as drying, coating, agglomeration, etc.

$$U_{mf} = \left\{ \begin{array}{l} \frac{(\rho_p - \rho_g)^{0,934} \cdot g^{0,934} \cdot d_p^{1,8}}{111 \cdot \mu_g^{0,87} \cdot \rho_g^{0,066}}, \text{ for } d_p < 100 \mu\text{m} \\ \frac{\mu_g}{\rho_g \cdot d_v} \cdot \left[ (1135,7 + 0,0408 * Ar)^{\frac{1}{2}} - 33,7 \right], \text{ for } d_p > 100 \mu\text{m} \end{array} \right\} \quad (4)$$

with [ $\rho_p$ ] & [ $\rho_g$ ] (kg/m<sup>3</sup>) the density of the particles respectively the gas, [ $g$ ] (m/s<sup>2</sup>) is the gravitational constant, [ $\mu_g$ ] ( $\frac{kg}{m \cdot s}$ ) the dynamic viscosity of the gas, [ $d_p$ ] (m) is the particle diameter and [ $d_v$ ] (m) is the diameter of the equivalent sphere. Further the dimensionless Archimedes Number (Ar) is calculated as follows:

$$Ar = \frac{\rho_g \cdot d_v^3 \cdot (\rho_p - \rho_g) \cdot g}{\mu_g^2} \quad (5)$$

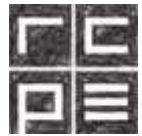
The thermal settling velocity  $U_t$  is the gas velocity at which dragging or transport of particles (e.g. pneumatic conveying) starts.

$$U_t = \sqrt{\frac{4 * g * d_p * (\rho_p - \rho_g)}{3 * \rho_g * C_D}} \quad (6)$$

$C_D$  is the so-called Drag coefficient and is a correlated function of the particle Reynolds number  $Re_p$ . Correlations can be found in (Morrison, 2016).

### 2.2.1 Advantages of fluid bed system

The fluid bed is a very complex unit operation, due to the complexity (or impossibility) of the description of the trajectories of the single moving particles in the bed. The advantages of a fluid bed process are the limited pressure drop, the temperature



homogeneity, good heat and mass transfer and an easy control of the flow rate and reaction kinetics.

### 2.2.2 Batch coating of powders

In Figure 3 the principal process of fluidizing and coating of particles is shown. The batch reactor is filled with particles and they are fluidized with air. The coating material is molten or dissolved/dispersed in liquid and the liquid is pumped into a spraying nozzle. The coating liquid is sprayed on the particles to produce a homogenous layer of coating material. As long as the material is still wet, there is a tendency to agglomerate. There is always a competition between forming a layer on the particles and agglomeration of wetted particles.

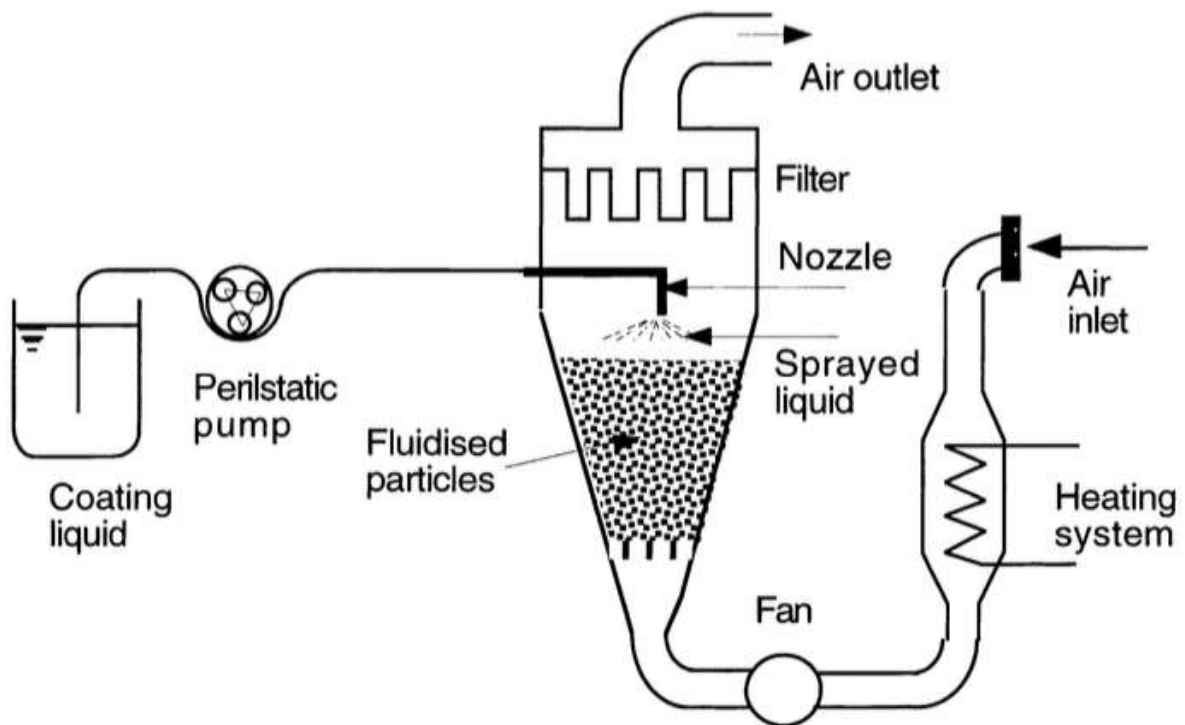
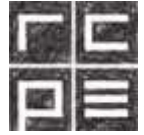


Figure 3: Principal scheme of a fluid bed coating process with a top spray nozzle (Teunou & Poncelet, 2002)

A coating process is the interaction between the three present phases in the fluidized bed. These phases are: solid (particles), liquid (coating material), gas (fluidizing air). In the following the events of a coating process are classified chronologically, but one has to take into account, that some of these events happen simultaneously.



- Air suspension of the particles in the coating chamber
- Spraying of liquid coating material as fine dispersed droplets with the aim that the droplets reach the particle before spray drying occurs
- Cover of the particle surface with droplets. The droplets adhere on the surface and flatten. In the best case the droplets form a continuous layer on the particle before drying.
- Last step is the layering or superposition of different layers on the particle surface to form a homogenous coating. After some cycles of wetting and drying a continuous film should have been formed on the particle surface with known thickness and composition. At this stage agglomeration happens with the highest possibility.

The success of the coating process is always a function of the wettability of the particles by the used coating material because only a homogenous covering of particle surface can be counted as a successful coating operation. To characterize the wettability of the particles and the strength of the bond between the coated particles the contact angle of the three-phase system (solid-liquid-gas) is used. The angle is a function of the chemical and physical properties of the coating material and the particle surface in the presence of air (such as surface tension between three phases, hygroscopicity, surface energy and roughness of particles). With some assumptions made (flat, homogenous, spherical surface), the wetting coefficient  $[Wm]$  (J) is introduced.

$$Wm = \gamma_{sv} - \gamma_{lv} - \gamma_{sl} \quad (7)$$

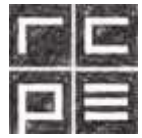
$[\gamma_{sv}]$  (J) is the interfacial tension between solid and vapour,  $[\gamma_{lv}]$  (J) is interfacial tension between liquid and vapour,  $[\gamma_{sl}]$  (J) interfacial tension between solid and liquid. If  $Wm > 0$  than a liquid can wet a surface.

## 2.3 Optimisation of the coating system

In the next few chapters some ways are introduced to improve the given coating system.

### 2.3.1 Definition of performance criteria

In general the performance is defined via the dimensionless coating efficiency  $E_c$ .



$$E_c = \frac{W_c}{W_{cs} \cdot Dm} \quad (8)$$

with

$$W_c = W_p \frac{w}{1 - w} \quad (9)$$

$W_c$  is the deposited mass of coating in kg,  $w$  is the coating content of the capsule in (kg/kg),  $W_p$  is the mass of the core material in kg,  $W_{cs}$  is the mass of the coating solution in kg and  $Dm$  is the dry matter content of the coating solution in (kg/kg).

The problem with using the coating efficiency  $E_c$  is, that there is no information about the energy balance and also no information about the quality of the resulting encapsulation. There are suggestions of introducing at least 4 efficiencies to characterize the performance of the coating operation.

1. The already mentioned coating efficiency  $E_c$ .
2. The energy efficiency  $E_e$ .
3. Next is the quality efficiency  $E_q$  whose definition cannot be generalised since it is related to a required property.
4. The product efficiency  $E_p$  that is the total amount of coated material per hours. This is the most important criterion for industrial application and scale up.

### 2.3.2 Choosing the right type of fluid bed method for batch fluid beds

There are 4 important types of fluid bed processes; shown in Figure 4 below.

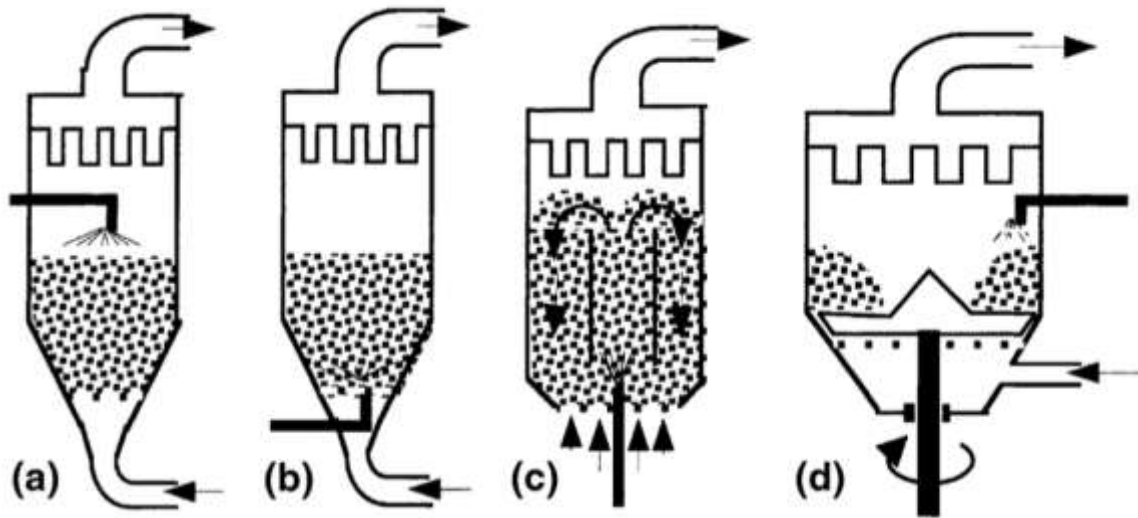
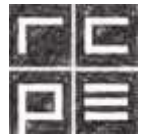
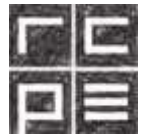


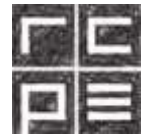
Figure 4: The 4 different types of batch fluid beds: (a) top spray; (b) bottom spray; (c) wurster; (d) rotor with side spray (Teunou & Poncelet, 2002)

- Top spray coaters: As seen in Figure 4 the spray nozzle is installed at the upper part of the process chamber, above the fluidized bed. The liquid is sprayed counter-currently onto the fluidized particles. Conventionally, a perforated base plate is used. The downside is that the particles are not coated homogeneously, which leads to problems with the controlled release of active pharmaceutical ingredient(s) (API).
- Bottom spray coaters: The nozzle is installed at the bottom of the processing chamber and sprays upwards, concurrently into the fluidized bed. A perforated base plate is also commonly used for bottom spray method. The collision between liquid droplets and particles are considerably higher than in the top spray coater. So the coating efficiency  $E_c$  (8) is higher. It is suitable for tablet coating but for very small particles the agglomeration rate is high due to the large number of wetted particles.
- Wurster system or insert bottom spray coater: In this method a small inner column (the so-called Wurster) is mounted above an upwards-directed nozzle. The perforations in the base plate are larger in the centre, smaller towards the periphery and larger again along the outermost circle. This arrangement facilitates a strong air stream and an upwards-directed core movement inside the Wurster. Due to the circulation of the particles the drying rate increases and the potential of agglomeration is reduced. Furthermore the coating quality (smooth



and continuous coating of the particles) is increased. Because of the decreased agglomeration possibility, the Wurster coater can be used for various particle sizes to form coated particles with good control release characteristics.

- Rotor system: In this system particles become a rotating movement due to the special design of the base plate and the resulting airflow. This provides higher spherical shape and density on the resulting coated particles. The quality is similar to the Wurster system but due to the high agitation coating materials that are too crumbly cannot be used. (Teunou & Poncelet, 2002)



### 3 Hot melt coating

The main advantage of hot melt coating is that no solvent is needed to get the coating material in liquid form. The coating material is a lipid or lipid-based excipient, which is sprayed on the surface of feed particles in the molten state. The lipid is resolidified on the surface of particles in the process chamber and provide the coating. This solvent-free technique reduces processing times significantly. Furthermore hot melt coating is more environmentally friendly than common coating methods with aqueous or organic solvents because no treatment after coating process (e.g. solvent evaporation) needs to be done. Organic solvents need treatment after the evaporation because of environmental regulations and are more expensive than water based solvents (Hinkes, 1978). Also the weight gain decreases with lipid-based materials when compared to commonly used polymer coatings. Moreover lipid based coatings are inexpensive and widely available, which makes it cost efficient.

Disadvantages include the high temperatures of up to 200°C for melting the lipid, which is a possible concern for safety reasons and possible physical or chemical degradation of the active ingredient (Achanta, Adusumilli, James, & Rhodes, 1997).

Requirements and examples for coating materials used in hot melt coating

- No physical or chemical change of lipid at temperatures close to 200°C
- The transition from solid to molten liquid should be in a narrow range and there should be relatively no softening before melting
- In the range between 30-200°C the thermal behaviour of lipid should be independent from the permeation, storage conditions and thermal history
- It should stay stable even when under repeated heating-cooling cycles
- Availability in varying hydrophilic-lipophilic balance (HLB) values.
- It should be easy to spray with good spraying characteristics
- Not toxic and approved for the use in pharmaceuticals

(Achanta, Adusumilli, James, & Rhodes, 1997)

In Table 2 a summary of interesting excipients is listed with their chemical composition, their properties, the functionality and some examples in which form they are available



in nature.

**Table 2: Examples of lipid excipients (Jannin & Cuppok, 2012)**

<b>Excipients</b>	<b>Chemical composition</b>	<b>Properties &amp; Melting Range (MR)</b>	<b>Functionality</b>	<b>Examples</b>
<b>Waxes</b>	Esters of fatty acids and long chain alcohols	Hydrophobic; MR=62-86°	Prolonged release	Carnauba wax, beeswax
<b>Vegetable oils</b>	Mix of triglycerides, free fatty acids and phospholipids	Mostly digestible; MR=60-71°C	Prolonged release Taste masking	Hydrogenated cottonseed oil, hydrogenated palm oil
<b>Polyoxy-glycerides</b>	Mix of glycerides, esters of fatty acid and polyethyleneglycol	Partially digestible; Melting Point =50°C	Prolonged release Immediate release	Stearoyl polyoxyl-6 glycerides
<b>Fatty acids</b>	Long chain fatty acids	MR=60-90°C	Prolonged release	Palmitic acid, stearic acid
<b>Partial glycerides</b>	Mix of mono-, di- and triglycerides	MR=54-74°C	Prolonged release Taste masking Lubrication	Glyceryl palmitostearate
<b>Animal fats</b>	Clarified butter	Melting Point=80°C	Prolonged release	Cow ghee

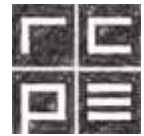
### 3.1 Physiochemical characterisation and functionality of hot melt coating excipients

#### 3.1.1 Molecular weight

Molecular weight is one of the most important physiochemical parameters as it can provide information about the strength, flexibility and rheological behaviour of a material and even about the ability of retarded drug release. The techniques which are used for determination of the molecular weight of fats and oils with size-exclusion chromatography were reported by (Hussain, Sastry, & Raju, 1991).

#### 3.1.2 Hydrophobicity

The hydrophobicity in glycerides is influenced by the amount of fatty acids because of their proponent weight. The hydrophobicity of glyceride is limited by the hydrophobic character of the fatty acid (Sonntag, 1979). The hydrophobicity is measured via the



contact angle between the surface of a lipid coating and a droplet of water. The hydrophobicity is an important parameter, because the drug release rate decreases with increasing hydrophobicity of the used lipid. (Jannin & Cuppok, 2012)

### 3.1.3 Thermal behaviour

Furthermore it is important to know the thermal behaviour of the materials in use, because hot melt coating requires higher temperatures about 20 °C above the melting point of used lipids. There are 3 important effects, which need to be determined before a hot melt coating can take place (Achanta, Adusumilli, James, & Rhodes, 1997).

- Physiochemical interactions between drug and excipient
- The ability of the excipient to influence drug release
- Stability of the dosage form

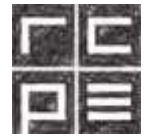
If waxes are used for the coating process, it's always important to know, that these are non homogenous in chemical composition and tend to have a melting range instead of a fixed melting point. For glycerides the melting range is dependent on the hydroxyl number, the degree of unsaturation and the molecular weight.

To determine the thermal behaviour of lipid excipients differential scanning calorimetry (DSC) is the most commonly used technique. The melting and solidification point, the phase transition temperature und the solid liquid ratio can be determined. To get insight in the polymorphic behaviour X-ray diffraction (XRD) can be coupled with DSC. (Sudke & Sakarakar, 2013)

### 3.1.4 Enthalpy of solidification

This is the amount of energy that is exothermally released when a liquid substance solidifies. During the crystallisation the temperature stays constant until all the whole system is solid, only after that the temperature starts to decrease again. The reversed process happens, when a solid substance is melt. The temperature stays the same until everything is molten and then increases again (Correns, 1949)

The enthalpy of solidification is the exothermic enthalpy of fusion (also called latent heat of fusion [H] (J)).



$$\Delta H_{fusion} = -\Delta H_{solidification} \quad (10)$$

(Atkins & Jones, 2010)

### 3.1.5 Rheological behaviour

The rheological behaviour of a molten solid is a function of temperature. This has to be evaluated to make sure the viscosity of the molten substance is low enough to provide continuous flow through the pump and the nozzle (Jannin & Cuppok, 2012). As (Bose & Bogner, 2007) suggest, the viscosity of the molten lipid should be at most 300 (*m Pa s*) at 80°C.

### 3.1.6 Expansion capacity

Glycerides tend to expand during melting and contract during crystallization. The quality of the coating layer is dependent on the spreading of the lipid droplets on the used substrate, which for itself is depending on the capacity of the lipid to expand and contract during melting and cooling (Jannin & Cuppok, 2012). Possible measurement methods include dilatometry and NMR (nuclear magnetic resonance) instrumentation. For NMR in-line techniques were developed to characterize the products and the optimization of the reaction conditions in real-time (Sans, 2015). There is motivation to make on-line dilatometry possible, like in the study for expansion coefficients of metals (Coupland, 2001) but there was no development in recent years.

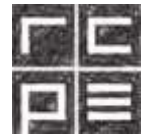
### 3.1.7 Characterisation of coated substances

There are many different substances, which have been coated in a hot melt coating process.

Pellets: Bromhexine hydrochloride, Salbutamol sulphate (Patil, Chafle, Khobragade, Umathe, & Avari, 2011)

Powders: Cefuroxime Axetil (Kulah & Kaya, 2010); citric acid, sodium- and potassium chloride (Jones & Percel, 1994)

Granulation: Urea (Villa, Bertin, Cotabarren, Pina, & Bucala, 2016), glass ballotini and lactose seeds (Seo, Holm, & Schaefer, 2002) (Tan, Salman, & Hounslow, 2006) for hot melt granulation.



### 3.1.8 Particle size

It is very important to keep the particle distribution as narrow as possible to avoid adhesion of small and large particles.

To measure particle size sieving can be a good method, but it tends to underestimate the size distribution for needle shaped particles and in case of very small particles they tend to block the sieve. So for very small particles like fine powders laser diffraction is a possible measurement method.

For different particle sizes different kinds of fluidized bed coaters are used. For large particles and pellets coated in a hot melt process ( $>500 \mu\text{m}$ ) a bottom-spray coater can be used. If a top-spray coater is used, the particles should be larger than  $100 \mu\text{m}$ . (Jannin & Cuppok, 2012).

### 3.1.9 Particle shape

Like in every particular application the best particles for experiments and simulation are smooth and spherical substances. With these a homogenous coating thickness can be achieved even in reproduced experiments, which is the most important thing for the validation of experimental results. Often, granulation or pelletisation is done before the coating process, to ensure the best shape possible for the used material (Jones & Percel, 1994).

### 3.1.10 Bulk density

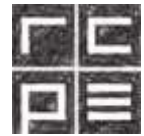
The bulk density should not be lower than  $0.5 \text{ g/ml}$  because these may be drawn directly into the filter before fluidization occurs and not higher than  $1 \text{ g/ml}$  because a sufficient fluidization of the whole bulk would be nearly impossible (Jannin & Cuppok, 2012).

### 3.1.11 Substrate stability

Due to the high temperatures used in hot melt coating, the material should not change crystalline form, crumble or melt at temperatures under  $80^\circ\text{C}$  (Jannin & Cuppok, 2012).

### 3.1.12 Polymorphic behaviour

Glyceride shows different polymorphic transition temperatures and melting ranges at different crystal structures (hexagonal, orthomorph, triclinic) (Brubach, Jannin,



Mahler, Bourgaux, Lesieur, & Roy, 2004).

### 3.1.13 Polymorphic behaviour of Triacylglycerols

There are 3 fundamental polymorphs for the majority of triacylglycerols and their derivatives. These are defined by the molecular packing in the crystal lattice: hexagonal ( $\alpha$ ), orthorhombic-perpendicular ( $\beta'$ ) and triclinic-parallel ( $\beta$ ). The different crystal lattice forms are shown in Figure 5. The lattice structure is identified with different analytical methods, for example X-ray diffraction, microscopy, DSC, etc. With wide-angle x-ray scattering (WAXS) the short spacing distances can be measured, which are characteristic for the different crystal lattice forms. Further with DSC the morphology can be detected due to different melting behaviours of the crystal forms. Most of the triacylglycerols follow the Ostwald step rule, which implies that the less stable polymorphic form ( $\alpha$ ) crystallizes faster than the more stable ones ( $\beta'$  and  $\beta$ ). The driving forces in crystallization are supersaturation and supercooling. After the crystallization the triacylglycerols transform from the least stable ( $\alpha$ ) to the most stable form ( $\beta$ ). The polymorphic stabilization causes a flake-like surface structure, which increases the surface area and forms water-repellent surfaces. Due to the change of the surface the dissolution rate changes. In literature there is a disagreement on how it affects the dissolution rate. It is reported, that the drug release is slower after storage due to the super water repellent surface but there are also reports of formulations that were significantly faster dissolving which was explained with the tortuosity that increased with the polymorphic transformation. (Lopes, et al., 2015)

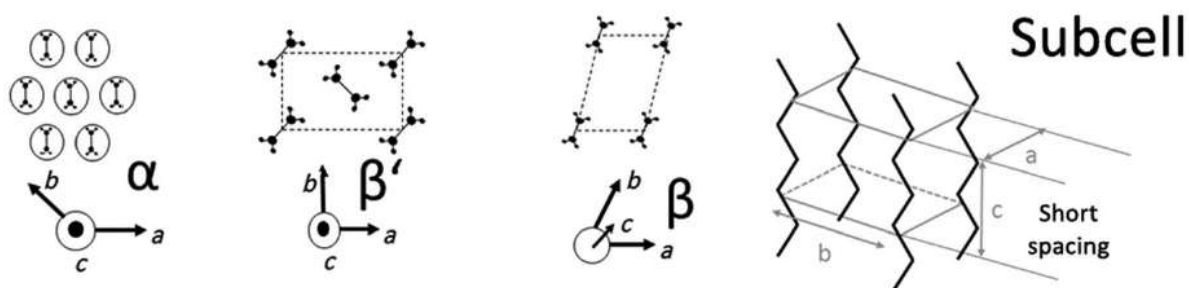
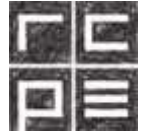


Figure 5: hexagonal ( $\alpha$ ), orthorhombic-perpendicular ( $\beta'$ ) and triclinic-parallel ( $\beta$ ) crystal lattice and a subcell to visualize the short spacing. (Modified from (Lopes, et al., 2015))



## 4 Computational Fluid Dynamics

This chapter will give a short introduction to Computational Fluid Dynamics (CFD). The main goal of CFD is to numerically solve partial differential equations describing the physics of a fluid flow. To get the solution of differential equations a system of algebraic equations with different discretization methods has to be approximated, in a way a computer is able to solve it. Fluid is a collective name for liquids and gases and means substances whose molecular structure offers no resistance to external shear forces. For liquids and gases, the same laws of motion can be applied. The motion in fluids is normally due to external applied forces like pressure difference, gravity, rotation or surface tension (Ferziger & Peric, 2002). Furthermore, the fluid can be regarded as a continuum, because there are a very huge number of molecules per cubic millimetre ( $10^{18}$  molecules per  $\text{mm}^3$  for gases and  $10^{21}$  molecules per  $\text{mm}^3$  for liquids). In the continuum the characteristics (density, pressure, velocity, etc.) vary throughout the fluid. So a fluid flow characteristic like velocity is averaged over a small volume with a still large number of molecules and very small spacing between. (Munson, Okiishi, Huebsch, & Rothmayer, 2013). Lomax et al., describe the goal of CFD in their book as:

*“The ultimate goal of the field of computational fluid dynamics (CFD) is to understand the physical events that occur in the flows of fluids around or within designated objects”.*

By physical events they mean interaction phenomena like dissipation, diffusion, convection, etc. These are mathematically described in the compressible Navier-Stokes-Equations. Most of these are nonlinear effects and therefore have no analytical solution and need to be solved numerically and that is where CFD becomes part of the game. (Lomax, Pulliam, & Zingg, 1999)

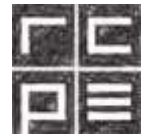
### 4.1 Principles of Fluid Dynamics

- The conservation of mass:

$$\frac{dm}{dt} = 0 \quad (11)$$

- The conservation of momentum:

$$\frac{d(m \cdot v)}{dt} = \sum F \quad (12)$$



t is time, m is mass, v is velocity and F is forces acting on the control mass (gravity, etc.) (Munson, Okiishi, Huebsch, & Rothmayer, 2013).

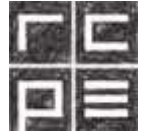
- First law of thermodynamics: Conservation of Energy, which means that energy cannot be created or destroyed, it can only change its form (internal energy of a system is constant).

$$E_{in} - E_{out} = \Delta E \quad (13)$$

- Second law of thermodynamics: Energy processes only happen in the direction of decreasing quality of energy. Some things cannot happen even if they would be possible under the first law, like a heat flowing from low to high temperatures. (Çengel & Boles, 2014).

#### 4.2 Important steps to develop numerical solution methods

- Mathematical Models: First of all, the set of partial differential equations and the boundary conditions have to be chosen. Assumptions like incompressible and/or inviscid flow, turbulent flow, 2 or 3 dimensions, etc. These may simplify the conservation laws.
- Discretization Methods: The differential equations need to be approximated by a system of algebraic equations at discrete locations in space and time. The most important discretization methods are finite difference, finite volume and finite element.
- Coordinate System: It's important to choose the right coordinate system (Cartesian, cylindrical, spherical, etc.). The coordinate system depends on the target flow and will also influence the discretization method as well as the grid type.
- Numerical Grid: The numerical grid defines the discrete locations at which the variables are calculated on the geometric shape. The geometric shape is divided into a finite number of elements or control volumes. Possibilities: Structured grid, Block-structured grid, unstructured grid.
- Finite Approximations: The choice of finite approximations is dependent on the discretization method. For finite difference approximations for the derivatives at the grid points need to be selected. When using finite volume, surface and volume



integrals need to be approximated and with finite element method one has to choose shape and weighting functions.

- **Solution Methods:** After discretization a large system of non-linear algebraic equations is obtained. The right solutions strategy is dependent on the problem. Steady flows are normally solved with pseudo time marching or an equivalent integration scheme. Unsteady flows are solved with methods for initial value problems for ordinary differential equations marching in time. (Ferziger & Peric, 2002)

### 4.3 Navier-Stokes and Euler Equations

The Navier-Stokes equations are a system of nonlinear partial differential equations, which describe the conservation of mass, momentum and energy. For a Newtonian fluid in one dimension it is written as follows:

$$\frac{\partial Q}{\partial t} + \frac{\partial E}{\partial x} = 0 \quad (14)$$

$$Q = \begin{bmatrix} \rho \\ \rho \cdot u \\ e \end{bmatrix} \quad (15)$$

$$E = \begin{bmatrix} \rho \cdot u \\ \rho \cdot u^2 + p \\ u \cdot (e + p) \end{bmatrix} \cdot \begin{bmatrix} 0 \\ \frac{4}{3} \cdot \mu \cdot \frac{\partial u}{\partial x} \\ \frac{4}{3} \cdot \mu \cdot \frac{\partial u}{\partial x} + \kappa \cdot \frac{\partial T}{\partial x} \end{bmatrix} \quad (16)$$

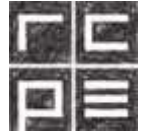
$\rho$  is the fluid density,  $u$  the flow velocity,  $e$  the total energy per unit volume,  $p$  is the pressure,  $\mu$  is the coefficient of dynamic viscosity,  $\kappa$  is the thermal conductivity and  $T$  is the temperature.

In many technical problems the flows are treated as steady (time-invariant). The steady state Navier-Stokes equations must satisfy:

$$\frac{\partial E}{\partial x} = 0 \quad (17)$$

If the Navier Stokes equation is in steady state and one also neglects viscosity and heat conduction, the Euler equations in 2D can be written as:

$$\frac{\partial Q}{\partial t} + \frac{\partial E}{\partial x} + \frac{\partial F}{\partial y} = 0 \quad (18)$$



$$Q = \begin{bmatrix} \rho \\ \rho \cdot u \\ \rho \cdot v \\ e \end{bmatrix} \quad (19)$$

$$E = \begin{bmatrix} \rho \cdot u \\ \rho \cdot u^2 + p \\ \rho \cdot u \cdot v \\ u \cdot (e + p) \end{bmatrix} \quad (20)$$

$$F = \begin{bmatrix} \rho \cdot u \\ \rho \cdot u \cdot v \\ \rho \cdot v^2 + p \\ u \cdot (e + p) \end{bmatrix} \quad (21)$$

(Lomax, Pulliam, & Zingg, 1999)

#### 4.4 Discretization

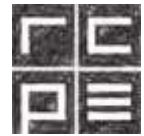
##### 4.4.1 Finite Difference Method

First of all, the solution domain (the geometry) needs to be covered by a structured grid. At each grid point, the conservation equations in differential form are solved by replacing the partial derivatives with approximations of the nodal values of the functions. The solution is one algebraic equation per grid node with the unknown variable value and some neighbour nodes in it.

To get the first and second derivatives of the variables depended on the chosen coordinate system Taylor series expansion and polynomial fitting are used. The advantage of the Finite Difference method is that it's very simple and effective on structured grids. Disadvantages are that it only gives good approximations on simple geometries and flows. If no further care is taken the conservation is not enforced.

##### 4.4.2 Finite Volume Method

In contrast to the Finite Difference Methods, the Finite Volume Method uses the integrated form of the conservation laws as starting point. The grid is made up of a finite number of continuous control volumes, where the integral form of the conservation laws is applied to each control volume. The variable values are calculated at the centre point of each control volume, so the grid nodes in the centre of each control volume. At the control volume surface interpolation is used to calculate the variable values. Like in



Finite Difference Methods, one ends up with one algebraic equation per control volume centre with the unknown variable and some neighbour nodal values in it. Due to the fact, that the control volume boundaries do not need to be related to a coordinate system. The method is conservative by construction as long as the surface integrals (represent convective and diffusive fluxes) are the same for the control volumes sharing boundary. This means that the control volume method can suit any type of grid and therefore can be used even for very complex geometries.

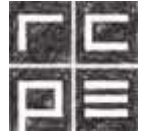
An advantage of the finite volume method is that all terms have a physical nature and are straightforward and understandable. The finite volume methods for higher order than second are difficult to develop in 3 dimensional space because the finite volume method needs three levels of approximation: Interpolation, Differentiation & Integration.

#### 4.4.3 Finite element method

In the finite element method the domain is divided into a set of unstructured elements (similar to the volumes, in finite volume method). The difference to the finite volume method is, that the equations are multiplied by so called weight functions before the integration. The easiest finite element methods use a solution approximated by a linear shape function for each element to enforce continuity over the element boundaries. The function is made with the information about the values in the corners of each element. Furthermore the approximation is substituted into a weighing integral of the conservation laws. These are solved by the derivation of the integral with respect to each nodal value to be zero. This gives the best solution within the set of non-linear algebraic equations. The biggest advantage of the finite element method is that it can deal with random geometries. The grids are easily refined, by simply subdividing each element. The downside, which is the same for all methods using unstructured grids, is that the linearized equations are not as well structured as for regular geometries, which makes it harder to find good solution methods. (Ferziger & Peric, 2002)

#### 4.4.4 Used differencing schemes

As there are many different schemes to approximate a solution for given equations, a short overview of the ones that were used for the discretization of the simulation of the airflow through the Innojet is given.



#### 4.4.4.1 Upwind scheme

The Upwind scheme is a finite difference scheme. We assume a 1D linear advection equation:

$$\frac{\partial u}{\partial t} + a \cdot \frac{\partial u}{\partial x} = 0; \text{ for } x \in [a, b], t > 0 \quad (22)$$

Furthermore we assume periodic boundary conditions, which means, that  $u$  and all derivatives of  $u$  are periodic for a period of  $b-a$ .

As seen in equation (22)  $u$  is also time dependent, that's why an initial condition is introduced:  $u(x, 0) = u_0(x)$ .

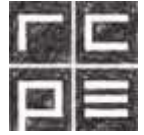
The interval  $[a, b]$  is separated in a uniform 1D mesh. The step size is defined as  $\frac{b-a}{N}$ , where  $N$  is the number of cells in the mesh. The grid point coordinates are defined as  $x_i = a + i\Delta x$ . To compute the approximated solution at discrete times  $t_n = n\Delta t, n \in \mathbb{N}$ , we introduce a time step  $\Delta t$ . Due to the periodic boundaries, the solution will be defined by its values at  $x_i$  for  $0 \leq i \leq N - 1$  and further applies:  $u(x_N, t_n) = u(x_0, t_n)$ , from this follows  $u_j^n = u(x_j, t_n)$ .

##### 4.4.4.1.1 First order explicit upwind scheme

Normally a finite difference is obtained by the approximation of the appearing derivatives in the partial differential equation by a Taylor series expansion up to a given order (which gives the order of the scheme). Only the values of the unknown function at the grid points are known. To eliminate all derivatives up to the beforehand fixed order, a Taylor expansion at different grid points is used and linearly combined. The same is done for the time discretization. For an approximation of order 1 in space and time, the equations are as follows:

$$\frac{\partial u}{\partial t}(x_j, t_n) = \frac{u(x_j, t_{n+1}) - u(x_j, t_n)}{\Delta t} + O(\Delta t) \quad (23)$$

$$\frac{\partial u}{\partial x}(x_j, t_n) = \frac{u(x_j, t_n) - u(x_{j-1}, t_n)}{\Delta x} + O(\Delta x) \quad (24)$$



For  $u_j^n$  the approximated solution using equation (23) & (24) for the approximation of the partial derivatives of equation (22) at the points  $x_j$  and  $t_n$  we get:

$$\frac{u_j^{n+1} - u_j^n}{\Delta t} + \frac{u_j^n - u_{j-1}^n}{\Delta x} = 0 \quad (25)$$

To compute  $u_j^{n+1}$ , equation (25) has to be rearranged:

$$u_j^{n+1} = u_j^n - a \cdot \frac{\Delta t}{\Delta x} \cdot (u_j^n - u_{j-1}^n) \quad (26)$$

#### 4.4.4.1.2 First order upwind implicit scheme

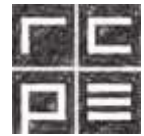
Another possibility is using an uncentred difference scheme in the other direction of the time derivative

$$\frac{\partial u}{\partial t}(x_j, t_n) = \frac{u(x_j, t_n) - u(x_j, t_{n-1})}{\Delta t} + O(\Delta t) \quad (27)$$

The approximation for the space derivative stays as in equation (24), which combined leads to following implicit scheme:

$$u_j^{n-1} = u_j^n + a \cdot \frac{\Delta t}{\Delta x} \cdot (u_j^n - u_{j-1}^n) \quad (28)$$

(Sonnendrücker, 2013)



## 5 Discrete element method

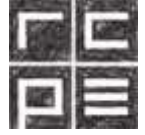
### 5.1 Introduction

The macroscopic movement of particles is driven by interactions between individual particles, particles with the wall and also particles with the surrounding fluid. To understand the microscopic behaviour of these mechanisms several discrete modelling techniques were developed, for example Monte Carlo methods, cellular automata and discrete element methods (DEM). DEM gives information about single particles, like the trajectories of their movement and the transient forces acting on them. This is impossible to obtain with physical experiments. DEM allows detailed information of every single particle and how it interacts over time with other particles, the wall and the surrounding fluid. As particles collide with each other contacts are established and/or released, these collisions lead to plastic/elastic deformations and frictional forces between particles, which are described by Newton's second law (law of motion). Discrete element methods are used if a large number of particles and their change of contact locations and conditions are of interest. The first assumption, which needs to be done, is if the simulations deal with rigid or deformable particles. For rigid particles with simple shape the collision times can be calculated exactly (contact time is infinitely short) and the post collision velocities (the energy loss due to particle interactions with particles, wall, fluid, etc.) are calculated via a coefficient of restitution, with one collision per time step. Hard particle models are mostly used in rapid granular flows (Zhu, Zhou, Yang, & Yu, 2007). For simulations with deformable particles the contact time is not infinitely short anymore and the contact forces vary due to the different contact times (Bicanic, 2007). A difference between hard and soft sphere models is, that in soft sphere simulations multiple particle contacts at a time step can be calculated, which is important for the simulation of quasi-static or dense packed systems. (Zhu, Zhou, Yang, & Yu, 2007)

### 5.2 Equations and force models

There are 2 types of motion a particle can have in granular flow:

- Translational
- Rotational



During the movement a particle will respectively be influenced by the movement of other particles, the movement of surrounding fluid and/or the wall. Through this influence momentum and energy is exchanged between the interacting phases. One main problem in DEM is, that particles are not only influenced by the torques and forces of neighbouring particles and fluid nearby but also from the propagation of disturbance waves of particles and fluid away from them. To get hold of this problem a numerical time step needs to be chosen, which restricts the propagation of the disturbance to only neighbouring particles and fluid. For coarse particulate systems the forces on the particles can be calculated with only the interactions of nearby particles and fluid. If the system is made up of fine particles also non-contact forces like Van-der-Waals and electrostatic forces need to be taken into account. To mathematically describe the rotational and the translational movement Newton's second law is used. For a particle  $i$  with the mass  $m_i$  and the moment of inertia  $I_i$  the equations are shown below:

$$m_i \frac{dv_i}{dt} = \sum_j F_{ij}^c + F_i^f + F_i^g + \sum_j F_{ik}^{vW} + \sum_j F_{ik}^E \quad (29)$$

$$I_i \frac{d\omega_i}{dt} = \sum_j M_{ij} \quad (30)$$

$v_i$  is the particles translational velocity,  $F_{ij}^c$  is the contact force acting on particle  $i$  by particle  $j$  or a wall,  $F_i^f$  is the force of surrounding fluid on the particle and  $F_i^g$  is the gravitational force,  $F_{ik}^{vW}$  is the Van-der-Waals,  $F_{ik}^E$  is the electrostatic force and both are acting on particle  $i$  by particle  $k$  or other sources.

$\omega_i$  is the angular velocity and  $M_{ij}$  is the torque acting on particle  $i$  by particle  $j$  or the wall. In Figure 6 the equations (29) & (30) on particle  $i$  are graphically shown.

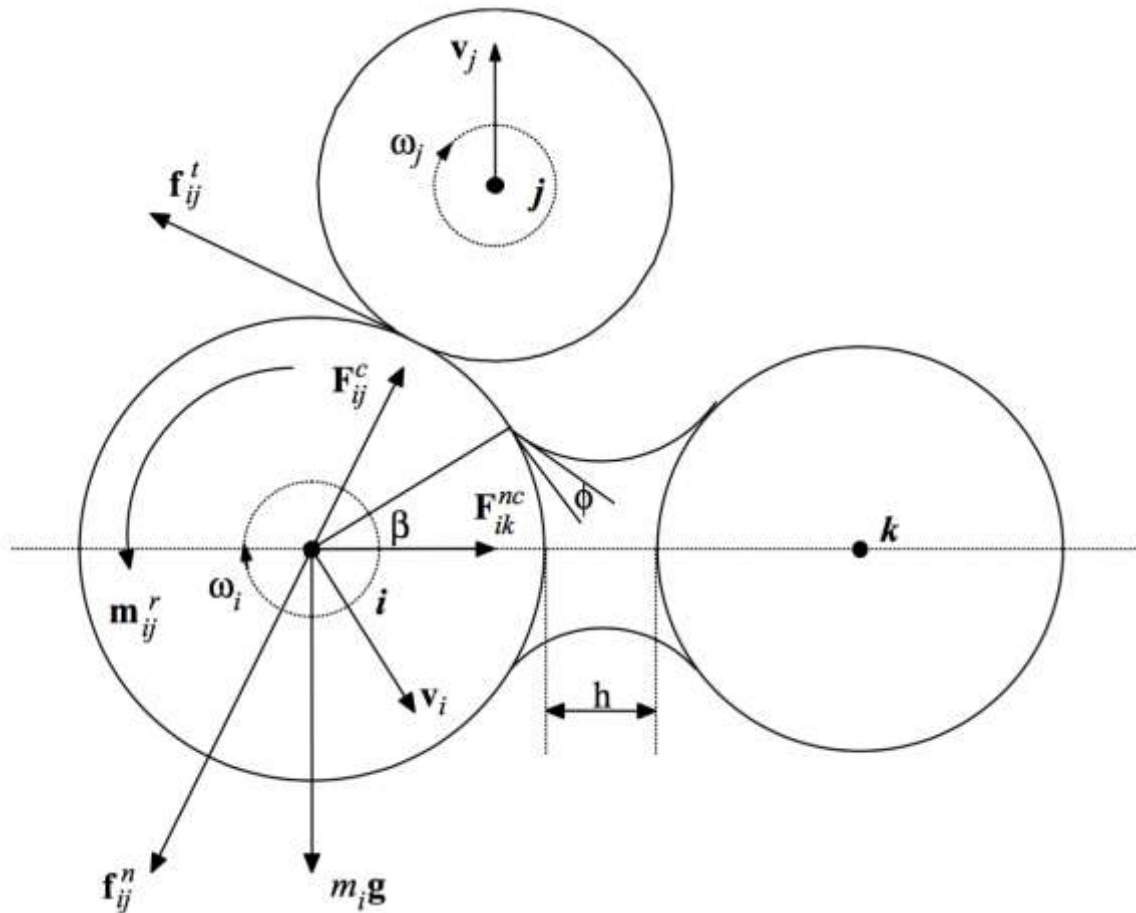
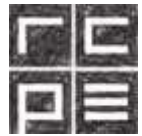


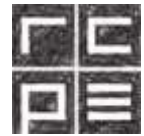
Figure 6: Graphic of newton second law. Mass- and inertial forces acting on a particle in contact with another particle (Zhu, Zhou, Yang, & Yu, 2007)

### 5.2.1 Contact forces

The contact between 2 particles is never just a single contact point but rather a contact area due to deformation. In DEM these deformations are thought of as two stiff bodies overlapping slightly. The resulting body force is split into two components: Tangential and normal force. To describe the contact tractions distribution of the resulting area many geometrical and physical properties like shape, material and the movement pattern of the particles have to be known. To efficiently describe these forces and the physical and material behaviour simple models and equations were introduced to determine the forces and torques resulting from the particle-particle contact.

- Linear models:

Linear spring-dashpot model (Figure 7): Proposed by (Cundall & Stack, 1979); the collision is modelled between a particle and a flat base with a contact force  $F_c$  and a damping  $F_d$ . The contact force  $F_c$  between particle and base is direct proportional to the overlap,  $\delta$ :



$$F_c = k_L \cdot \delta \quad (31)$$

$k_L$  is the linear-spring constant. Some of the kinetic energy is converted into heat and sound and also in plastic deformation. For the dissipation of the energy, a damping for  $F_d$  is introduced:

$$F_d = \eta \cdot v \quad (32)$$

$v$  is the relative velocity of the particle and  $\eta$  is the damping coefficient. (Malone & Xu, 2008)

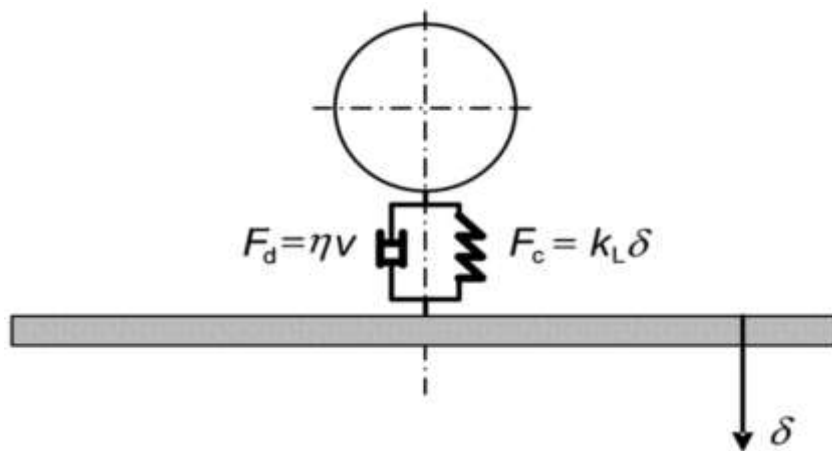


Figure 7: Linear spring-dashpot model of a particle colliding with a wall (Malone & Xu, 2008)

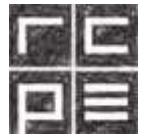
Linear spring model: Is the same model, but without the damping factor and further the dissipation and conversion of energy in heat, sound or plastic deformation. (Di Renzo & Di Maio, 2003)

- Non-linear models:

Hertz-Mindlin and Deresiewicz: (Hertz, 1882) developed a theory about the normal elastic contact between two spheres and (Mindlin & Deresiewicz, 1953) further proposed a model for the tangential forces. They showed, that the force-displacement is a function of the loading history and the change of the normal and tangential force or displacement. The calculations of the non-linear model is very time consuming and therefore not very popular in DEM simulations with a high number of particles.

### 5.2.2 Non-contact forces

There is a large impact of non-contact forces if the particles are very fine and/or humidity is high. In DEM the non-contact forces can be considered directly. The non-



contact forces include van der Waals force, capillary force and electrostatic force with varying importance dependent on the particle diameter (Figure 8):

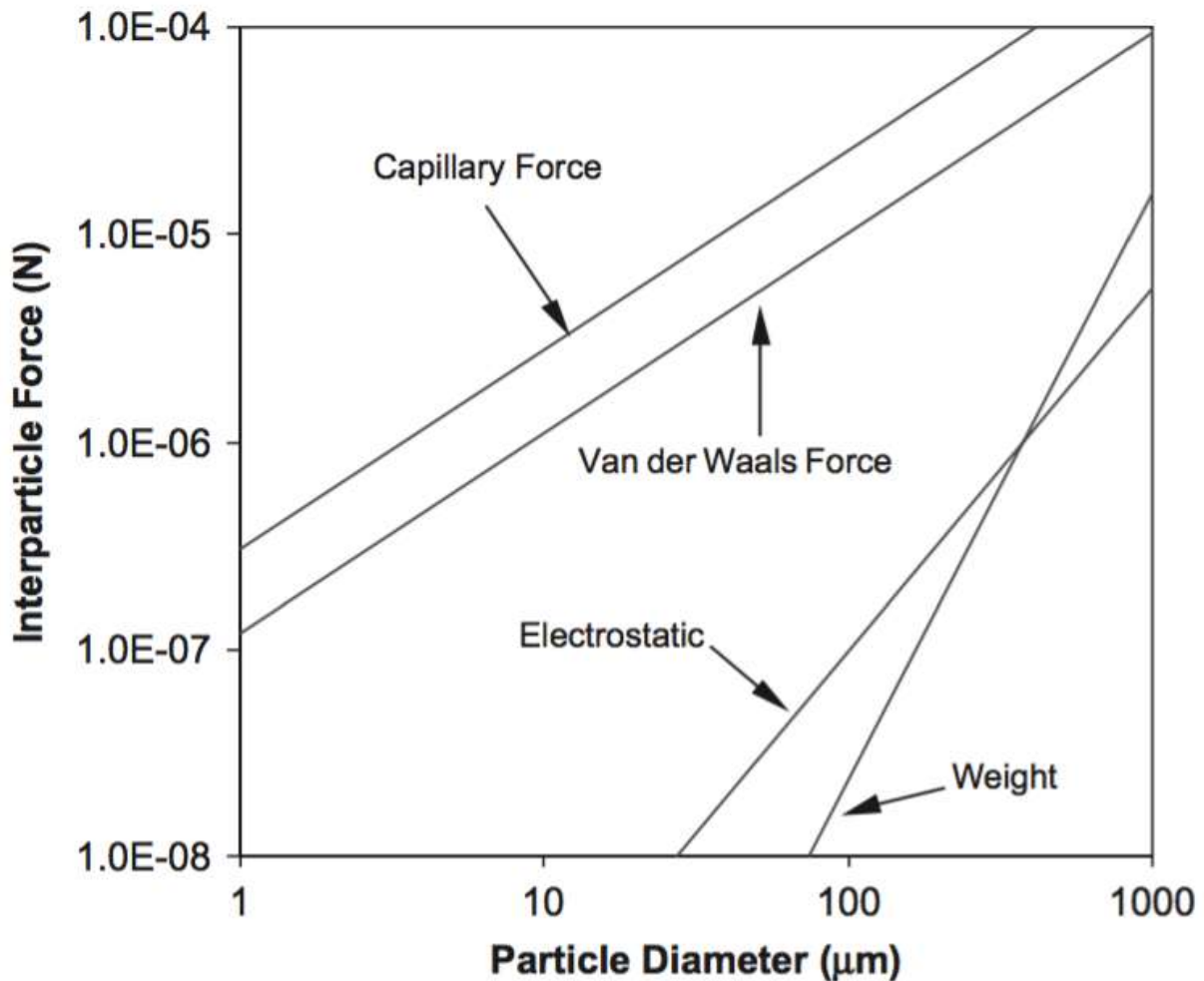


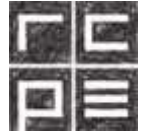
Figure 8: Comparison of the magnitude of inter-particle forces (Zhu, Zhou, Yang, & Yu, 2007)

**Van der Waals forces:** Are a collection of dipole-dipole, dipole-non polar and non polar-non polar forces between particles. For sphere-sphere interaction the Van der Waals force can be calculated with:

$$F_{vw} = \frac{A \cdot R}{12 a^2} \quad (33)$$

R is the radius of the sphere, A is the (material specific) Hamaker constant and a is the distance between the 2 surfaces. (Seville, Willett, & Knight, 2000)

**Electrostatic force:** Also called Coulomb force is an attractive or repulsive force between particles or objects due to electric charge. Two positive and two negative charges repel each other and 2 different charges (positive-negative) will attract each other. It can be calculated using:



$$\mathbf{F}_c = \frac{k \cdot q_1 \cdot q_2}{r^2} \quad (34)$$

$q_1$  is the electric charge of particle 1 and  $q_2$  the electric charge of particle 2,  $k$  is a proportionality factor and  $r$  is the distance between the two centres of the particles. (Britannica, 2016)

**Capillary force:** Two spherical surfaces in contact create a narrow slit around the contact area. For lyophilic surfaces (dispersed phase with a high affinity for the continuous phase), some of the surrounding vapour will condense and form a meniscus. Due to the meniscus an attractive force is created. The surface tension of the liquid pulls the particles together and further the pressure inside the meniscus is reduced (compared to the pressure in the system) due to the capillary pressure  $\Delta P$  and pulls the particles further together.

$$\Delta P = \gamma \left( \frac{1}{r_1} + \frac{1}{r_2} \right) \quad (35)$$

with  $\gamma$  as the surface tension and  $r_1$  and  $r_2$  as the two radii of the particles. This is the so-called Young-Laplace equation. Two radii characterize the equation for the capillary force, the meridional radius  $r$  and the azimuthal radius  $l$  (concave to the liquid).

$$F_{\text{Cap}} = 2\pi\gamma l - \pi l^2 \Delta P \quad (36)$$

$$\text{with } \Delta P = \gamma \left( \frac{1}{l} - \frac{1}{r} \right) \quad (37)$$

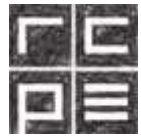
(Butt & Kappl, 2008)

### 5.2.3 Particle-Fluid Interactions

Additionally to particle-particle contact forces and non-contact forces, the surrounding fluid also plays a big part in particle motion. Buoyancy force, particle-fluid drag force, pressure force and other unsteady forces such as virtual mass force and Basset force are implemented in DEM simulations for a valid description of the system of particles. For a single particle moving through a gas the drag resistance can be calculated with the Newton equation:

$$F_d = \frac{C_d \cdot \pi \cdot \rho_f \cdot d_p^2 \cdot |u - v| \cdot (u - v)}{8} \quad (38)$$

The drag coefficient  $C_d$  is a function of the particle Reynold's number (49) and liquid properties. There are 3 regions of Reynold's numbers, which have well-established correlation functions (Zalilah, 2016). These regions are Stoke's law, transition law and



Newton's law. The change of the drag coefficient with different Reynold's numbers is shown in Figure 9.

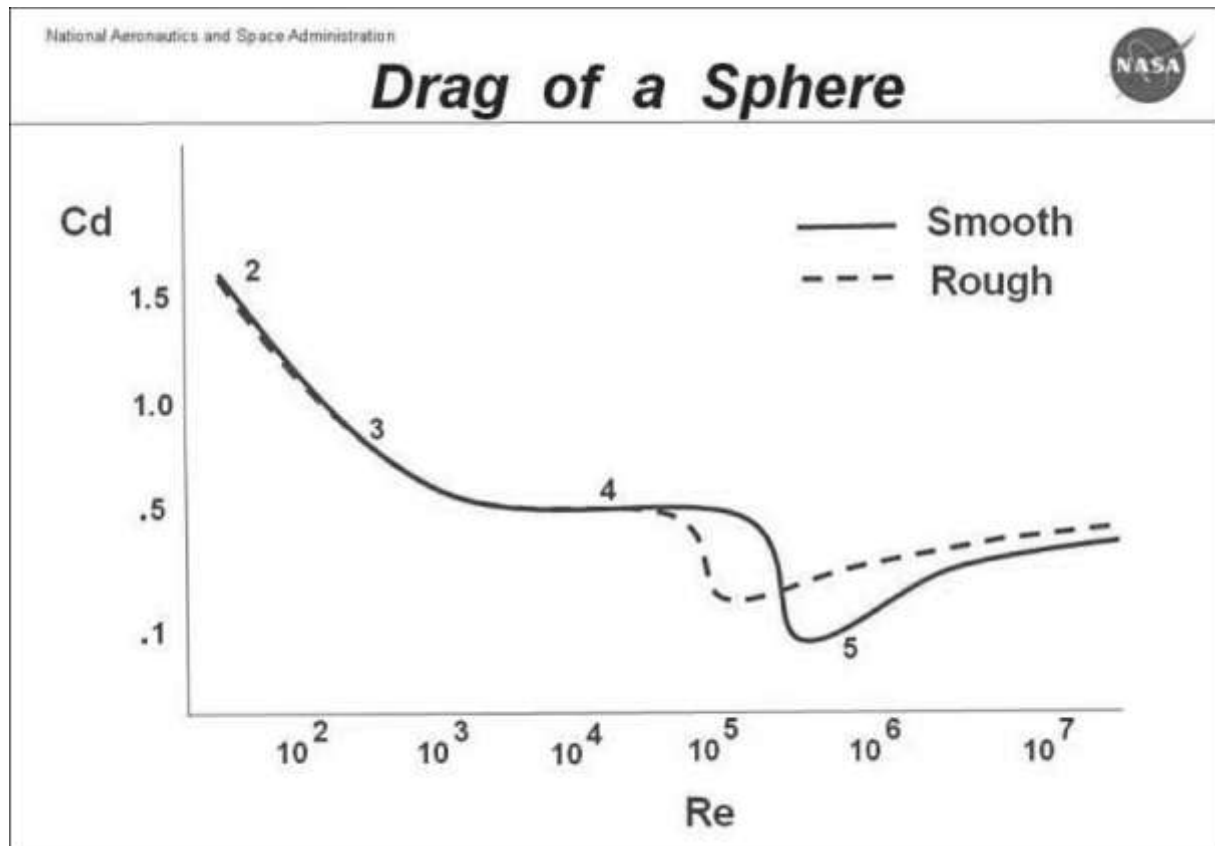
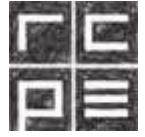


Figure 9: Change of the drag coefficient of a smooth respectively a rough sphere with different Reynolds numbers (NASA, 2016)

For a system of particles it becomes more complex. Every single particle is influenced by the other particles in the system. The space for the fluid is reduced, which generates a high velocity gradient and further a higher shear stress on the particle surface. To estimate the particle-fluid drag two methods have been established:

- Based on empirical correlations like bed pressure drop (Ergun, 1952) (Wen & Yu, 1966) or bed expansion experiments (Richardson, 1971). The system of particles is evaluated with a local porosity and this is connected to either the flow regime or the particle Reynolds number.
- Based on numerical simulations at a micro scale with direct numerical simulation (Choi & Joseph, 2001) and Lattice-Boltzmann computation (Zhang, 1999b), but these are computational expensive and to date only used for rather simple systems. (Zhu, Zhou, Yang, & Yu, 2007)



## 6 CFD-DEM Modelling

The CFD-DEM coupling corresponds to an Euler-Lagrangian approach. The incompressible Newtonian fluid phase is treated as a continuum and is based on the Euler approach. The particle phase (disperse phase) is described with Newton's second law as a system of single particles, which is a Lagrangian approach.

- Lagrange: The movement of a single particle is traced through the Volume. The position of the particle is a function of initial position  $\vec{r}_0 = (a, b, c)$  and time  $t$ . The streamline is written as  $\vec{r} = \vec{r}(\vec{r}_0, t)$ .
- Euler: The change of the stream characteristics is calculated at a fixed point in the volume, with the particles running through it. (Zierep & Bühler, 2010)

### 6.1 Continuous phase modelling

The modelling of the gas phase is done with the Volume-Averaged Navier-Stokes equations, where all the variables are volume-averaged quantities over a (at least) one order of magnitude larger control volume  $V$ . The equation for the conservation of mass is shown below:

$$\frac{\partial}{\partial t}(\varepsilon_f \rho_f) + \nabla(\varepsilon_f \rho_f \vec{v}_f) = 0 \quad (39)$$

$\rho_f$  is the fluid density,  $\varepsilon_f$  is the local volume fraction,  $\vec{u}_f$  is the velocity vector of the fluid.

Furthermore the conservation of the momentum is written as:

$$\frac{\partial}{\partial t}(\varepsilon_f \rho_f \vec{v}_f) + \nabla(\varepsilon_f \rho_f \vec{v}_f \vec{v}_f) = -\varepsilon_f \nabla p - \nabla(\varepsilon_f \tau_f) + \varepsilon_f \rho_f \vec{g} - S_p \quad (40)$$

$p$  is the hydrodynamic pressure,  $\vec{g}$  is the gravity acceleration vector,  $S_p$  is the interphase momentum transfer source term between particles and fluid and  $\tau_f$  is the stress tensor, which is defined as

$$\tau = -p\mathbf{I} + \sigma \quad (41)$$

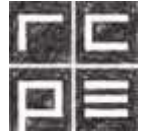
$\mathbf{I}$  is the unit matrix and  $\sigma$  is the viscous stress tensor

$$\sigma = \mu_f (\nabla \vec{v}_f + \nabla \vec{v}_f^T) - \frac{2}{3} \mu_f \nabla \cdot \vec{v}_f \mathbf{I} \quad (42)$$

$\mu_f$  is the dynamic viscosity (Jajcevic, Siegmann, Radeke, & Khinast, 2013)

### 6.2 Disperse phase and drag force modelling

The motion of each single particle is derived from Newton's second law of motion. This was shown in equation (29) and will now be expanded to:



$$m_p \frac{d\vec{v}_p}{dt} = -V_i \nabla p + \beta (\vec{v}_f - \vec{v}_p) + \sum_{N_p} F_{p \rightarrow p} + \sum_{N_w} F_{p \rightarrow w} + m_p \vec{g} \quad (43)$$

$m_p$  is the mass of the individual particle,  $-V_i \nabla p$  is the pressure gradient,  $\beta$  is the interphase momentum transfer coefficient and the summed up terms where described in equation (29). The angular momentum was described in equation (30).

To model the fluid drag force the Ergun-Wen-Yu model derived by (Gidaspow, 1994) is used, where the interface momentum transfer coefficient  $\beta$  is written as a function of the solid fraction  $\varepsilon_s$ , the fluid fraction  $\varepsilon_f$ , the particle Reynolds number  $Re_p$ , the particle diameter  $d_p$  and the particle density  $\rho_p$ .

For dense systems  $\varepsilon_f < 0,8$  the (Ergun, 1952) equation is used:

$$\beta_{Ergun} = 150 \cdot \frac{\varepsilon_s^2 \mu_f}{\varepsilon_f d_p^2} + 1,75 \cdot \frac{\varepsilon_s \rho_f}{d_p} \cdot |\vec{u}_f - \vec{u}_p| \quad (44)$$

and for dilute systems  $\varepsilon_f \geq 0,8$  the interface momentum transfer is estimated with the (Wen & Yu, 1966) equation:

$$\beta_{Wen-Yu} = \frac{3}{4} C_D \cdot \frac{\varepsilon_s \rho_f}{d_p} \cdot |\vec{u}_f - \vec{u}_p| \cdot \varepsilon_f^{-2,65} \quad (45)$$

For the calculation of the drag coefficient  $C_D$ , at first the particle Reynolds number is calculated:

$$Re_p = \rho_f \cdot d_p \frac{|\vec{u}_f - \vec{u}_p| \cdot d_p}{\mu_f} \quad (46)$$

With the result of the particle Reynolds number, the drag coefficient  $C_D$  is expressed as:

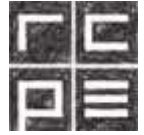
$$C_D = \begin{cases} \frac{24}{\varepsilon_f Re_p} \cdot (1 + 0,15 \cdot (\varepsilon_f Re_p)^{0,687}) & \text{for } Re_p < 1000 \\ 0,44 & \text{for } Re_p \geq 1000 \end{cases} \quad (47)$$

For the transition of the two regimes, (Huilina & Gidaspow, 2003) introduced another function:

$$\varphi_{gs} = \frac{\arctan(150 \cdot 1,75 \cdot (0,2 - \varepsilon_s))}{\pi} + 0,5 \quad (48)$$

which is used to weight the inter-phase transfer coefficient:

$$\beta = (1 - \varphi_{gs}) \cdot \beta_{Ergun} + \varphi_{gs} \cdot \beta_{Wen-Yu} \quad (49)$$



### 6.3 Particle-Particle & Particle-Wall interaction models

As mentioned in chapter 5.2.1 there are different ways to model the particle-particle contacts. This work was done with a soft sphere model with either linear spring-dashpot model to calculate the contact forces or a MEPA model to calculate contact and cohesion.

#### 6.3.1 Linear Spring-Dashpot

In Figure 10 the particle-particle contact in the soft sphere model is shown. There is a small overlap  $\delta_n$  between particle  $P_A$  and  $P_B$  in contact. As a result of the particle overlap, the relative velocity, the spring stiffness and the damping parameter a repulsive force emerges.

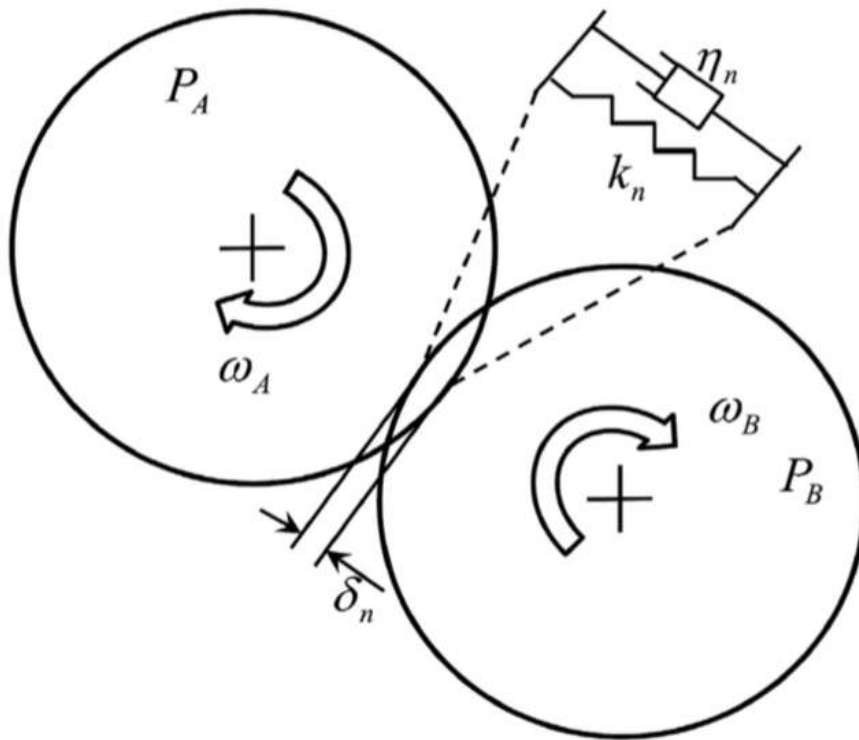
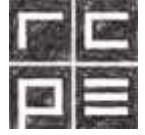


Figure 10: Particle-Particle interactions with a soft sphere model (Jajcevic, Siegmann, Radeke, & Khinast, 2013)

The calculation of the normal force is shown in the equation below:

$$\vec{F}_{p_A \rightarrow p_B, n} = -k_n \delta_n \vec{n}_{AB} - \eta_n \vec{u}_{AB, n} \quad (50)$$

$k_n$  is the spring stiffness,  $\delta_n$  is the upper mentioned overlap between the two spheres,  $\vec{n}_{AB}$  is the unit vector between the centres of the particles  $P_A$  and  $P_B$ ,  $\eta_n$  is the damping parameter and  $\vec{u}_{AB, n}$  is the normal relative velocity for the particles  $P_A$  and  $P_B$ . The damping parameter  $\eta_n$  can be calculated using the formula of (Pepiot & Desjardins, 2012).



$$\eta_n = -2 \cdot \ln(e_{n,p \rightarrow p}) \cdot \frac{\sqrt{\left(\frac{1}{m_A} + \frac{1}{m_B}\right)^{-1} \cdot k_n}}{\sqrt{\pi^2 + (\ln(e_{n,p \rightarrow p}))^2}} \quad (51)$$

with  $e_{n,p \rightarrow p}$  the normal coefficient of restitution (it has to apply:  $0 < e_{n,p \rightarrow p} < 1$ ) and  $m_A$  and  $m_B$  are the masses of the particles A and B in contact.

For  $\vec{u}_{AB}$  the following equation is used:

$$\vec{u}_{AB} = \vec{u}_A - \vec{u}_B - (R_A \omega_A + R_B \omega_B) \times \vec{n}_{AB} \quad (52)$$

And from equation (52), the normal relative velocity is derived:

$$\vec{u}_{AB,n} = (\vec{u}_{AB} \cdot \vec{n}_{AB}) \cdot \vec{n}_{AB} \quad (53)$$

The next unknown in equation (50) and further in equation (53), which is the unit vector  $\vec{n}_{AB}$  between the two particle centres in contact is calculated with the positional vectors of the particles A and B.

$$\vec{n}_{AB} = \frac{\vec{p}_B - \vec{p}_A}{|\vec{p}_B - \vec{p}_A|} \quad (54)$$

After the derivation of the normal component, the derivation of the tangential component of the contact force with a Coulomb-type friction law (Deen, Annaland, Hoef, & Kuipers, 2005) is done.

$$\vec{F}_{p_A \rightarrow p_B,t} = \begin{cases} -k_t \delta_t - \eta_t \vec{u}_{AB,t} & \text{for } |\vec{F}_{p_A \rightarrow p_B,t}| \leq |\vec{F}_{p_A \rightarrow p_B,n}| \\ -\mu_{fr,p \rightarrow p} \cdot |\vec{F}_{p_A \rightarrow p_B,n}| \cdot \vec{t}_{AB} & \text{for } |\vec{F}_{p_A \rightarrow p_B,t}| > |\vec{F}_{p_A \rightarrow p_B,n}| \end{cases} \quad (55)$$

$k_t$  is the tangential spring stiffness,  $\delta_t$  is the tangential displacement,  $\eta_t$  is the tangential damping parameter and  $\vec{u}_{AB,t}$  is the tangential velocity for the particles  $P_A$  and  $P_B$ ,  $\mu_{fr,p \rightarrow p}$  is the friction coefficient and  $\vec{t}_{AB}$  is the tangential unit vector. The used equations are derived below:

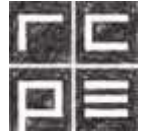
- Tangential displacement:

$$\delta_t = \vec{u}_{AB,t} \cdot \Delta t \quad (56)$$

- Tangential velocity:

$$\vec{u}_{AB,t} = \vec{u}_{AB} - \vec{u}_{AB,n} \quad (57)$$

- Tangential damping coefficient (Deen, Annaland, Hoef, & Kuipers, 2005):



$$\eta_n = -2 \cdot \ln(e_{t,p \rightarrow p}) \cdot \frac{\sqrt{\left(\frac{2}{7}\right) \left(\frac{1}{m_A} + \frac{1}{m_B}\right)^{-1} \cdot k_t}}{\sqrt{\pi^2 + (\ln(e_{t,p \rightarrow p}))^2}} \quad (58)$$

with  $0 < e_{t,p \rightarrow p} < 1$  as the tangential coefficient of restitution.

- Tangential unit vector:

$$\vec{t}_{AB} = \frac{\vec{u}_{AB,t}}{|\vec{u}_{AB,t}|} \quad (59)$$

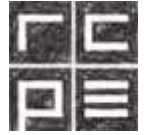
These equations above all show particle-particle contact. To model the particle-wall contacts the walls are just considered as particles with infinite mass, zero radius (only the mass of particle A is considered in the damping) and zero angular velocity. The only thing that changes is in equation (55), the particle-particle friction coefficient  $\mu_{fr,p \rightarrow p}$  is exchanged with the particle-wall coefficient  $\mu_{fr,p \rightarrow w}$ . (Jajcevic, Siegmann, Radeke, & Khinast, 2013)

### 6.3.2 MEPA (Macroscopic Elasto-Plastic Adhesive) contact model

The MEPA model uses a maximum force-based failure; this means the maximum displacement of the contact is determined by the material's tensile strength, elastic modulus and Poisson's ratio. The unique aspect of the MEPA model is, that the particle behaviour is described with macro and micro mechanics like material yield limits and physical properties. The simulation model is rather about mechanical behaviour of physical materials data in a shear test than the molecular mechanical laws. The MEPA model takes plastic contact deformation and cohesive attraction into account. As mentioned before, at particle-particle contacts the particles undergo elastic and plastic deformations and with increased plastic contact area, the pull-off force increases. The MEPA model uses 4 parameters to represent the loading, unloading/re-loading and cohesive branches:

- Virgin loading parameter  $k_1$
- Unloading & Reloading parameter  $k_2$
- Cohesive parameter  $k_{adh}$
- Index parameter  $n$  (Controlling the order of the system)

$$f_1(\delta) = k_1 \delta^n \quad (60)$$



$$f_2(\delta) = k_2(\delta^n - \delta_p^n) \tag{61}$$

$$f_3(\delta) = -k_{adh}\delta^n \tag{62}$$

$\delta_p^n$  is the maximum plastic contact indentation, which arises from elastic unloading to a zero contact force from a non-zero overlap  $\delta$ .

The whole relationship is expressed as:

$$f_{hys} = \begin{cases} f_1(\delta) & \text{for } f_2(\delta) \geq f_1(\delta) \\ f_2(\delta) & \text{for } f_1(\delta) > f_2(\delta) > f_3(\delta) \\ f_3(\delta) & \text{for } f_3(\delta) \geq f_2(\delta) \end{cases} \tag{63}$$

The normal force is characterized by

$$f_0^n = \gamma_n \vec{v}_n + f_{hys} \vec{n} \tag{64}$$

$\gamma_n$  the viscous dissipation of the system,  $\vec{v}_n$  is the normal relative velocity of the particle and  $\vec{n}$  is the normal direction unit vector.

For the tangential force, the normal force it connected to it via Coulombs law:

$$f^t \leq \mu_s f_{hys} \tag{65}$$

(Del Cid, 2015)

For better oversight, the non-linear MEPA cohesive contact law hysteresis is show in Figure 11.

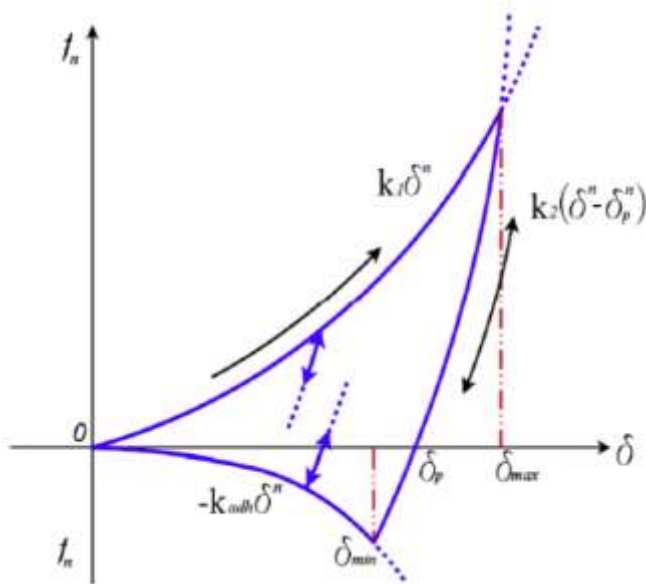
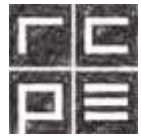


Figure 11: Non linear contact law hysteresis (Del Cid, 2015)



### 6.3.3 CFD-DEM coupling data management

The continuous phase (fluid) and the dispersed phase (particles) are coupled with the source term  $\vec{S}_p$  and the fluid volume fraction  $\varepsilon_f$ . One of the goals in CFD-DEM coupling is to minimize the amount of data that is exchanged between the CFD and the DEM code, to keep the time consumption at a minimum. In Figure 12 the coupling scheme between commercial AVL-Fire and in house made eXtended particle systems XPS.

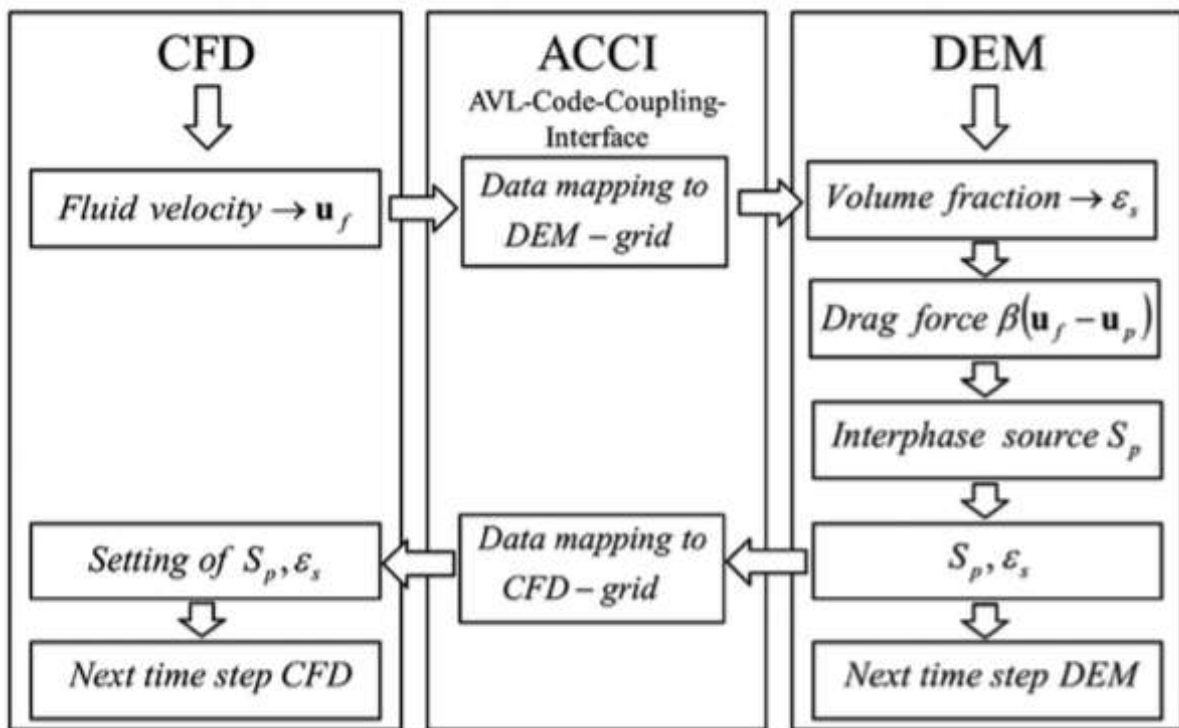
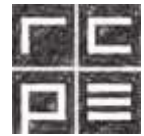


Figure 12: CFD-DEM coupling scheme via AVL-Code-Coupling-Interface (Jajcevic, Siegmann, Radeke, & Khinast, 2013)

The fluid phase model is solved in the CFD code of AVL Fire in a multiphase setup, which considers the fluid and the solid phase separately. The motion and collision of the solid particles is calculated in the DEM code of XPS. At the beginning of the calculation, the fluid velocity field is transferred from the CFD code via the ACCI to the DEM code. Using the volume fraction and the transferred fluid velocity field, the DEM code calculates the drag force, which acts on the particles, and further the interphase source term. The newly calculated field is then transferred back to the CFD code. (Jajcevic, Siegmann, Radeke, & Khinast, 2013)



## 7 Materials and Methods

### 7.1 Innojet Ventilus 2.5 equipped with a hot melt device (Romaco Innojet, Germany)

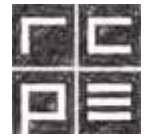
Explanation for the numbers in Figure 13: The Innojet Ventilus and the IHD hot melt device:

#### 7.1.1 IHD Hot melt device:

1. Temperature sensor for coating material
2. Vessel for melting and stirring the molten material
3. Magnetic stirrer with hot plate for the melting process
4. Scale for spray rate calibration and monitoring
5. Tube for connection of Hot melt vessel and peristaltic pump (hot air flow through it to heat the pipe)
6. Pump control for the revolutions per minute and temperature of the pump head (display at point 8.)
7. Switch for air heating system (to keep the excipient in molten state through the pumping system to the nozzle)
8. Displays and controls for the air heating system (top) the pump head temperature (middle) and hot melt temperature (bottom) measured at point 14.
9. Manometer to regulate spray pressure
10. Switch for air supply (for the melt stabilizing system described in 7.)
11. Switch for the IHD hot melt device (also emergency switch)
12. Control wheel for the atomization air pressure (manometer in point 9)
13. Heated connection from the IHD to the Innojet Ventilus and further the spray nozzle (also heated by the air flow described in point 7)

#### 7.1.2 Ventilus V-2.5/1 fluid bed device:

14. Container for accumulation of hot air for keeping the nozzle on temperature and also keeping the plastic pipes on temperature while the molten excipient is flowing through to the nozzle
15. Spray nozzle holder and distributor plate. Inlet of the air and (bottom spray) molten excipient
16. Filling for raw particular material and sample point



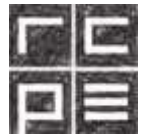
## CFD-DEM Simulation of a Hot Melt Fluidized Bed Coating Process

17. Infrared sensor for measurement of product temperature
18. Fluid chamber (1l glass device)
19. Measurement of differential pressure in the filter system
20. Filter dome
21. Filter cleaning system and outlet temperature measurement
22. Control and regulation display of inlet air temperature, outlet air temperature, product temperature, air-flow rate, pressure monitoring, status of out let F6/F9 and inlet F6.

(Becker K. , 2016)



Figure 13 Innojet Ventilus V-2.5/1 with IHD Hot Melt Device (Becker K. , 2016)



### 7.1.3 Piping & Instrumentation Diagram (P&ID) Innojet Ventilus V-2.5/1

Fresh air enters the fluid bed equipment through filter F9. It is accelerated in the compressor and lead through a heater. After the heater the hot air enters the fluid bed reactor through the distributor plate. After the reactor, the dust-loaded air goes through the first air filters inside the fluid bed chamber and afterwards through filters F6 and F9. Part of the air is recycled and used to clean the ‘in-reactor’ outlet filters. After passing the output compressor and the damper, the air is put back in the operating room. In Figure 14 an excerpt of the P&ID of the Innojet Ventilus 2.5 is shown.

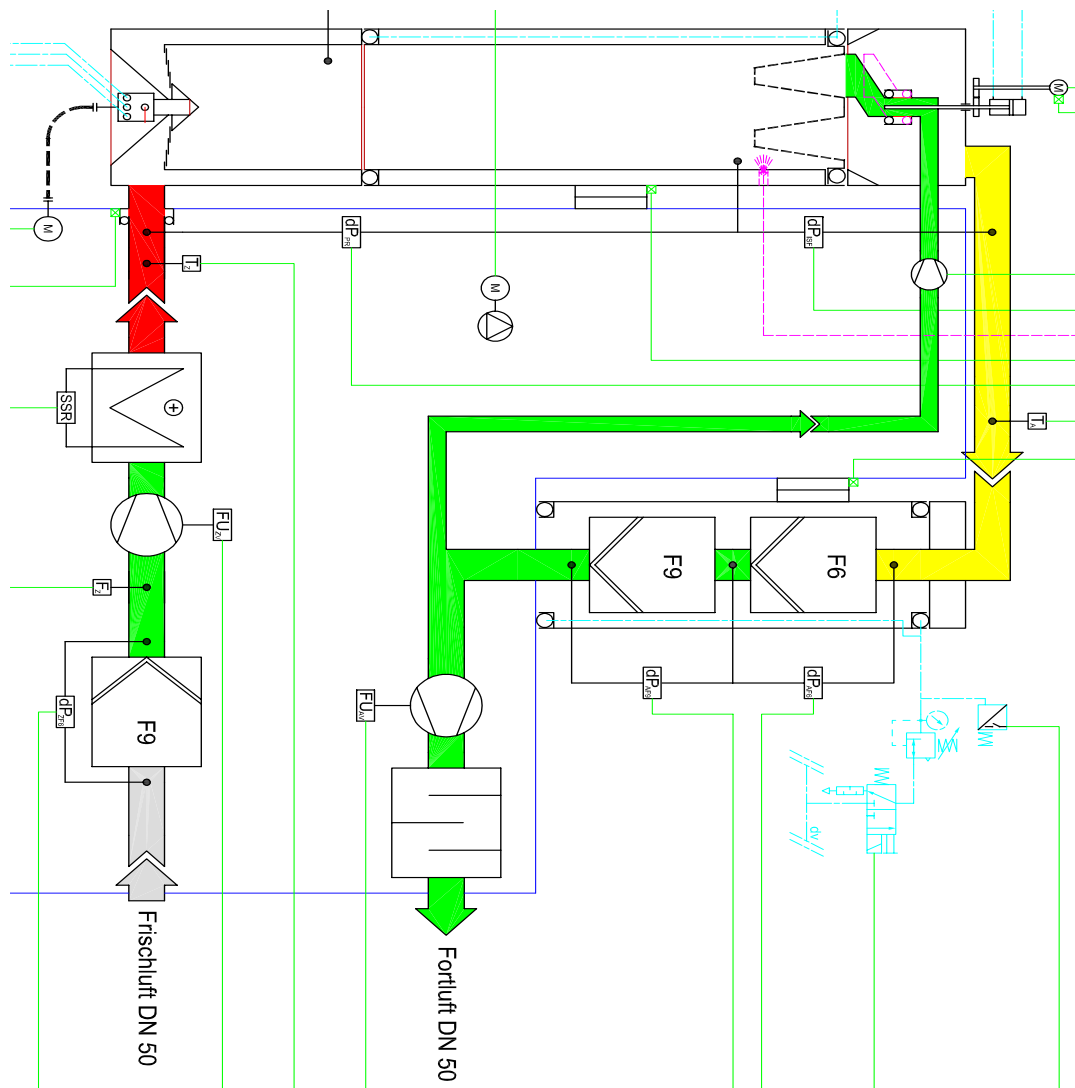
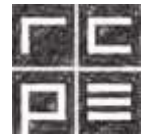


Figure 14: Excerpt from the P&ID of the Innojet Ventilus 2.5 (Romanco Innojet, 2012)



## 7.2 Active Pharmaceutical Ingredient (API)

### 7.2.1 N-acetylcystein (NAC)

Chemical Formula:  $C_5H_9NO_3S$

Molecular weight: 163.195 g/mol (NIST, nist.gov)

Melting point: 109.5°C (Lide, 2005)

Solubility in water (buffer at pH 7.4):  $>24.5 \mu\text{g/ml}$  (PubChem)

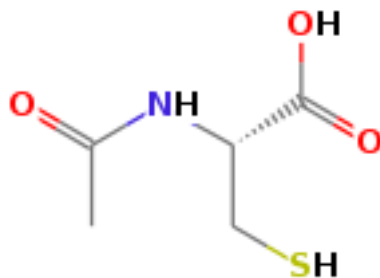


Figure 15: Chemical structure of N-acetylcystein (NIST, nist.gov)

## 7.3 Excipients

### 7.3.1 Tristearin (Dynasan 118)

Chemical Formula:  $C_{57}H_{110}O_6$

Molecular weight: 891.4797 g/mol (NIST, nist.gov)

Melting point(s):

Table 3: Melting points of the different polymorphs of Tristearin (Chapman, 1961)

$\alpha$ -Configuration	54°C
$\beta'$ -Configuration	64°C
$\beta$ -Configuration	73.1°C

Solubility in water (buffer at pH 7.4): Not soluble in water, little solubility in cold ethanol (Heydt & Schiedermaier, 2019)

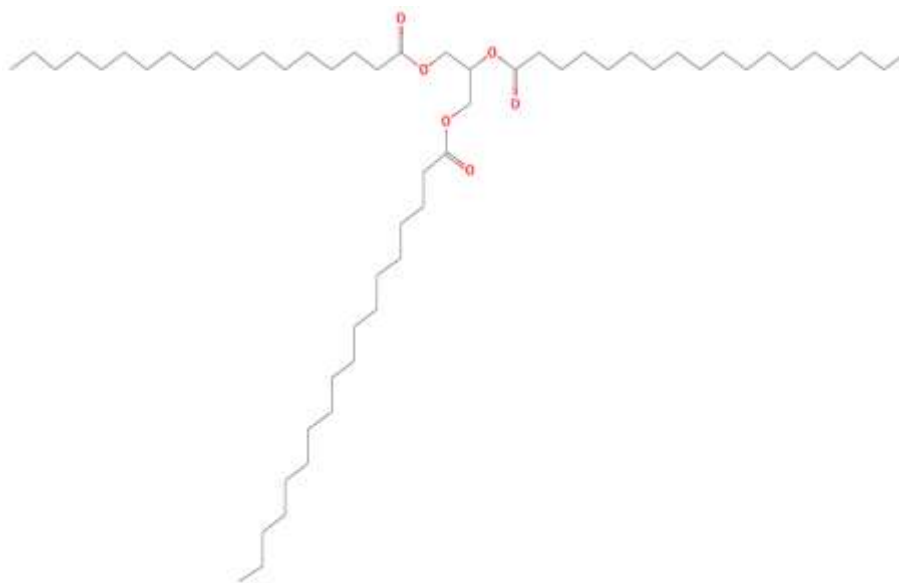
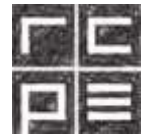


Figure 16: Structure of Tristearin (NIST, nist.gov)

### 7.3.2 Polysorbat 65 (Tween 65)

Chemical Formula:  $C_{100}H_{194}O_{28}$

Molecular weight: 1138.7551g/mol (ChemIDplus)

Melting point: 30-35°C (Hager, 1995)

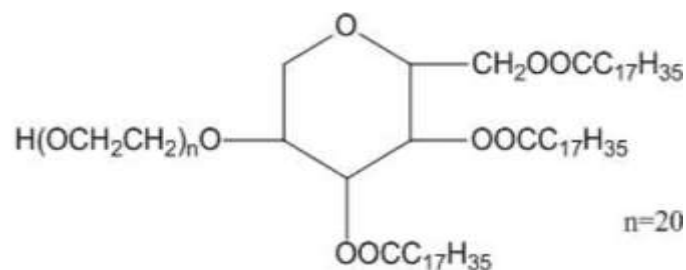


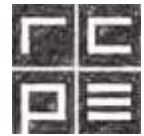
Figure 17: Structure of Polysorbat (IROGroup)

## 7.4 Experimental Methods

### 7.4.1 Hot Melt Coating

A Design of Experiments (DOE) was used to study the effect of process parameters on the polymorphic behaviour of lipid as coating material. The matrix of design is displayed in Table 4. From previous experiments it is known that the lipid crystallizes in  $\alpha$  polymorph, when the process temperature is selected below the melting temperature of  $\alpha$ -form (54°C) and the  $\beta$ - polymorph forms by adjusting the process temperature above melting temperature of  $\alpha$  but below the melting temperature of  $\beta$ -form (73°C).

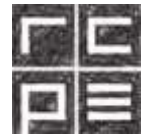
The parameters that were varied were: Inlet temperature (°C), Spray Rate (g/min), Air Flow (m<sup>3</sup>/h) and the Spray Liquid (Pure Tristearin (marked as 1 in Table 4) or a



Tristearin and Polysorbat 65 mixture (2)). For the experiments 600 g of NAC were weighted and after starting the process, filled in the chamber over a filling hose. The hot melt excipient was molten at 80°C and the spray process was started when the particles were properly fluidized. The task was to coat the particles with 70% of their starting mass, which is 420 g of coating material. The experiments with Tristearin and Polysorbate 65 were done with 14% Polysorbat (58.8 g) and 86% Tristearin (361.2 g).

**Table 4: The matrix of input parameters for the DoE on Innojet Ventils**

<b>Exp. Number</b>	<b>Exp. Name</b>	<b>Spray liquid</b>	<b>Air flow (m<sup>3</sup>/h)</b>	<b>Spray rate (g/min)</b>	<b>Temperature (°C)</b>	<b>Time (min)</b>
1	N1	1	50	4	30	105
2	N7	1	50	7	60	60
3	N8	1	75	7	60	60
4	N5	1	50	4	60	105
5	N4	1	75	7	30	60
6	N6	1	75	4	60	105
7	N20	1	62.5	5.5	45	76.4
8	N3	1	50	7	30	60
9	N17	1	62.5	5.5	45	76.4
10	N18	2	62.5	5.5	45	76.4
11	N19	2	62.5	5.5	45	76.4
12	N13	2	50	4	60	105
13	N16	2	75	7	60	60
14	N21	2	62.5	5.5	45	76.4
15	N14	2	75	4	60	105
16	N15	2	50	7	60	60
17	N10	2	75	4	30	105
18	N9	2	50	4	30	105
19	N11	2	50	7	30	60
20	N2	1	75	4	30	105
21	N12	2	75	7	30	60



## 7.5 Simulation in AVL Fire® and XPS

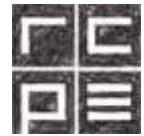
The simulations were done in a coupled CFD-DEM simulation in AVL Fire® and XPS. The varied parameters to validate the results are shown in Table 5 and the constant parameters for the simulations are shown in Table 6.

**Table 5: Variable simulation parameters**

Case Number	Temperature (°C)	Air flow (m <sup>3</sup> /h)	Spray rate (g/min)	Initial Wall Temp. (°C)	Initial Particle Temp. (°C)	Exp. Name
5	60	75	4	30	60	N6
6	30	75	7	30	30	N4
7	60	75	7	30	25	N8
8	45	62.5	4	30	45	N20
9	30	50	4	30	30	N1
10	60	50	7	30	60	N7
11	45	62.5	5.5	45	45	N18
12	30	50	7	30	30	N3
13	60	75	7	60	60	N8

**Table 6: Particle simulation parameters**

Type of Particles	N-acetylcysteine
Number of particles	13162948
Mean radius (m)	0.0000236
Sigma radius (m)	0.000077
Maximum radius (m)	0.00315
Minimum radius (m)	0.000125
Normal force model	Cohesion Mepa
Tangential model	Linear Spring-Dashpot



## 7.6 Analytical Methods

### 7.6.1 Particle Size Measurement

The particle size distribution was measured with the high-speed sensor QicPic from Sympatec GmbH (Clausthal-Zellerfeld, Germany). The dispersion was done with a RODOS dry disperser. The particle size range was from 20–6820  $\mu\text{m}$  and 400 frames per second were taken. This data was taken for the simulation of the particle movement and the spraying process in the CFD-DEM simulations.

### 7.6.2 Small Angle X-ray Spectroscopy (SAXS)

The qualitative crystal morphology measurement was done with a Kratky SAXS compact camera from HECUS X-ray System in Graz, Austria in collaboration with an X-ray generator from Seifert (Augsburg, Germany). The operation parameters were 50 kV and 1 mA for an exposure time of 20 minutes. The analysed materials were pure Tristearin and a Tristearin & 14% Polysorbate 65 mixture in triplicated samples. The analysis of the data was done with SwaxsOphone and Python.

### 7.6.3 Differential Scanning Calorimetry (DSC)

For the quantitative crystal morphology measurements a 204 F1 Phoenix DSC from Netzsch GmbH (Selb, Germany) was used. The DSC measurements were done under  $\text{N}_2$  atmosphere with 9 sections from -20 °C to 90 °C with 5 K/min heating or cooling, respectively. All samples were done in triplicates. For the evolution of the data Netzsch Proteus-61 was used.

### 7.6.4 Dissolution

The dissolution test triplicates were done in a USP 2 offline system (Ewerka, Heusenstamm, Germany). In Table 7 the specifications for the dissolution experiments are shown. The sample was taken automatically with a size at each sample point of 1.5 ml into HPLC vials for analysis. The removed sample volume was not substituted.

**Table 7: Parameters of the Dissolution experiments**

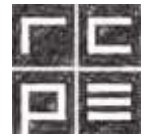
Sample	1200 mg of NAC particles coated with Tristearin or Tristearin & Polysorbate 65
Mixing device	Paddle mixer
Rotational speed	100 (rpm)
Medium	Water
Volume	900 (ml)
Temperature	37 ± 0.5 (°C)
Sampling intervals (Tristearin)	5, 15, 30, 45, 60, 120, 240, 480, 720, 960, 1200, 1440 (min)
Sampling intervals (Tristearin & Polysorbate 65)	5, 10, 20, 30, 45, 60, 120, 150 (min)

### 7.6.5 High Pressure Liquid Chromatography (HPLC)

The triplicates of the dissolution tests were analysed in a HPLC with the parameters presented in Table 8. For the calibration 10 standards were made from 0.025 mg/ml to 6.070 mg/ml of N-acetylcystein.

**Table 8: Parameters of the HPLC analysis**

Instrument	Agilent 1260 (Santa Clara, USA)
Column	Merck, Purospher STAR, RP-18e (5µm), Hibar RT 150-4,6 (Darmstadt, Germany)
Mobile Phase	5% Acetonitrile in 95% Water at pH 1.6 (with Orthophosphoric acid)
Flow rate	1 ml/min
Wavelength	220 nm
Injection volume	20 µm
Column temperature	21°C
Sample temperature	5°C
Duration	9 minutes



## 8 Results & Discussion

The goal of this work was to verify a CFD-DEM simulation of a HMC process on the Innojet Ventilus with around 13 million particles with a known PSD from an image analysis (Figure 49 & Figure 50). The validation cases were selected from the experiments (Table 4). The process was simulated for a time of 10 seconds with a calculation time of around 1 second per day. For the validation of the CFD-DEM simulations experiments were done to produce hot melt coated particles in the Ventilus with  $\alpha$  or  $\beta$  crystal lattice configuration. The configuration was analysed with a DSC measurement and confirmed with WAXS study. Furthermore in some experiments the particles were coated with Tristearin and 14% Polysorbate 65 to see the difference between crystal structure and dissolution behaviour of coated particles using pure Tristearin and the Tristearin & Polysorbate 65 mixture as coating material at different process temperatures.

### 8.1 DSC and WAXS measurements

Since the melting points of the  $\alpha$  &  $\beta$  configurations are known (Table 3) they could be identified in the DSC curves. In Figure 18 the curves of the first heating cycle for the experiments N2 (using an inlet temperature of 30°C, which is below the melting point of  $\alpha$ -form) and N5 (inlet temperature of 60°C, between the melting points of  $\alpha$ - and  $\beta$ -forms) are shown. The coating material of these two experiments is pure Tristearin and it is expected that after process the coating is completely in  $\alpha$ -form in case of N2 sample and in  $\beta$ -form in case of N5 sample.

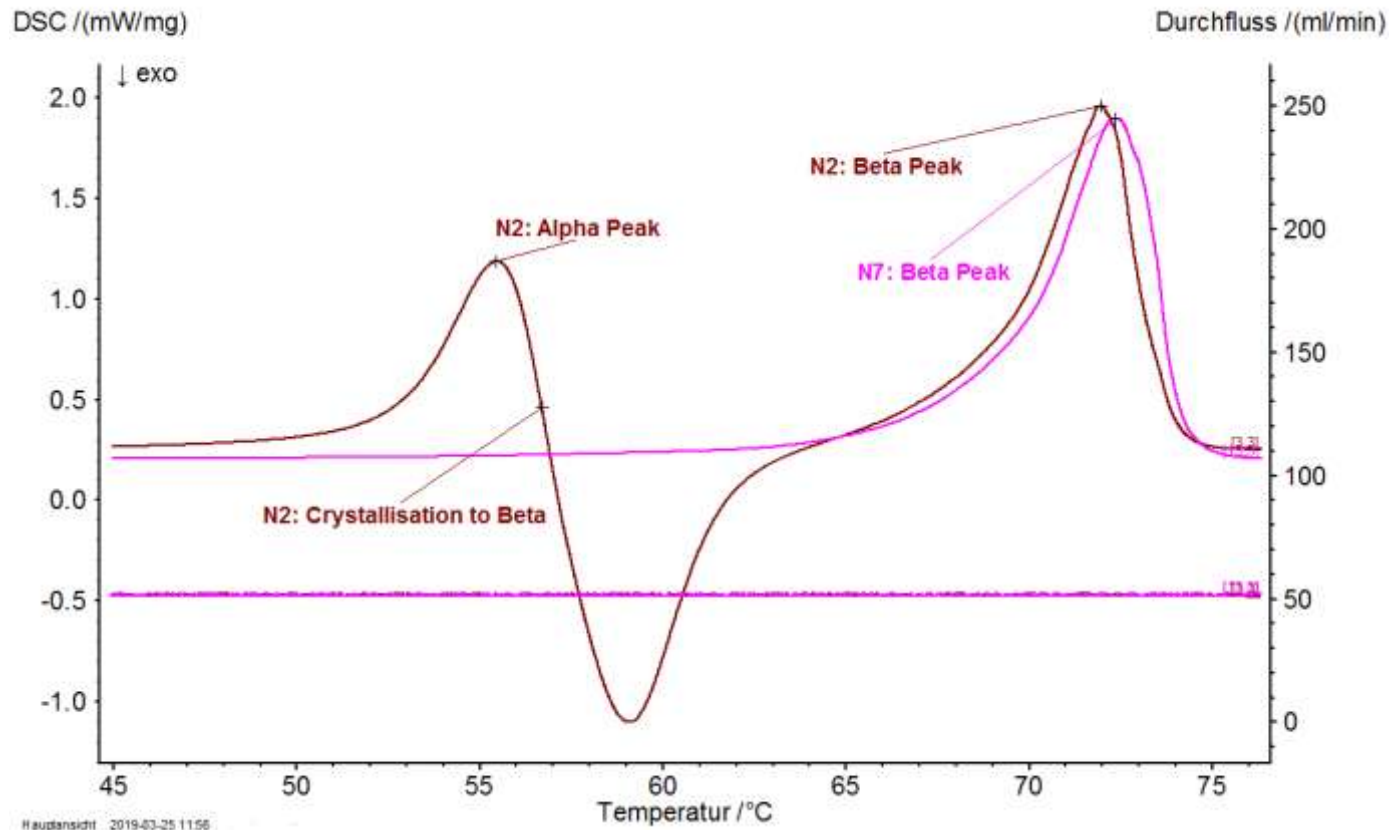
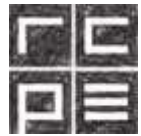
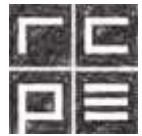


Figure 18: N2 (30°C) & N5 (60°C) DSC curves. The exothermic transitions are in the negative y-direction. There is a distinct alpha peak, a recrystallization and a beta melting peak for N2 and only a beta peak for N5 and shows exactly the difference between alpha and beta morphology behaviour in the DSC

The DSC data shown in Figure 22 confirm this assumption. The thermograms of all DoE samples provided with an inlet temperature of 30 °C showed the existence of  $\alpha$ -form in the coating. The alpha form is very unstable and a crystal structure change to beta is very likely to happen over time, even in cooled environment. There were also traces of alpha configuration in experiment N18, performed with inlet temperature of 45°C, but the alpha configuration could not be confirmed with the WAXS studies (Figure 51). For the experiments with the inlet temperature at 60°C the coated particles had no measurable content of  $\alpha$ -form, this also counts for the experiments with the Tristearin-Polysorbate 65 mix. The WAXS analysis confirmed that no  $\alpha$  configuration was found in the samples provided with high inlet temperature and mixtures of Tristearin and Polysorbate 65. Which was expected due to the findings of Becker et al. (Becker, et al., 2016). After the coating process the particles were put in plastic bags and stored in a fridge.



### 8.1.1 Model fit: Morphology

The DoE was fitted to get the influencing input parameters. The coefficient plot (Figure 19) shows a significant influence of the inlet temperature (Temp) on alpha and beta polymorphic form. The temperature has a negative influence in the alpha morphology (left), which means with increasing temperature the proportion of alpha decreases. In contrast to the beta morphology, which increases with increasing temperature. Figure 20 is the contour plot to show how the temperature influences the proportion of alpha to beta morphology. It confirms the coefficient plot, the increase of temperature decreases alpha morphology and increases the beta morphology.

The model fit R2 showed 0.57, the parameter for the robustness of a future model showed 0.56, the validity of the model is 0.58 and the reproducibility is 0.59. It's obvious that more experiments need to be performed to get better parameters in all categories.

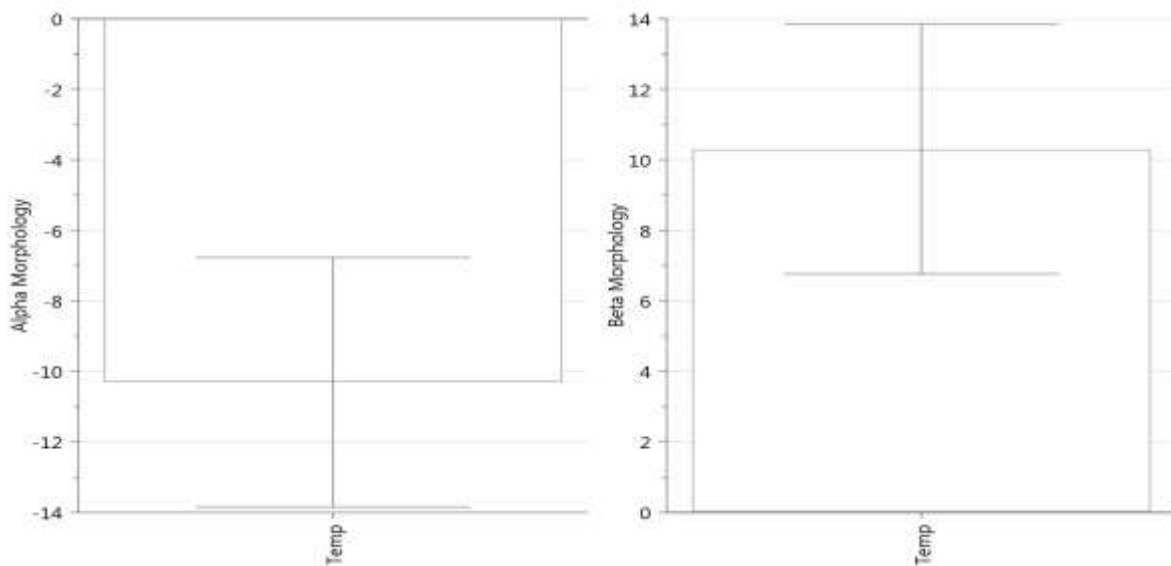


Figure 19: Coefficient plot significant influences on crystal structure (alpha-left, beta-right)

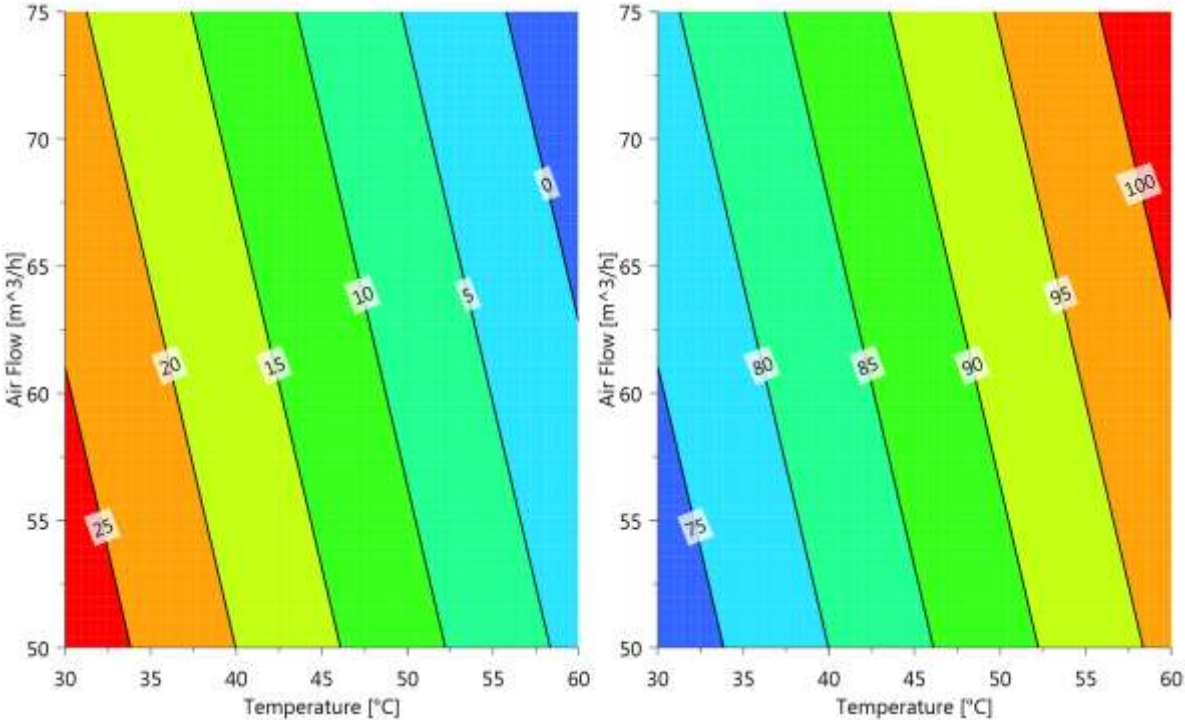
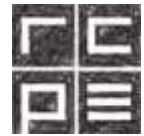


Figure 20: Contour Plot of the influencing parameters on the proportions of alpha (left) and beta (right) morphology



## 8.2 Dissolution

The dissolution tests for the experiments with the particles coated with pure Tristearin were done for 24 hours for all temperatures (30°C, 45°C, 60°C). The results were compared to the results of (Lopes, et al., 2015). The dissolution rate of samples with  $\beta$  configuration was much slower compared to the  $\alpha$  configuration in the cited paper. As seen in Figure 21 there was practically no release from microcapsules, neither from coatings containing  $\beta$ -polymorph nor from coatings containing  $\alpha$ -polymorph after 24 hours. The highest detected released amount was about 0.08 % for microcapsules containing  $\beta$ -polymorph, which is in the same scale as the compared results but in an opposite direction. As in the cited paper the release of NAC from microcapsule with  $\beta$  configuration was slower than the release from those with  $\alpha$ -form. (Lopes, et al., 2015). Moreover, at that study the NAC release from microcapsules with  $\alpha$ -form was 45% after 24 h, which is much higher than achieved release in this study. This is most probably due to the more dense and perfect coating of NAC crystals with pure lipid in the current study. Despite the fact that the  $\beta$ -form provides a more dense subcell arrangement with tilted lamellas, resulting in a more water repellent surface compared to the  $\alpha$ -form, there was in fact no release of NAC from both coatings.

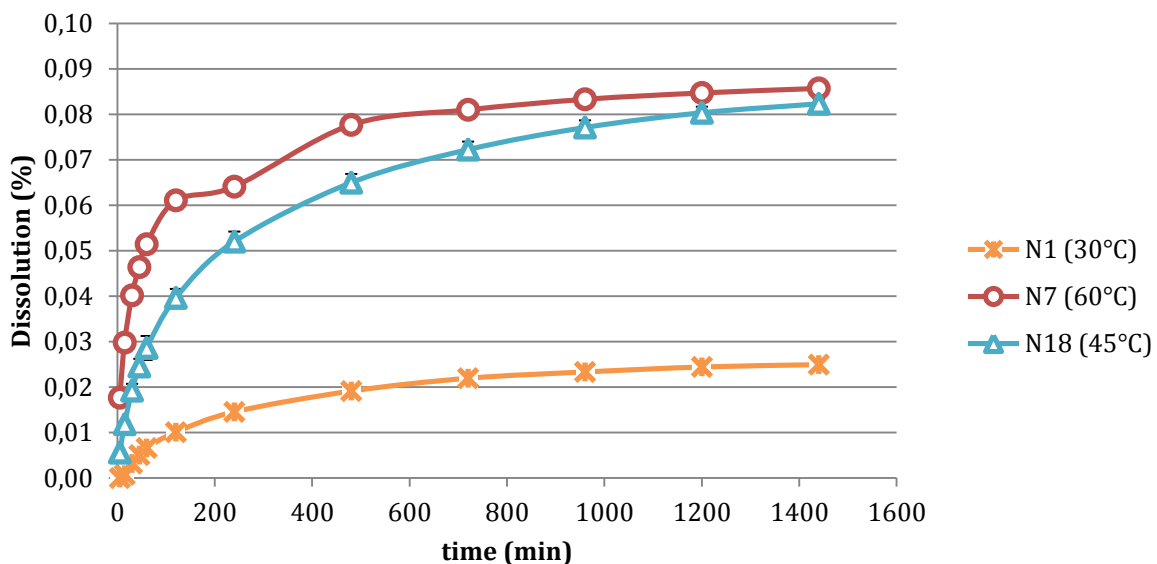
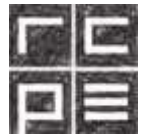


Figure 21: Mean dissolution of the triplicates in % over time for the experiments N1, N7, N18 with pure Tristearin and different temperatures

For the experiments with a mixture of Polysorbate 65 and Tristearin the dissolution rates were much higher. This is due to the water solubility of Polysorbate 65 and acting as pore-former in the coating formulation and the reason for selecting 2.5 hours as



dissolution time. The output (response) parameters for this DoE were selected as release (%) after 5 minutes and 30 minutes of dissolution test as indicator for taste masking and immediate release behaviour. Since Polysorbate 65 has a HLB value of 10 and therefore is soluble in water which makes the release of NAC from coatings drastically faster than coatings without emulsifier.

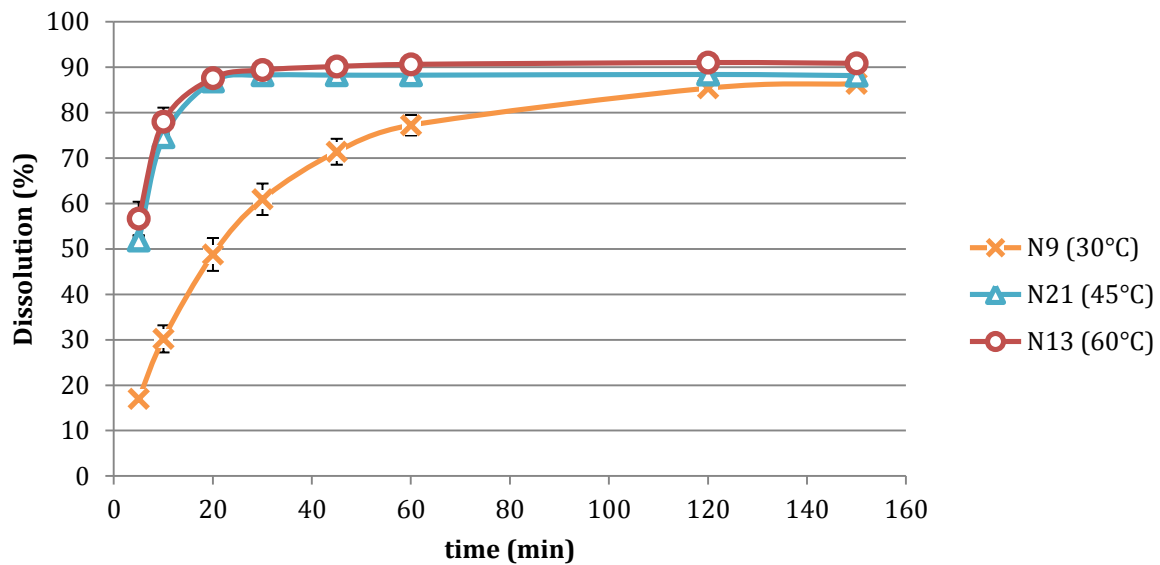
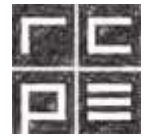


Figure 22: Dissolution in % over time for the experiments with Tristearin-Polysorbate 65 mixture

### 8.2.1 Model fit: Taste Masking and immediate release behaviour

The Full factorial process model showed that the dissolution after 5 minutes is significantly influenced by temperature (Temp), spray rate (Spr), spray rate \* temperature (Spr\*Temp) and the quadratic temperature term (Temp\*Temp). For the dissolution after 30 minutes the significant parameters are airflow (Air), temperature (Temp), temperature \* airflow (Air\*Temp) and the quadratic temperature



(Temp\*Temp) displayed in Figure 23.

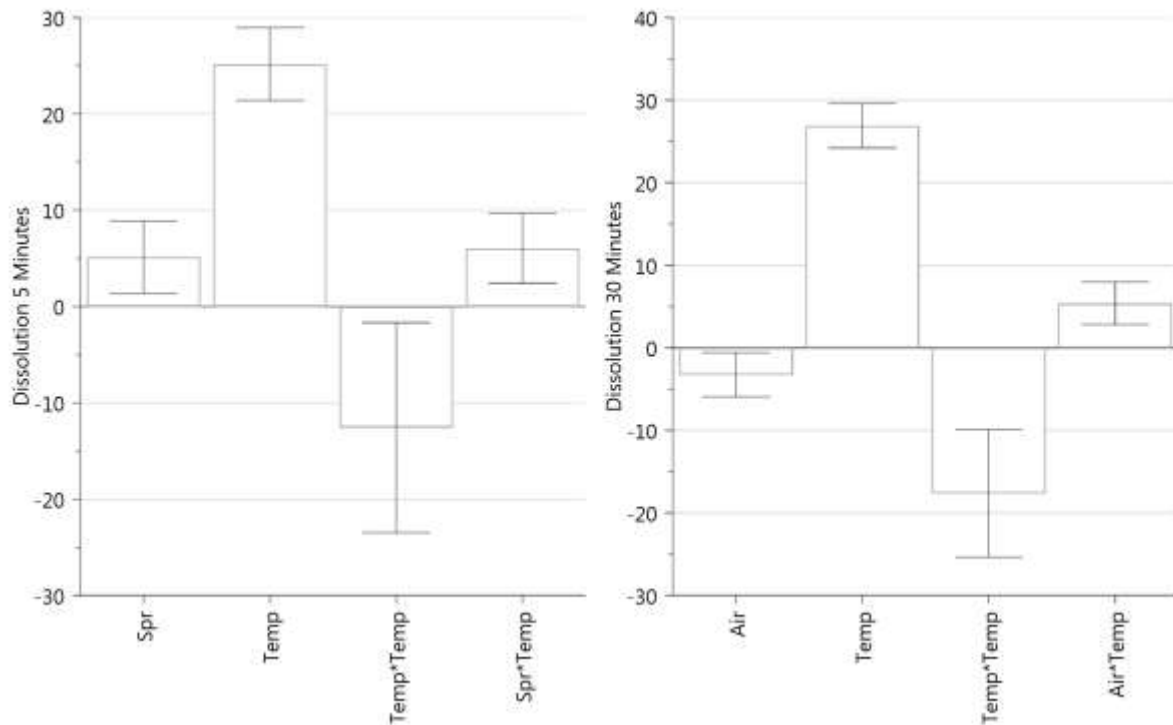


Figure 23: Coefficient plot of the Dissolution after 5 (right) and 30 minutes (left)

The contour plots for the two dissolution experiments are Figure 24 & Figure 25. The influence of the temperature on the process is unambiguously. In Figure 24 (Dissolution after 5 minutes) the spray rate has significant influence on the dissolution but only for higher temperatures as 45°C. Higher inlet temperature and higher spray rate result in agglomeration instead of coating, which is due to the spraying of high amounts of lipid per unit of time without sufficient time in the process container to completely recrystallize on the surface of particles and form a film. Therefore, the dissolution is still too fast to be around the value of taste masking which would be 10% after 5 minutes (Gittings, Turnbull, Roberts, & Gershkovich, 2013). An immediate release profile was defined as (Figure 25), at least 85% release of API within 30 minutes (World Health Organization, 2006). The influential parameters are the airflow and temperature. The dissolution is slower with higher airflow, which is due to the higher particle velocity and shorter particle-particle contacts what leads to less agglomeration, thereby better coating and slower dissolution behaviour (Figure 29).

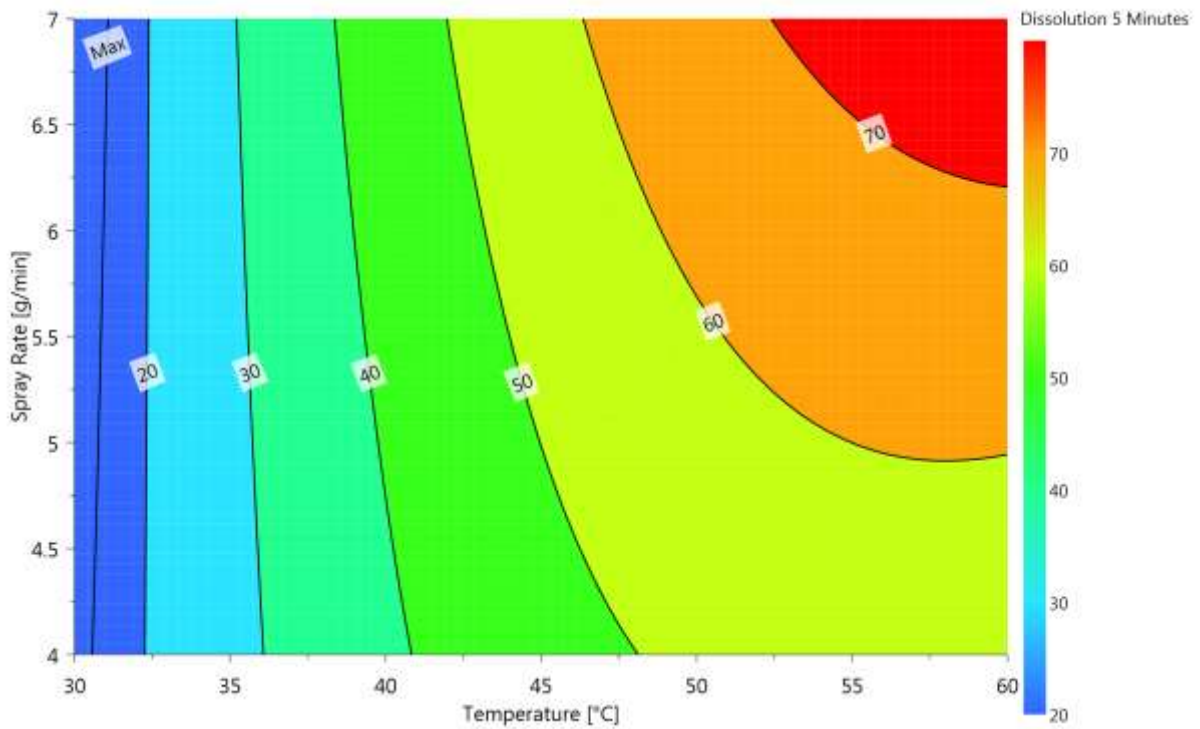
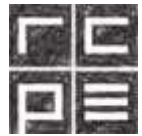


Figure 24: Contour plot for the dissolution after 5 minutes

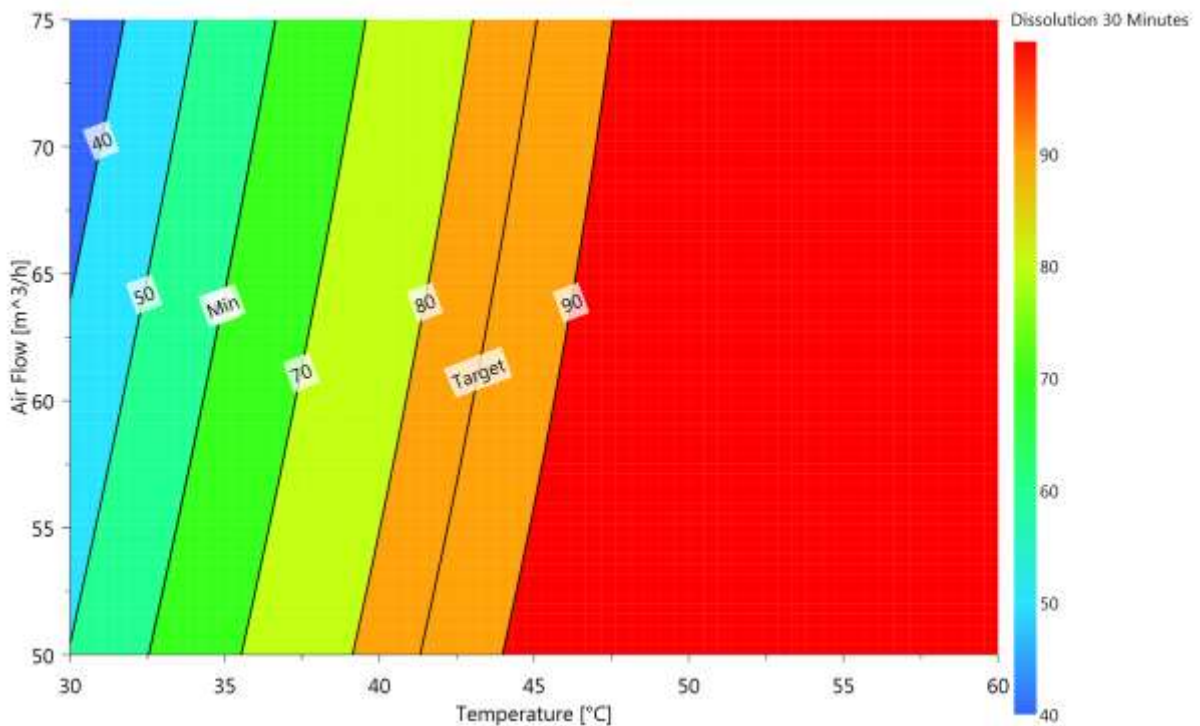
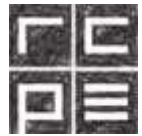


Figure 25: Contour plot for the dissolution after 30 minutes

The model fit R2 showed 0.99, the parameter for the robustness of a future model showed 0.98, the validity of the model is 0.24 and the reproducibility is 0.99. All input parameters showed influence on the dissolution rate.



### 8.3 CFD –Simulations

As preparation for the CFD-DEM coupled simulations a set of CFD simulations were done to calculate the heat flow over the fluid bed boundary and also to specify the simplifications for the coupled simulations which are computationally more expensive. Figure 26 & Figure 27 are examples for the CFD simulations in AVL Fire. The flow is getting colder near the wall due to the heat transfer to the ambient. The flow is accelerated in the nozzle and the distributor plate (detail in Figure 27).

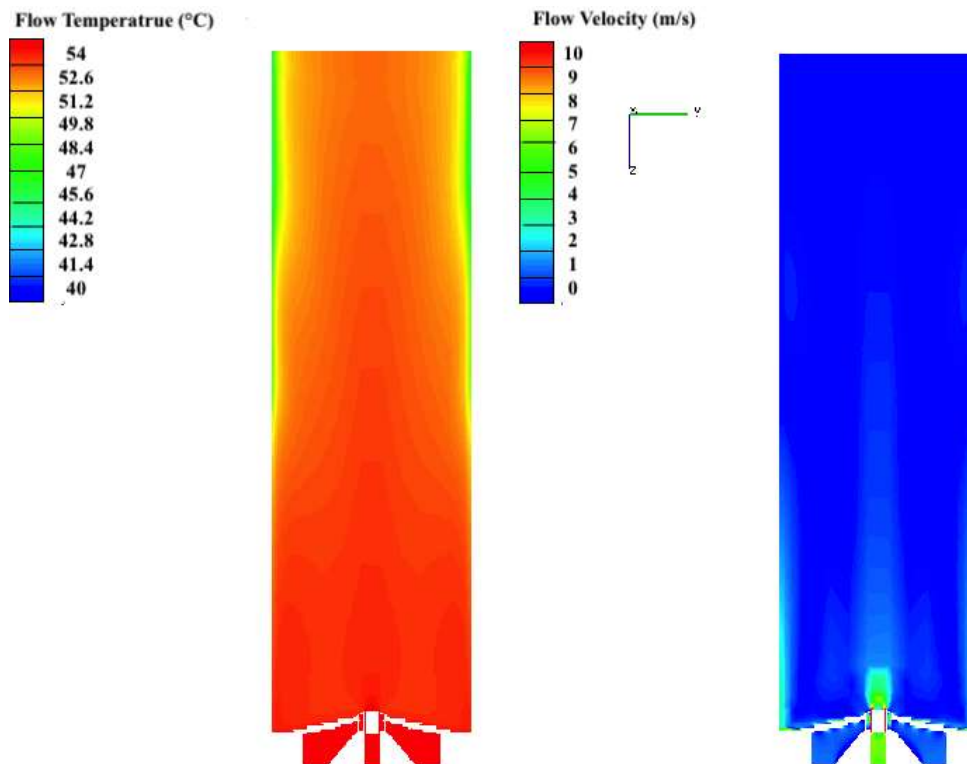


Figure 26: Examples for the CFD situations with Temperature (left) and Velocity (right) of the fluid flow

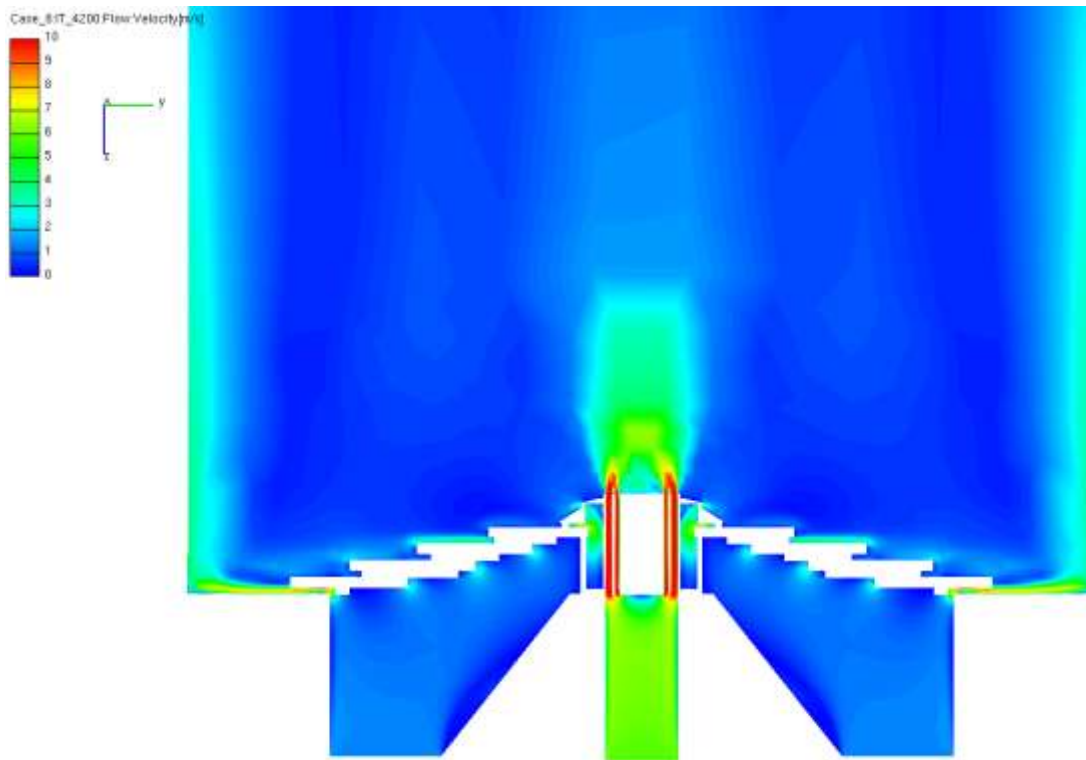
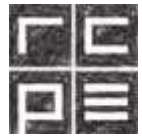


Figure 27: Detail of the fluid flow velocity of the CFD simulation geometry

For the coupled simulations the geometry was simplified and the heat transfer to the ambient and the heat transfer coefficient were calculated from the CFD results.

## 8.4 CFD-DEM Coupled Simulations

### 8.4.1 Particle Size Distribution

In Figure 28 the experimental PSD of NAC particles from a QICPIC analysis is compared to the PSD that was generated by XPS with the input parameters shown in Table 6. Figure 28 shows that the computer generated PSD fits well. Except in the region of small particles ( $<250 \mu m$ ) the cumulative distribution doesn't fit. Which is due to the  $x_{10}$  of the NAC particles is  $251.75 \mu m$  and this was considered as the smallest particle size for the simulations (See Figure 49). For the largest particles the  $x_{99}$  was taken into account, which makes the error smaller in the upper regions.

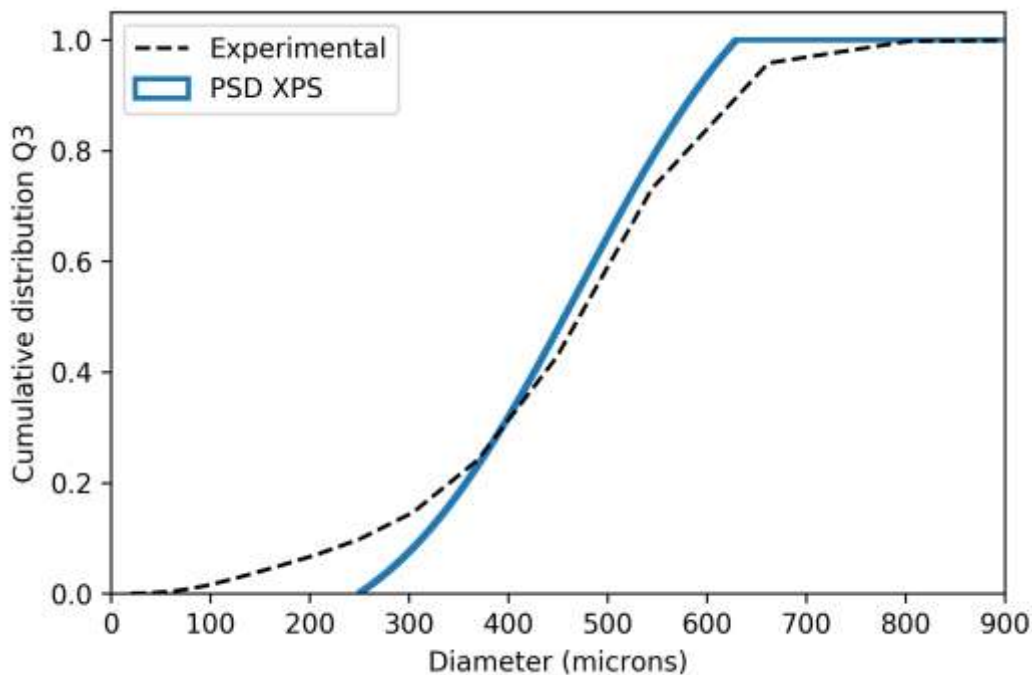
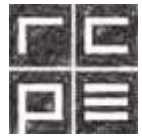


Figure 28: Comparison of the Cumulative distributions of NAC particles in experiment and simulation

#### 8.4.2 Particle mean velocity magnitude

To further investigate the particle agglomeration mentioned in the Chapter Model fit: Taste Masking the mean particle velocity was analysed in the CFD-DEM simulations. Due to higher particle velocity the contact times between the particles are shorter and that leads to less chance for agglomeration. Figure 29 shows that the particles with the highest airflow ( $75\text{m}^3/\text{h}$ ) have the highest mean velocity and therefore the least likelihood of agglomeration and the lowest airflow ( $50\text{m}^3/\text{h}$ ) has the highest likelihood of agglomeration. A histogram of the particle velocities was done (Figure 30) to show the distribution of the three different airflow velocities.

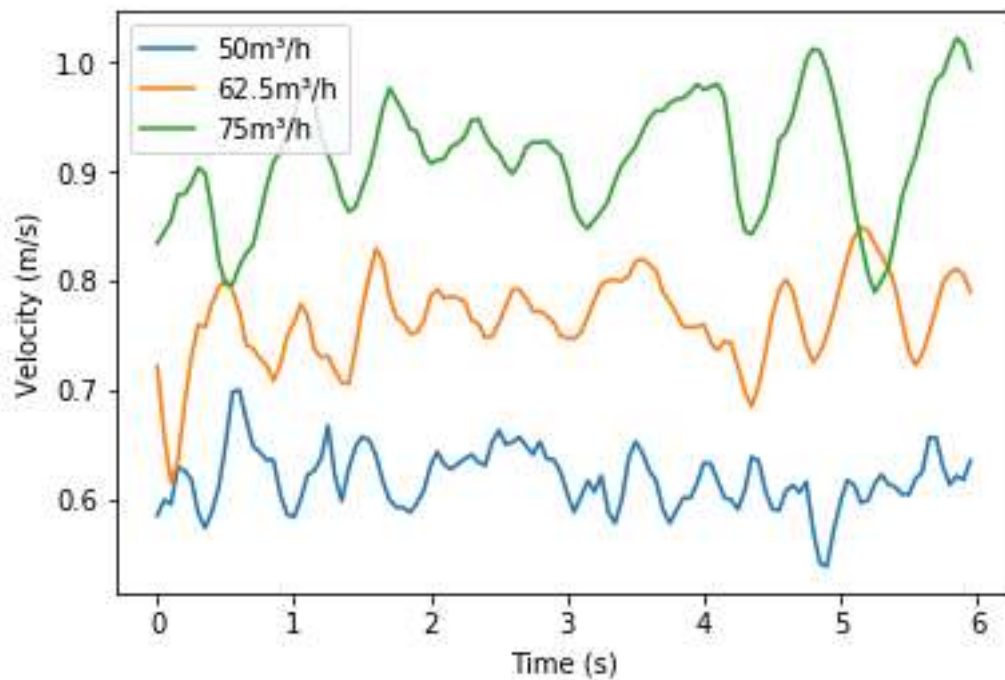
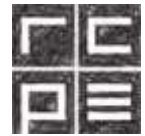


Figure 29: Particle mean velocity magnitude after 1.5 seconds till 7.5 seconds for three different airflow speeds

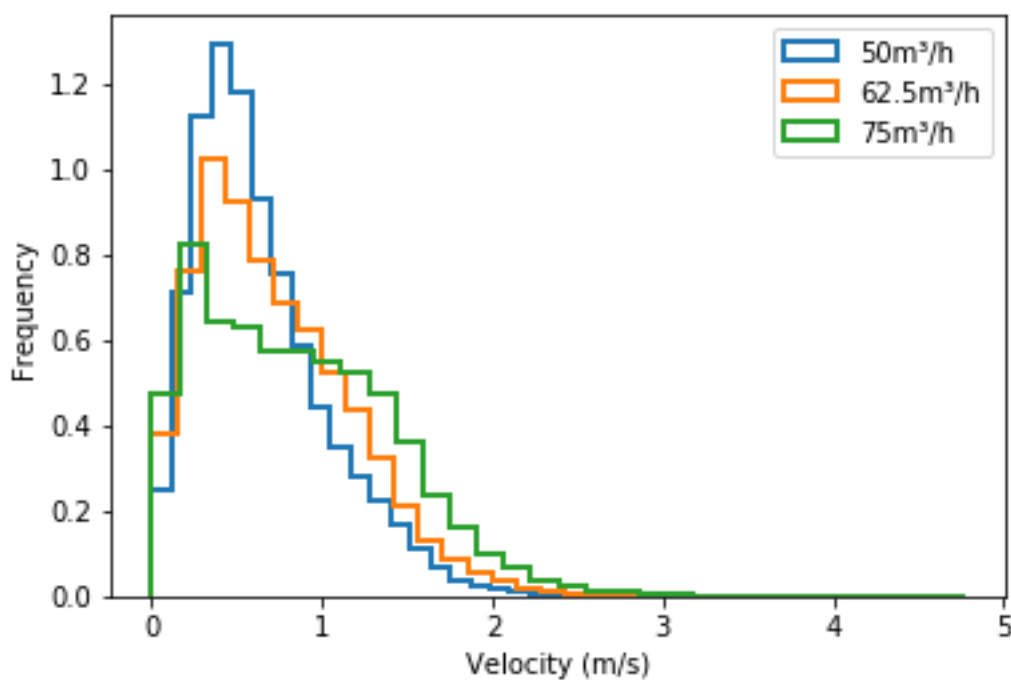
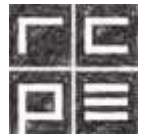


Figure 30: Histogram of the Particle mean velocity magnitude for three different airflow speeds

### 8.4.3 Mixing radial

The mixing of the particles in the fluid bed was simulated for 3 different airflows (50, 62.5, 70 m<sup>3</sup>/h). The mixing is calculated as:



$$MA = \frac{\text{Mean Mixing } (t)}{\text{Mean Mixing } (t_0)} \quad (66)$$

The mixing average (MA) should be in a range of approximately 0.5. On average 50% of the particles changed from one side of the fluid bed to the other. Figure 31 shows the mixing in radial direction and starts at 1, which means completely unmixed and after one second it starts fluctuating around 0.5 with no big outlier till the end of the 10 simulated seconds. On average 0.5 of all particles are on a different side of the fluid bed at all times.

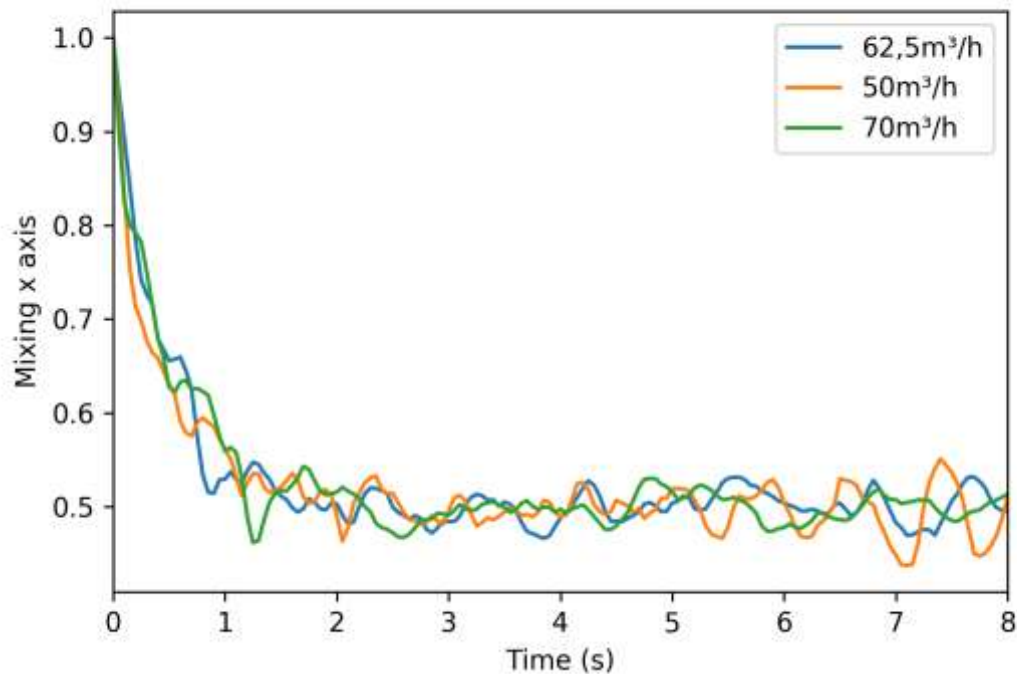


**Figure 31: Mean mixing of the particles in radial direction over time**

The development of the mixing process in the DEM-CFD simulation is presented in Figure 32. The initial of the mixing is after 2 seconds and after 3.10 seconds the particle system is completely mixed, what was expected after the calculation of the mixing average (MA).

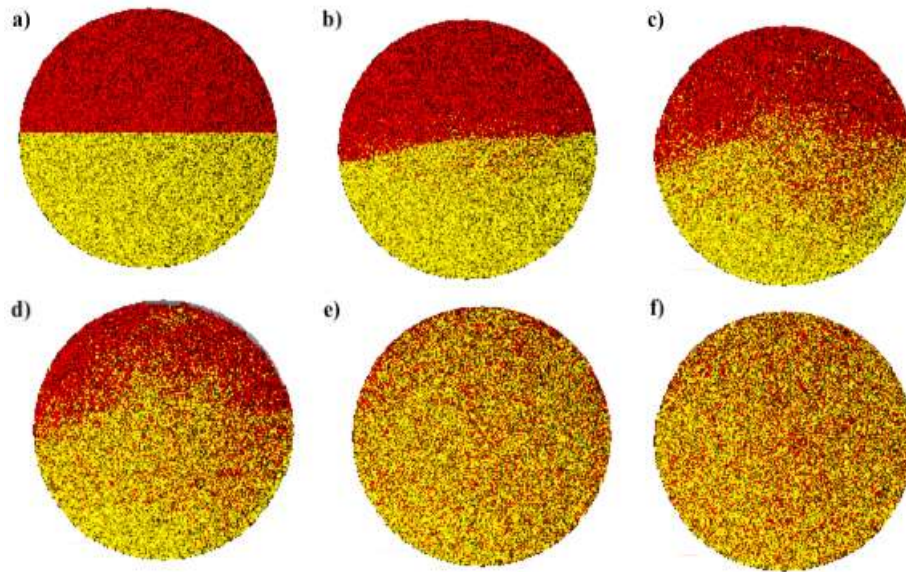
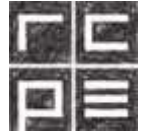


Figure 32: Mixing of Case 13 (75m<sup>3</sup>/h) in radial direction after a) 2.20 seconds (initial position); b) 2.50 seconds; c) 2.70 seconds; d) 2.80 seconds; e) 3.00 seconds; f) 3.10 seconds

#### 8.4.3.1 Lacey Mixing Index $M$ for radial mixing

For further insight in the mixing process the Lacey index was used to look at the development of the mixing process over time and use a commonly used and comparable measure. The Lacey index bounded between 0 and 1, where 0 means completely segregated mixture and 1 means perfectly mixed. The mixture of particles was divided into 2 groups (as seen in Figure 32 Point a). For a binary mixture of two fractions  $p$  and  $(1-p)$  the variance of the completely segregated mixture is calculated as

$$\sigma_0^2 = p(1 - p) \quad (67)$$

further the variance of the random mixture is given as

$$\sigma_r^2 = \frac{p(1 - p)}{n} \quad (68)$$

with  $n$  as the number of particles in the sample ( $n=6820899$  particles).

The Lacey Mixing Index is defined as

$$M = \frac{\sigma_0^2 - \sigma^2}{\sigma_0^2 - \sigma_r^2} \quad (69)$$

(Govender, Wilke, Wu, Rajamani, Khinast, & Glasser, 2018)

The development of the Lacey index over time in radial direction is displayed in Figure 33. After around 1 second the Lacey index already reaches random mixture and from 2 seconds on the Lacey index stays constant around 1 till the end of the simulated time.

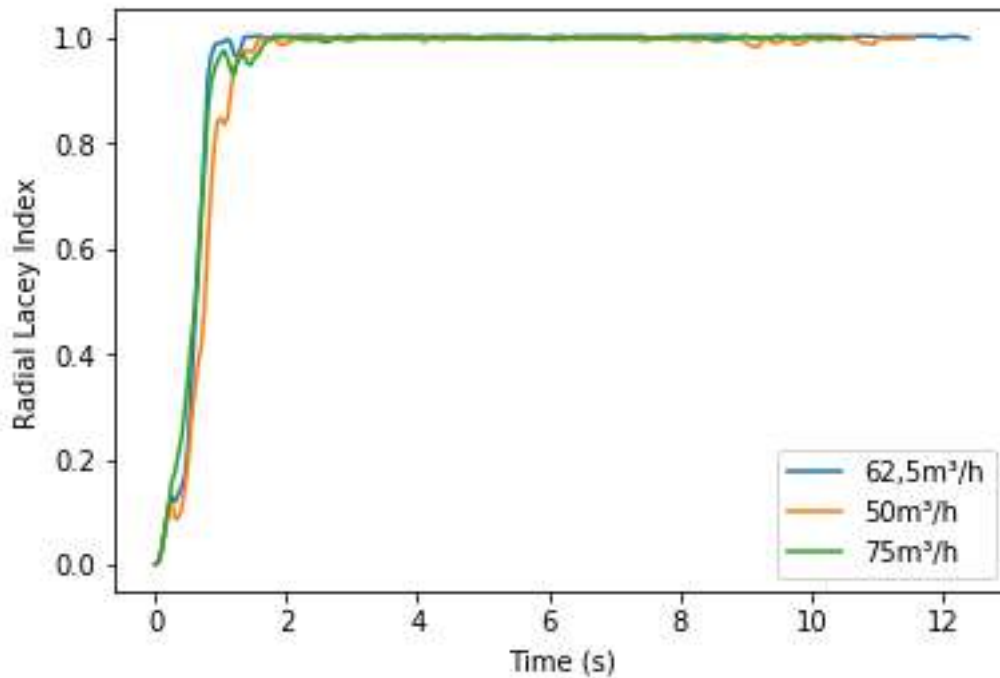
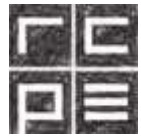


Figure 33: Development of the Lacey Index over time for 3 different airflow rates in radial direction

#### 8.4.4 Mixing axial

The same calculation was done for the mixing on the z-axis (height of the fluid bed). The mixing point was defined to be at 30 cm of 70 cm fluid bed height. Figure 34 shows, that the mixing starts at 1 and after around the first second it begins to fluctuate around 0.5 for 70 m<sup>3</sup>/h and around 0.3 for 62.5 m<sup>3</sup>/h. For the 50 m<sup>3</sup>/h the particles mixing is going down to a value around 0.2 which shows that the mixing quality of the particles over the height of the fluid bed is declining with decreasing airflow.

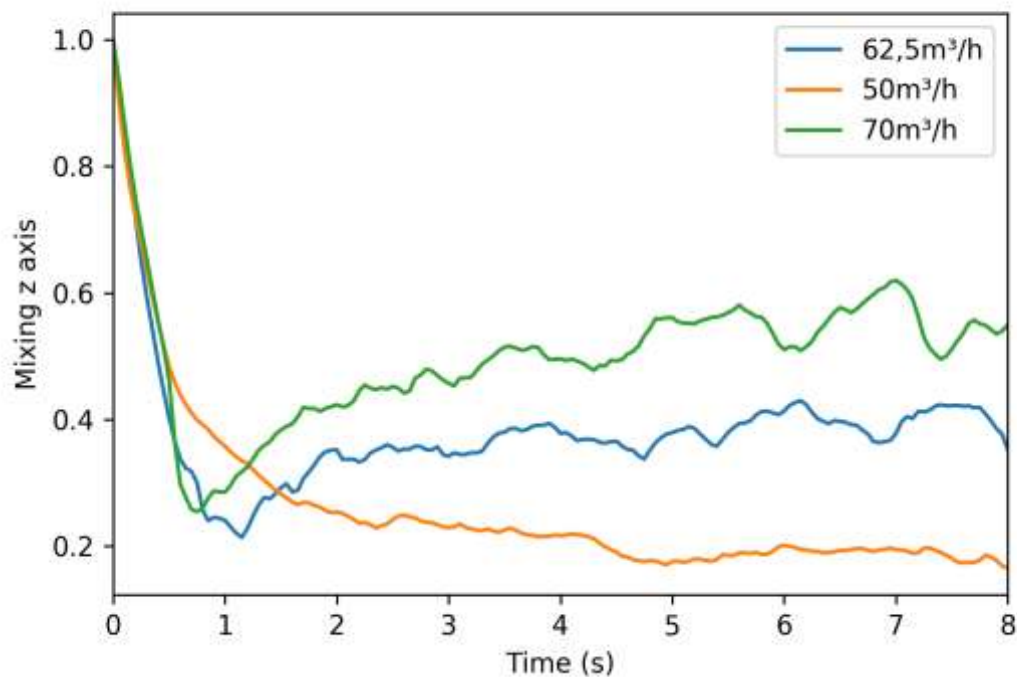
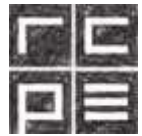


Figure 34: Mean mixing of the particles in axial direction over time

Figure 35 & Figure 36 compare the influence of the airflow velocity of Case 9 (50 m<sup>3</sup>/h) and Case 13 (75 m<sup>3</sup>/h) as seen in Figure 34 the mixing behaviour is different for the two cases. The fluidization is way better in Case 13 since in Case 9 most particles don't even reach the upper parts of the fluid bed. The mixing behaviour is still very good, as the particles mix quite well in both cases.

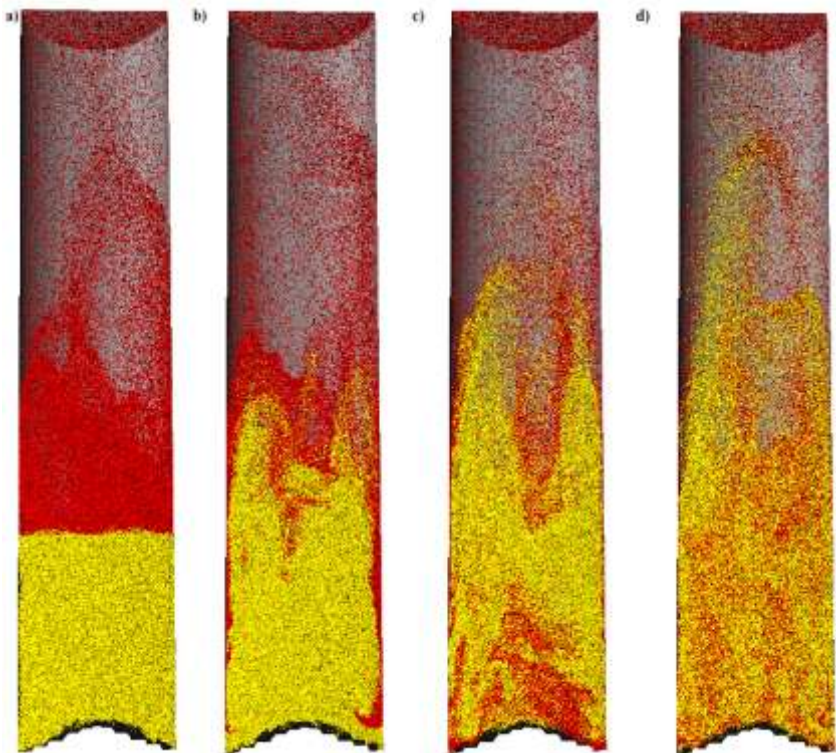


Figure 35: Mixing of Case 9 ( $50 \text{ m}^3/\text{h}$ ) in horizontal direction after a) 3.10 seconds (initial position); b) 3.30 seconds; c) 3.50 seconds; d) 3.70 seconds

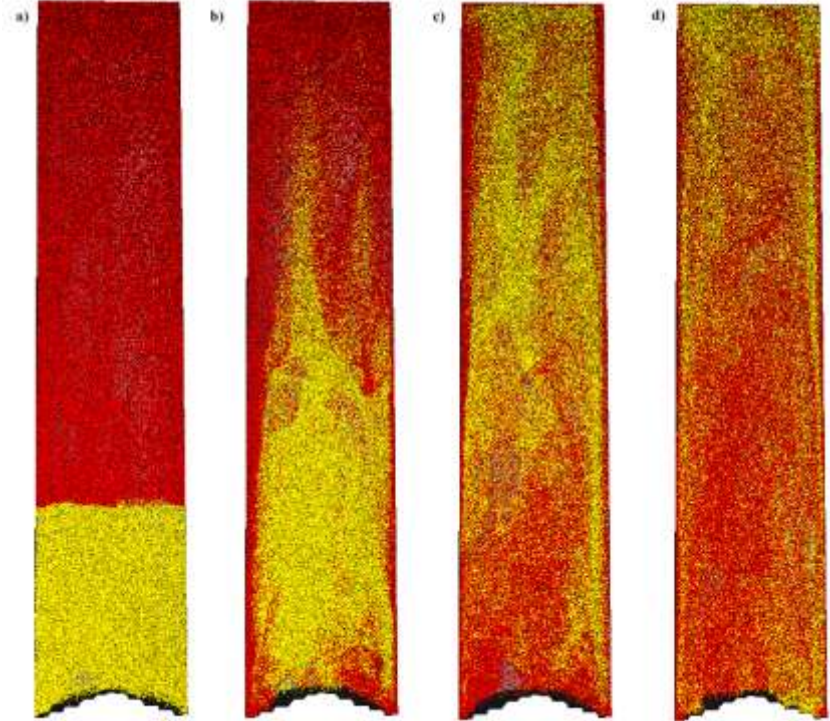
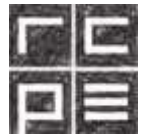


Figure 36: Mixing of Case 13 ( $75 \text{ m}^3/\text{h}$ ) in horizontal direction after a) 3.10 seconds (initial position); b) 3.30 seconds; c) 3.50 seconds; d) 3.70 seconds



#### 8.4.4.1 Lacey Mixing Index $M$ for axial mixing

The development of the Lacey index over time in axial direction is displayed in Figure 37. In difference to the radial Lacey index, the mixing quality is different for the 3 airflows. Furthermore it is interesting to see that the mixing quality increases from 50 m<sup>3</sup>/h to 62.5 m<sup>3</sup>/h and then decreases again at 75 m<sup>3</sup>/h. At 62.5 m<sup>3</sup>/h the particles stay in the considered area and the de-mixing of the 50 m<sup>3</sup>/h and 72 m<sup>3</sup>/h cases is because of particles leaving and re-entering the considered region and not due to actual de-mixing. And with a value around 0.8 it can still be considered as well mixed.

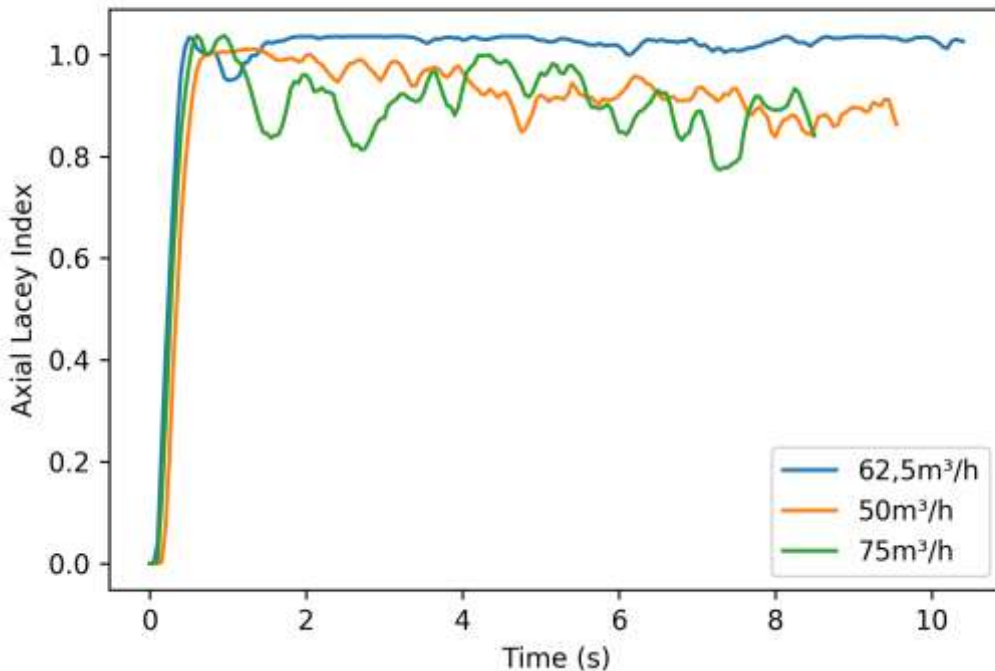


Figure 37: Development of the Lacey Index over time for 3 different air flow rates in axial direction

#### 8.4.5 Influence of initial and airflow temperature

##### 8.4.5.1 30 °C Simulations

The simulations for Case 9, Case 6 and Case 12 are shown for 10 seconds with an initial particle temperature of 25°C for Cases 9 and 6 to also get insight in the heating process during the simulation. Case 12 was initialized with 30°C particle temperature. In Figure 38 the different development of the temperature is due to the higher air flow rate in Case 6 (75 m<sup>3</sup>/h) compared to the 50 m<sup>3</sup>/h in Case 9. Case 12 is shown in more detail in Figure 39 since the temperature change is so small that it nearly resembles a straight line in Figure 38.

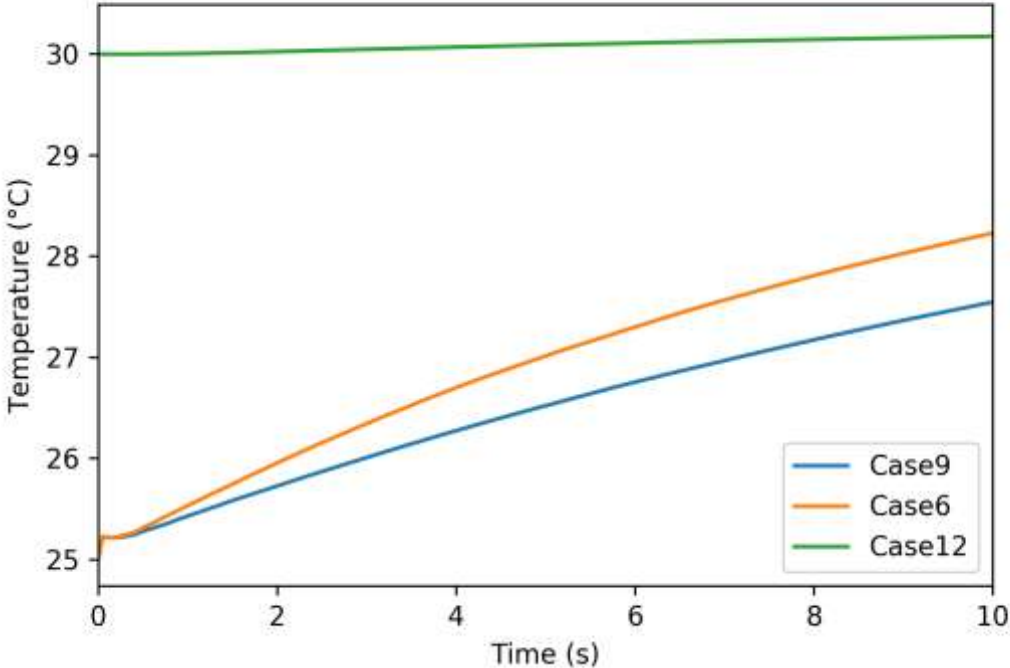


Figure 38: Change of temperature over time for the Cases 6 and Case 9 (25°C particle initial temperature) and Case 12 (30°C particle initial temperature) at 30°C grid temperature

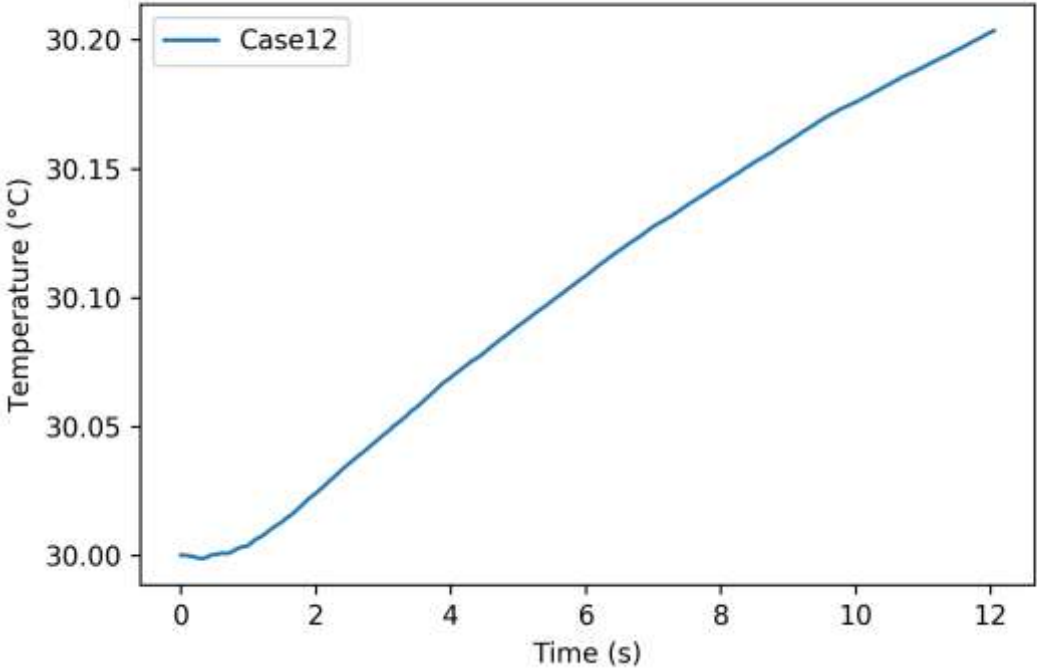
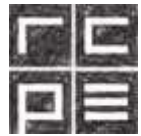


Figure 39: Change of temperature over time for Case 12 (30°C particle initial temperature) at 30°C grid temperature



#### 8.4.5.2 45 °C Simulations

The Cases 8 and 11 were run with 45°C initial particle temperature and with the same airflow and two different grid temperatures. In Figure 40 it is easy to see that the starting temperature of Case 11 is higher due to the fact that the grid is initialized at a higher temperature (45°C in Case 11 & 30°C in Case 8) in the CFD simulation and the particles cool less down at wall contact (the cooling is the drop in Figure 40 at the initialization of the simulations). There is a heat transfer from the wall to the ambient which explains the small drop even in the Case 11 with the 45°C initial wall temperature). Furthermore as the simulation progresses the larger temperature gradient in Case 8 and the heating of the wall narrows the gap between the two lines.

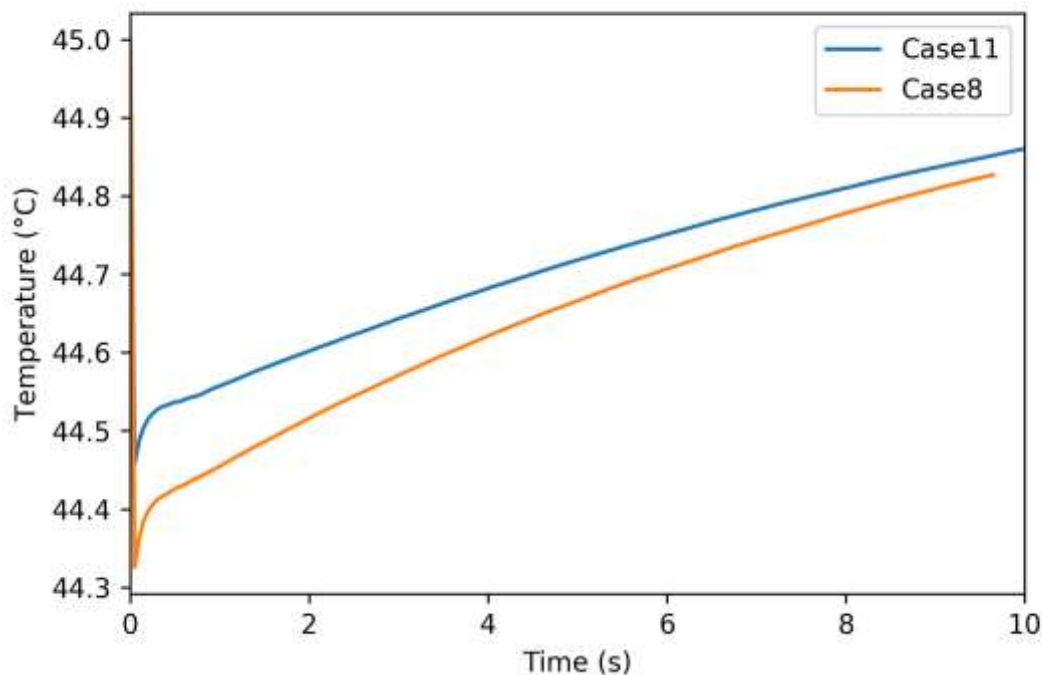
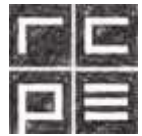


Figure 40: Change of temperature over time for the Cases 11 and 8 with 45°C particle initial temperature and 30°C grid temperature for Case 8 and 45°C grid temperature for Case 11

#### 8.4.5.3 60 °C Simulations

Also for the simulations with 60°C there were 2 simulations with different airflow rates (Case 10: 50 m<sup>3</sup>/h, Case 5: 75m<sup>3</sup>/h) and 30°C initial grid temperature and additionally simulation Case 13 with 75 m<sup>3</sup>/h and 60°C initial grid temperature was made to get rid of the cooling (seen in Figure 40 as the sharp drop at the beginning of the simulations) of the initial particles in the initialisation step (0.05 seconds) and at all wall contacts (the air is also cooled due to the wall temperature gradient and the heat transfer for the fluid



bed wall to the ambient) before the wall is heated by the air and the contacting particles. Figure 41 shows that Cases 5 and 10 have the same initial temperature (initialisation step takes 0.05 seconds and the particles are cooled down by the grid before the air-flow starts). Due to the higher flow rate in Case 5 the convective heat transport from the air flow to the particles is higher than for the particles in Case 10 which is presented in Figure 41, which is the explanation for the widening of the gap between the two simulation Cases. Case 13 is shown in more detail in Figure 42 since the temperature change is so small that it nearly resembles a straight line in Figure 41.

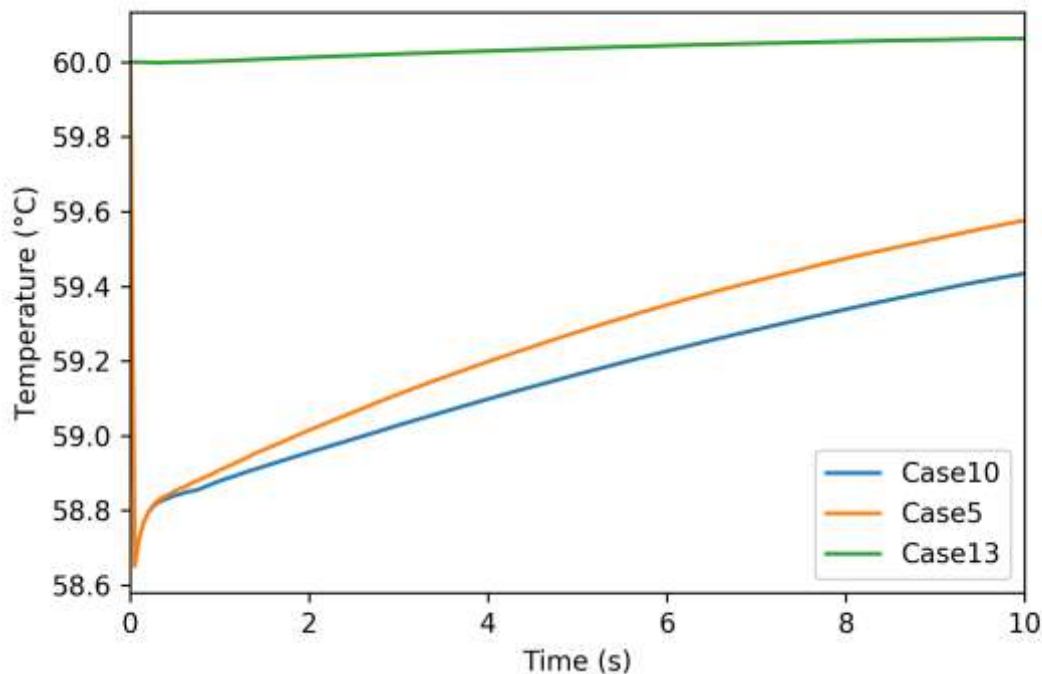


Figure 41: Change of temperature over time for the Cases 10 and 5 with 60°C particle initial temperature and 30°C grid temperature & of Case 13 with 60°C initial particle and initial grid temperature

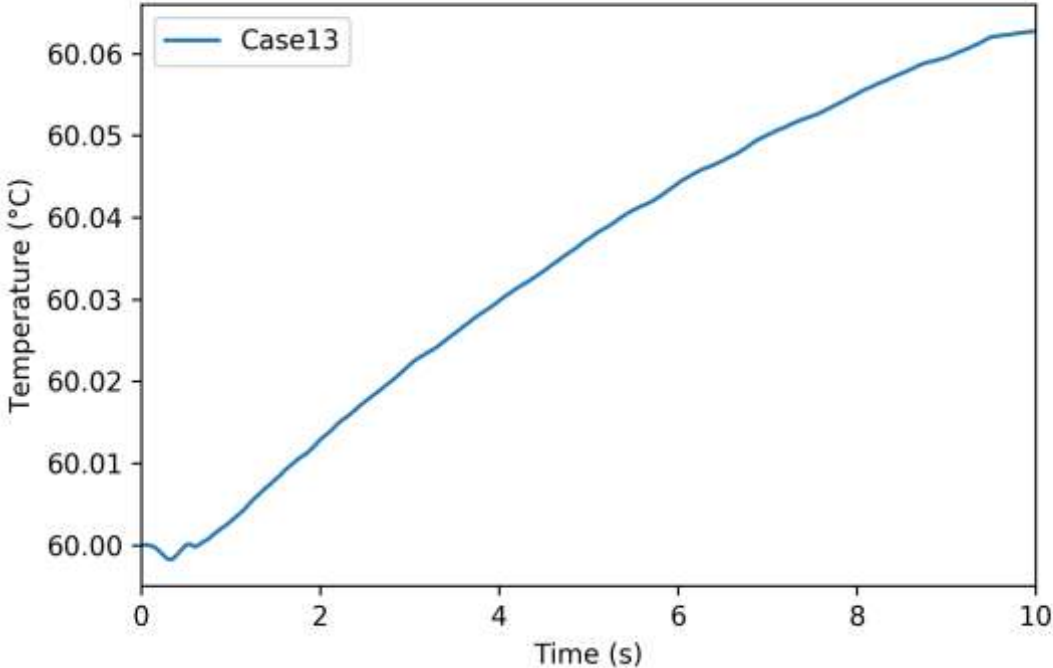
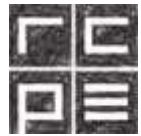


Figure 42: Change of temperature over time for Case 13 with 60°C initial particle and initial grid temperature



#### 8.4.6 Particle coating

##### 8.4.6.1 30°C: Case 9 (initial particle temperature 25°C) and Case 12 (initial particle temperature 30°C)

Figure 43 gives an impression in the influence of the coating on the particle temperature. Due to the spray liquid the mean temperature of the coated particles is higher than the overall mean temperature. XPS calculates the enthalpy of the spray liquid and transfers it on the particle. Through the influence of the wall contacts (conductive heat transfer) and the spray air (convective heat transfer) the particles are cooled down but since this heat transfer forces also act on the uncoated particles the only difference is the temperature gradient and the coated particles stay above mean temperature. In Figure 44 the initial particle temperature was 30°C (Case 12) so the gradient between air and particle temperature was zero from the start to get an even better insight in the influence of the spray liquid temperature.

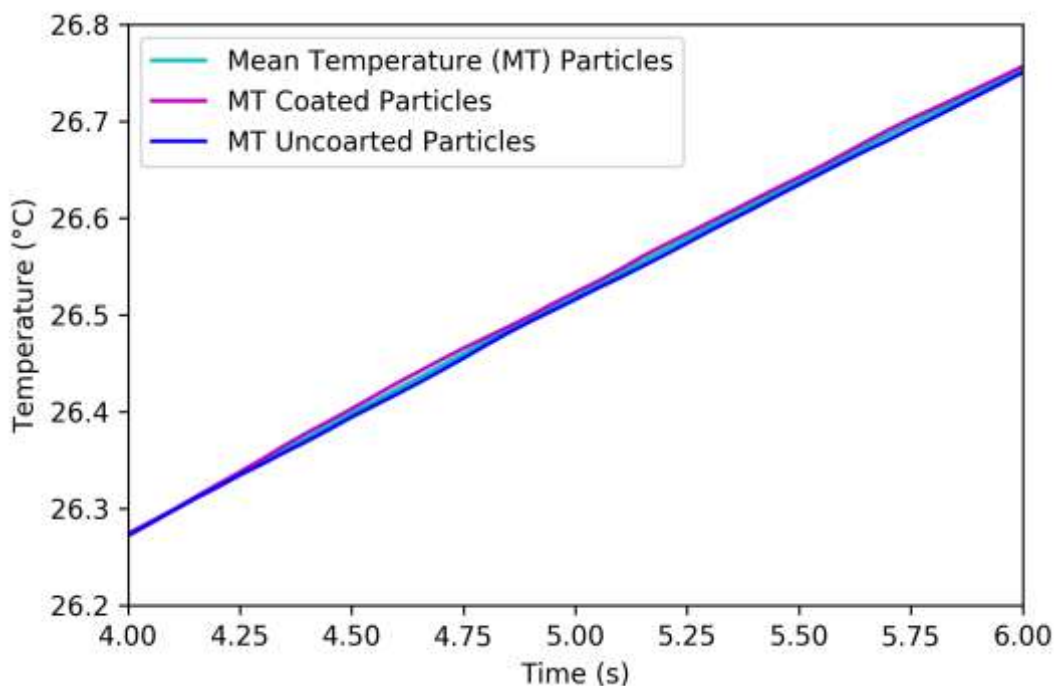


Figure 43: Change of the temperature over time of the coated particles, uncoated particles and the mean particle temperature in Case 9 (30°C)

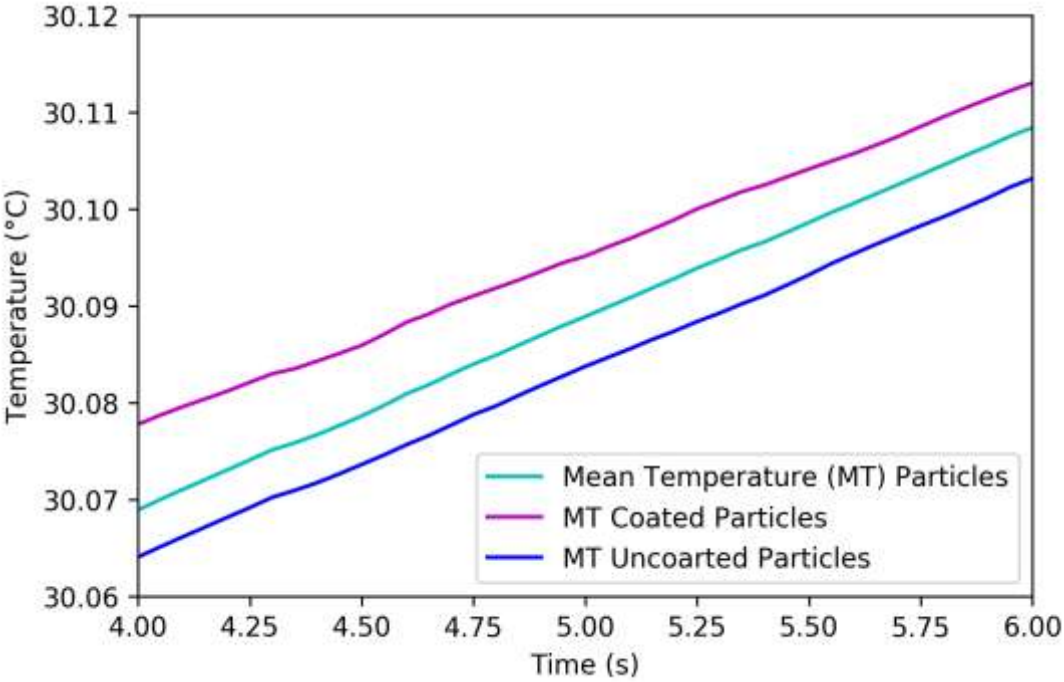
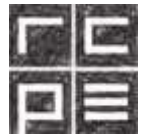


Figure 44: Change of the temperature over time of the coated particles, uncoated particles and the mean particle temperature in Case 12 (30°C)



#### 8.4.6.1.1 45°C: Case 11 (initial wall temperature 45°C) & Case 8 (initial wall temp. 30°C)

In Case 11 and Case 8 the difference between the initial wall temperatures is well illustrated. The influence of the initial wall temperature of 45°C in Case 11 is apparent since the particles that collide with the wall have a smaller temperature gradient than in Case 8 with lower initial wall temperature (30°C). It is reasonable that the difference between the 2 Cases is that Case 11 reflects 10 seconds of an already running process and Case 8 simulates the warm up of the fluid bed coater.

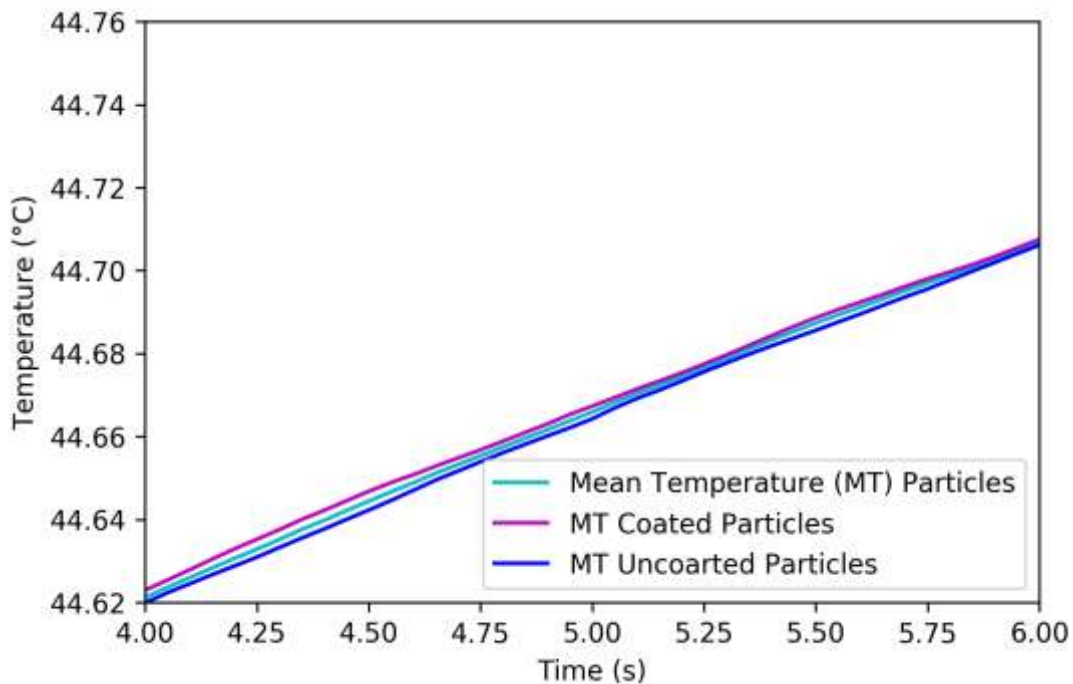


Figure 45: Change of the temperature over time of the coated particles, uncoated particles and the mean particle temperature in Case 8 (45°C)

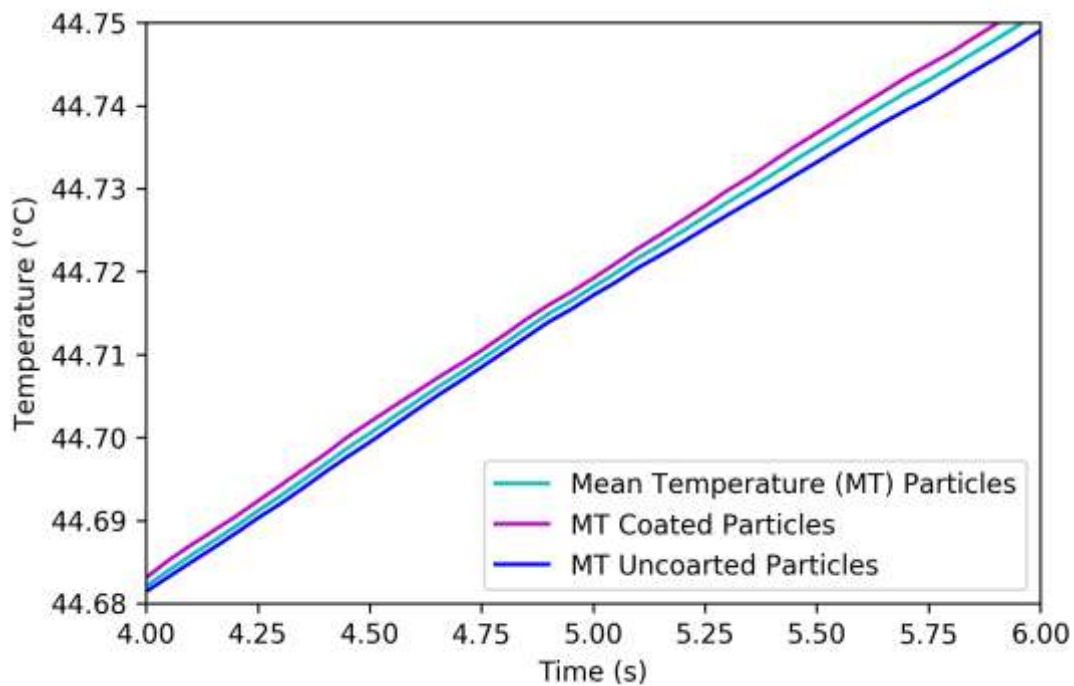
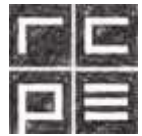


Figure 46: Change of the temperature over time of the coated particles, uncoated particles and the mean particle temperature in Case 11(45°C)

#### 8.4.6.2 60°C: Case 5 (initial wall temperature 30°C) & Case 13 (initial wall temperature 60°C)

To further emphasize the importance of initial parameters, the initial wall temperatures in Case 5 and Case 13 had a difference of 30°C. In Figure 47 the coated particles even lose temperature because the amount of coating liquid is so small (around  $7.5 \times 10^{-11}$  litre/particle) and the spray liquid impact accelerates the particles and due to this more wall contacts lowers their temperature. As compared to Figure 48 where the coated particles have higher temperature than mean or uncoated particle temperature.

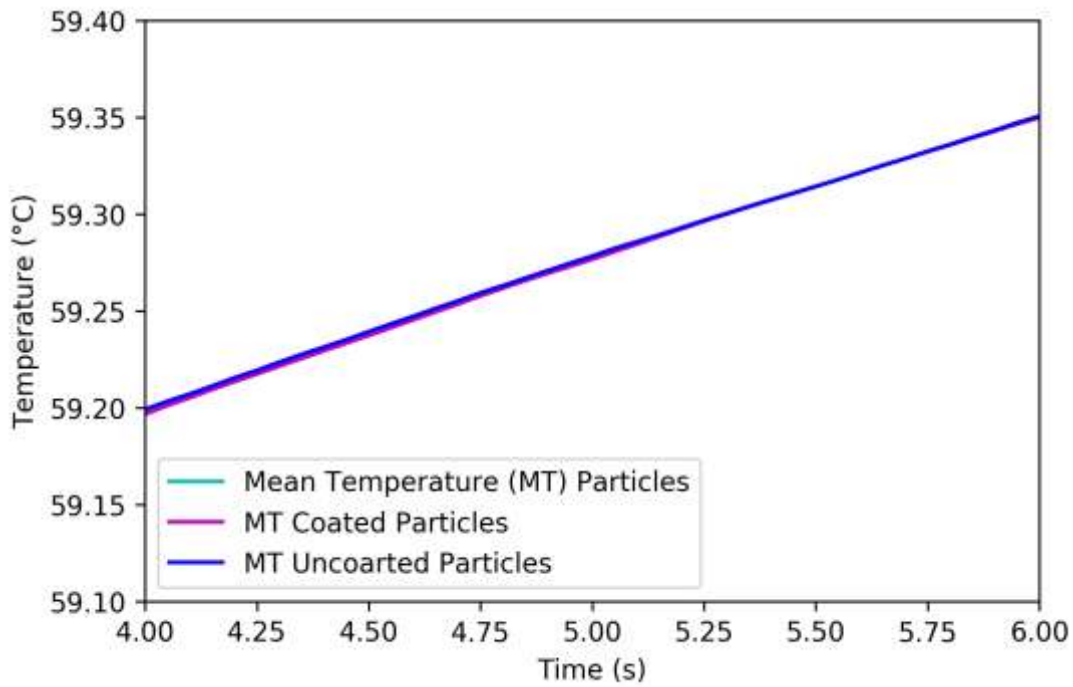
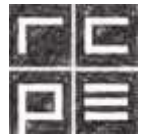


Figure 47: Change of the temperature over time of the coated particles, uncoated particles and the mean particle temperature in Case 5(60°C)

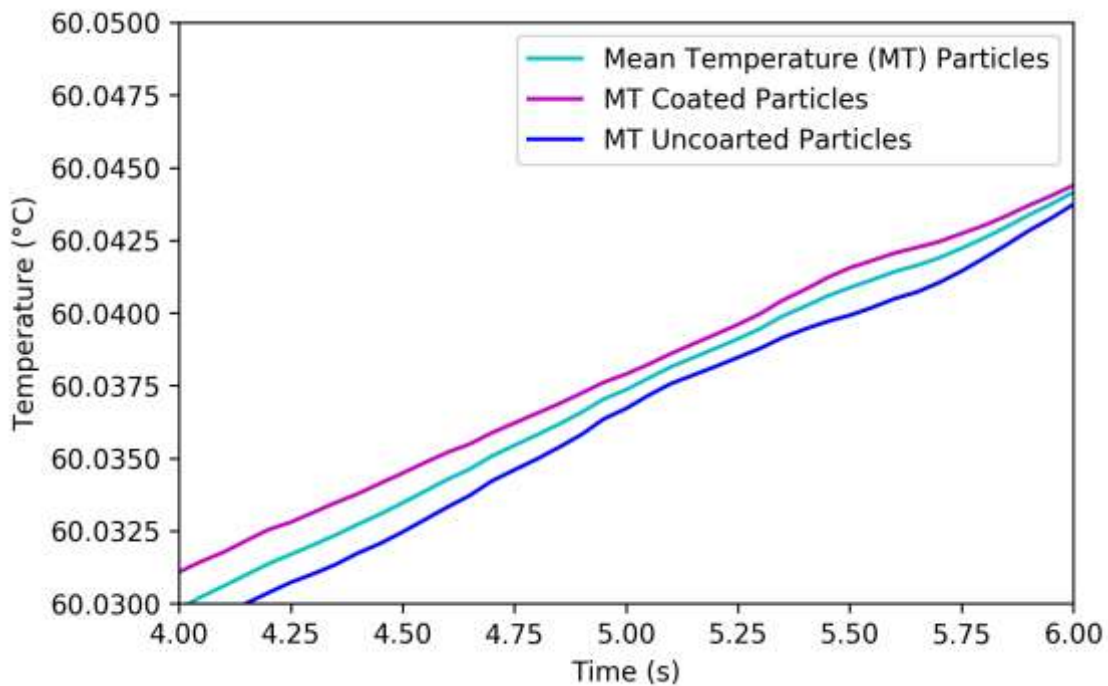
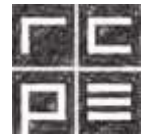


Figure 48: Change of the temperature over time of the coated particles, uncoated particles and the mean particle temperature in Case 13(60°C)

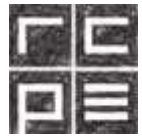


## 9 Summary

This thesis was a verification study for a fluid bed hot melt coating process with the CFD-Software AVL Fire and the in-house DEM-Software XPS. The experiments on the Innojet Ventilus V2.5 revealed a significant connection between airflow temperature and crystal morphology of Tristearin. In the experiments with the Tristearin-Polysorbat 65 mixture the temperature had no influence on the crystal lattice, because the transformation of the crystallized  $\alpha$ -form of Tristearin to  $\beta$ -form was immediately induced by Polysorbate 65. After the analysis of the crystal structure the microcapsules were tested for the API release. The studies revealed that the crystal morphology of pure Tristearin does not have an influence on the release of the coated NAC from microcapsules but the introduction of an emulsifier (Polysorbate 65) changes the system drastically.

The process was simulated with more than  $13 \cdot 10^6$  particles on AVL Fire and the DEM code XPS. The mixing behaviour in the fluid bed was investigated and it was found that the mixing is consistent for all airflow rates. Furthermore the airflow and the different initial temperatures of particles and the geometry grid showed big influence on the outcome. The difference in initial grid temperatures even made a difference in the coating analysis due to the fact that the coated particles were cooled further by the wall- and particle-particle contacts due to their higher speed (coated particles were accelerated by the spray).

It was showed that the CFD-DEM coupling could reproduce the results of the morphology studies and give an insight in a very complex particle mixing and temperature exchange system.

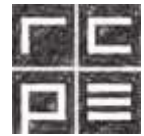


## 10 Outlook

For future simulations a solidification enthalpy model should be implemented to further improve the accuracy of the fluid-particle system. Using such a model it could be possible to calculate more complex morphologies with narrower crystal formation temperatures or also with degradation product analysis.

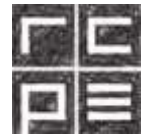
Further there should be more work done on the heat transfer models to increase accuracy of prediction and also to allow spray drying of the coating tablets to happen.

The validation process only made a small step with this work but gave a prospect for future work on the topic of CFD-DEM simulations and the possibilities within.

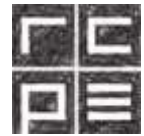


## 11 Literature

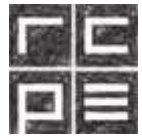
- Çengel, & Boles. (2014). *Thermodynamics: An Engineering Approach*. North Carolina State University: McGraw-Hill Education.
- Achanta, Adusumilli, James, & Rhodes. (1997). *Development of Hot Melt Coating Methods*. Kingston, Rhode Island: University of Rhode Island.
- Atkins, & Jones. (2010). *Chemical Principles*. New York: W.H. Freeman and Company.
- Becker, K. (2016). Hot melt coating with lipid-based excipients Development of a solvent-free technology for the coating of multiparticulate drug delivery systems . Graz: Submitted to the Department of Pharmaceutical Technology of the University of Graz .
- Becker, Saurugger, Kienberger, Lopes, Haack, Köberle, et al. (2016). Advanced stable lipid-based formulations for a patient centric product design . *International Journal of Pharmaceutics* , 136-149.
- Berger, Aftosmis, & Murman. (2005, May). Analysis of Slope Limiters on Irregular Grids. *NAS Technical Report* .
- Bicanic. (2007). Discrete element methods. In Stein, d. Borst, & Hughes, *encyclopedia of computational mechanics* (pp. 307-339). University of Michigan: Wiley.
- Bose, & Bogner. (2007). *Solventless pharmaceutical coating processes: a review*. Storrs, CT, USA: Pham Dec Technol.
- Britannica, E. o. (2016, Oktober 25). *www.britannica.com*. Retrieved Oktober 29, 2018 from <https://www.britannica.com/science/Coulomb-force>
- Brubach, Jannin, O., Mahler, Bourgaux, Lesieur, & Roy. (2004). *Structural and Thermal Characterization of Mono- and Diacyl Polyoxyethylene Glycol by Infrared Spectroscopy and X-ray Diffraction Coupled to Differential Calorimetry*. Chatenay Malabry, France: Journal of physical chemistry.
- Butt, & Kappl. (2008, November 1). Normal capillary forces . *Advances in Colloid and Interface Science* , pp. 48-60.
- Chapman. (1961). *The polymorphism of glycerides*. Cambridge: ACS Publications.
- ChemIDplus. (n.d.). *chem.nlm.nih.gov*. Retrieved Oktober 28, 2018 from <https://chem.nlm.nih.gov/chemidplus/rn/9005-71-4>
- Choi, & Joseph. (2001). Fluidization by lift of 300 circular particles in plane Poiseuille flow by direct numerical simulation. *Journal of Fluid Mechanics* 438 , 101-128.
- Condra. (2001). *Reliability Improvement with Design of Experiments*. New York: Marcel Dekker, Inc. .
- Correns. (1949). *Einführung in die Mineralogie*. Göttingen: Springer.
- Coupland. (2001). *Ultrasonic Characterization of Lipid Crystallization*. Department of Food Science. Pennsylvania State University: AOCS .
- Crow. (2006). *Multiphase Flow Handbook*. Boca Raton: Taylor&Francis.
- Cundall, & Stack. (1979). A discrete numerical model for granular assemblies. *Geotechnique* , 47-65.
- Deen, Annaland, V. S., Hoef, V. d., & Kuipers. (2005). Review of discrete particle modeling of fluidized beds. *Chem. Eng. Sci.* 62 , 28-44.
- Del Cid, L. (2015). A Discrete Element Methodology for the Analysis of Cohesive Granular Bulk Solid Materials. Colorado: Colorado School of Mines.
- Di Renzo, A., & Di Maio, F. (2003). Comparison of contact-force models for the simulations of collisions in DEM-based granular flow codes. *Chemical Engineering Science* , 17.



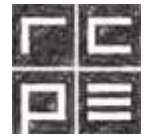
- Editorial-Team. (2015, Juli 28). *laboratoryinfo.com*. Retrieved Oktober 22, 2018 from <https://laboratoryinfo.com/wp-content/uploads/2015/07/High-performance-liquid-chromatography-hplc.jpg>
- Elkordy, A. A. (2013). *APPLICATIONS OF CALORIMETRY IN A WIDE CONTEXT*. Croatia, Rijeka: InTech.
- Ergun. (1952). Fluid flow through packed columns. *Chemical Engineering and Processing* 48 , 89-94.
- Ferziger, & Peric. (2002). *Computational Methods for Fluid Dynamics*. Berlin: Springer.
- Gidaspow. (1994). Continuum and kinetic theory discription. In Gidaspow, *Multiphase flow and fluidization*. Chicago, Illinois: Academic Press, Inc. .
- Gittings, Turnbull, Roberts, & Gershkovich. (2013). Dissolution methodology for taste masked oral dosage forms. *Journal of Controlled Release* 173 , 32–42.
- Govender, Wilke, Wu, Rajamani, Khinast, & Glasser. (2018). Large-scale GPU based DEM modeling of mixing using irregularly shaped particles. *Advanced Powder Technology* , 2476-2490.
- Höhne, H. F. (2003). *Differential Scanning Calorimetry*. Berlin-Heidelberg: Springer.
- Hager. (1995). *Hagers Handbuch der Pharmazeutischen Praxis: Band 9: Stoffe P-Z*. (G. D.-W. Franz v. Bruchhausen, Ed.) Springer.
- Hertz. (1882). Über die Berührung fester elastischer Körper. *Journal für reine und angewante Mathematik* , 156-171.
- Heydt, & Schiedermaier. (2019). *Thieme RÖMPP*. Retrieved March 7, 2019 from <https://roempp.thieme.de/roempp4.0/do/data/RD-07-02302>
- Hinkes. (1978). Solvent Film Coating: Aqueous vs. Organic . *Midwest Regional Meeting, Academy of Pharmaceutical Sciences* (p. 11). Madison, Wisconsin : Wisconsin Alumni Research Foundation .
- Huilina, & Gidaspow. (2003). Hydrodynamics of binary fluidization in a riser: CFD simulation using two granular temperatures. *Chem. Eng. Sci.* 58 , pp. 3777-3792.
- Hussain, Sastry, & Raju. (1991). *Molecular weight averages as criteria for quality assessment of heated oils and fats*. Hyderabad, India: Springer.
- IROGroup. (n.d.). <http://www.irosurfactant.com>. Retrieved Oktober 29, 2018 from <http://www.irosurfactant.com/Tween-65.htm>
- Jajcevic, Siegmann, Radeke, & Khinast. (2013). Large-scale CFD–DEM simulations of fluidized granular systems . *Chem. Eng. Sci.* , 298-310.
- Jannin, V., & Cuppok, Y. (2012). *Hot-melt coating with lipid excipients*. Gattefossé S.A.S., 36 chemin de Genas: ScienceDirect.
- Jones, & Percel. (1994). *Coating of multiparticulates using molten materials*. New York.
- Ketterhagen, Am Ende, & Hancock. (2008). *Process Modeling in the Pharmaceutical Industry using the Discrete Element Method*. Groton, Connecticut: Wiley InterScience.
- Krämer, J., Grady, L. T., & Gajendran, J. (2005). Historical Development of Dissolution Testing . In J. Dressman, & J. Krämer, *Pharmaceutical Dissolution Testing* (pp. 1-65). New York: Taylor & Francis Group .
- Kulah, & Kaya. (2010). *Investigation and scale-up of hot-melt coating of pharmaceuticals in fluidized beds* . Turkey: Elsevier.
- Lide, D. R. (2005). *CRC Handbook of Chemistry and Physics*. Boca Raton, FL: CRC Press.
- Lomax, Pulliam, & Zingg. (1999). *Fundamentals of Computational Fluid Dynamics*. NASA Ames Research Center: Springer.
- Lopes, Becker, Stehr, Lochmann, Haack, Zimmer, et al. (2015, September). Role of Lipid Blooming and Crystallite Size in the Performance of Highly Soluble Drug-Loaded Microcapsules. *Journal of Pharmaceutical Sciences* , 4257-4265.



- Lyngfelt, Leckner, & Mattisson. (2000). Department of Energy Conversion, Chalmers University of Technology. Göteborg, Sweden: Elsevier.
- Malone, & Xu. (2008, July 15). Determination of contact parameters for discrete element method simulations of granular systems. Leeds: Elsevier.
- Mindlin, & Deresiewicz. (1953). Elastic spheres in contact under varying oblique forces. *Journal of Applied Mathematics* , 327-344.
- Morrison. (2016). *Data Correlation for Drag Coefficient for Sphere*. Department of Chemical Engineering . Michigan: michigan technological University.
- Munson, Okiishi, Huebsch, & Rothmayer. (2013). *Fundamentals of Fluid Mechanics*. Ames, Iowa: Wiley.
- Nakamura, Iwasaki, & Watano. (2006). *Numerical Simulation of Film Coating Process in a Novel Rotating Fluidized Bed*. Osaka Prefecture University: Chem. Pharm. Bull.
- NASA. (2016). *grc.nasa.gov*. Retrieved May 28, 2018 from <https://www.grc.nasa.gov/WWW/k-12/airplane/dragSphere.html>
- NIST. (n.d.). *nist.gov*. Retrieved Oktober 29, 2018 from <https://webbook.nist.gov/cgi/cbook.cgi?ID=C616911&Units=SI>
- NIST. (n.d.). *nist.gov*. Retrieved Oktober 29, 2018 from <https://webbook.nist.gov/cgi/cbook.cgi?Name=tristearin&Units=SI>
- Pashaie, M. (2014, June 13). *slideshare.net*. Retrieved March 25, 2019 from <https://www.slideshare.net/MokhtarPashaie/dsc-tga>
- Patil, Chafle, Khobragade, Umathe, & Avari. (2011). *Evaluation of hot melt coating as taste masking tool*. Nagpur, India: International Research Journal of Pharmacy.
- Pepiot, & Desjardins. (2012). Numerical analysis of the dynamics of two- and three-dimensional fluidized bed reactors using an Euler-Lagrange approach. *Powder Technologie 220* , 104-121.
- PubChem. (n.d.). *PubChem Compound Database*. Retrieved March 07, 2019 from National Center for Biotechnology Information : <https://pubchem.ncbi.nlm.nih.gov/compound/12035>
- Richardson. (1971). Incipient fluidization and particulate systems. In Davidson, & Harrison, *Fluidization*. New York: Academic Press.
- Romanco Innojet. (2012, 02 03). Dokumentation Innojet Ventilus V2.5. Steinen.
- Sans, P. D. (2015). A self optimizing synthetic organic reactor system using real-time in-line NMR spectroscopy. *Chemical Science* , 1258-1264 .
- Schnabelegger, & Singh. (2013). *The SAXS Guide*. Graz, Steiermark: Anton Paar GmbH.
- Seo, Holm, & Schaefer. (2002). *Effects of droplet size and type of binder on the agglomerate growth mechanisms by melt agglomeration in a fluidised bed*. European Journal of Pharmaceutical Sciences.
- Seville, Willett, & Knight. (2000, April 28). Interparticle forces in fluidisation: a review. *Powder Technology 113* , pp. 261-268.
- Shu. (1988, November 6). Total-Variation-Diminishing time discretizations. *Society for Industrial and Applied Mathematics* , 12.
- Sonnendrücker. (2013, July 16). Numerical methods for hyperbolic systems. (M.-P.-I. f. Plasmaphysik, Ed.) München.
- Sonntag, N. O. (1979). *Fat splitting*. Taminent, PA: Springer.
- Sudke, & Sakararakar. (2013). *Lipids - An Instrumental Excipient In Pharmaceutical Hot Melt Coating*. India: International Journal of PharmTech Research.
- Sweby. (1984, October 5). High resolution schemes using flux limiters for hyperbolic conservation laws. *Society for Industrial and Applied Mathematics* , 17.



- Tan, Salman, & Hounslow. (2006). *Kinetics of fluidised bed melt granulation I: The effect of process variables*. Chemical Engineering Science.
- Teunou, & Poncelet. (2002). *Batch and continuous fluid bed coating - review and state of the art*. Nantes Cedex 3, France: Journal of Food Engineering.
- Toschkoff, & Khinast. (2013). *Mathematical modeling of the coating process*. Graz: Elsevier.
- Villa, Bertin, Cotabarren, Pina, & Bucala. (2016). *Fluidized bed melt granulation: Coating and agglomeration kinetics and growth regime prediction*. Bahia Blanca, Argentina: CrossMark.
- Wen, & Yu. (1966). Mechanics of fluidization. *A.I.Ch.E. Series 62*, 100-111.
- Weston, A., & Brown, P. R. (1997). *HPLC and CE*. California, San Diego: Academic Press.
- World Health Organization. (2006). *Stability testing of active pharmaceutical ingredients and finished pharmaceutical products*. World Health Organ Tech Rep Ser.
- Wunderlich. (2005). *Thermal Analysis of Polymeric Materials*. Knoxville, TN: Springer.
- Zalilah. (2016, June). <https://people.utm.my/>. Retrieved February 20, 2019 from <http://fcee.utm.my/zalilah/files/2016/06/Chapter-3-Motion-of-Particles.pdf>
- Zhang, e. a. (1999b). Dynamic behavior of collision of elastic spheres in viscous fluids. *Powder Technology 106*, 98-109.
- Zhu, Zhou, Yang, & Yu. (2007). *Discrete particle simulation of particulate systems: Theoretical developments*. Centre for Simulation and Modelling of Particulate Systems, School of Materials Science and Engineering. New South Wales: Elsevier.
- Zierep, & Bühler. (2010). *Grundzüge der Strömungslehre*. Wiesbaden: Vieweg+Teubner.



## 12 List of Figures

Figure 1: Geldart chart for characterization of particle fluidization behaviour in the 4 groups A, B, C, D. With the particle diameter [ $d_p$ ] ( $\mu\text{m}$ ) on the x-axis and the density difference between particle $\rho_P$ and gas $\rho_{Pg}$ $\text{kg}/\text{m}^3$ (Crow, 2006) .....	4
Figure 2: Dimensionless Grace chart for upward flow regime through solid particles to characterize the state of a fluidized bed (Crow, 2006) .....	5
Figure 3: Principal scheme of a fluid bed coating process with a top spray nozzle (Teunou & Poncelet, 2002) .....	8
Figure 4: The 4 different types of batch fluid beds: (a) top spray; (b) bottom spray; (c) wurster; (d) rotor with side spray (Teunou & Poncelet, 2002) .....	11
Figure 5: hexagonal ( $\alpha$ ), orthorhombic-perpendicular ( $\beta'$ ) and triclinic-parallel ( $\beta$ ) crystal lattice and a subcell to visualize the short spacing. (Modified from (Lopes, et al., 2015)) .....	18
Figure 6: Graphic of Newton's second law. Mass- and inertial forces acting on a particle in contact with another particle. (Zhu, Zhou, Yang, & Yu, 2007) .....	28
Figure 7: Linear spring-dashpot model of a particle colliding with a wall (Malone & Xu, 2008) .....	29
Figure 8: Comparison of the magnitude of inter-particle forces (Zhu, Zhou, Yang, & Yu, 2007) .....	30
Figure 9: Change of the drag coefficient of a smooth respectively a rough sphere with different Reynolds numbers (NASA, 2016) .....	32
Figure 10: Particle-Particle interactions with a soft sphere model (Jajcevic, Siegmann, Radeke, & Khinast, 2013) .....	35
Figure 11: Non linear contact law hysteresis (Del Cid, 2015) .....	38
Figure 12: CFD-DEM coupling scheme via AVL-Code-Coupling-Interface (Jajcevic, Siegmann, Radeke, & Khinast, 2013) .....	39
Figure 13: Innojet Ventilus V-2.5/1 with IHD Hot Melt Device (Becker K., 2016) .....	42
Figure 14: Excerpt from the P&ID of the Innojet Ventilus 2.5 (Romanco Innojet, 2012) ..	43
Figure 15: Chemical structure of N-acetylcysteine (NIST, nist.gov) .....	44
Figure 16: Structure of Tristearin (NIST, nist.gov) .....	45
Figure 17: Structure of Polysorbate (IROGroup) .....	45
Figure 18: N <sub>2</sub> (30°C) & N <sub>5</sub> (60°C) DSC curves. The exothermic transitions are in the negative y-direction. There is a distinct alpha peak, a recrystallization and a beta melting peak for N <sub>2</sub> and only a beta peak for N <sub>5</sub> and shows exactly the difference between alpha and beta morphology behaviour in the DSC .....	51
Figure 19: Coefficient plot significant influences on crystal structure (alpha-left, beta-right) .....	52
Figure 20: Contour Plot of the influencing parameters on the proportions of alpha (left) and beta (right) morphology .....	53
Figure 21: Mean dissolution of the triplicates in % over time for the experiments N1, N7, N18 with pure Tristearin and different temperatures .....	54
Figure 22: Dissolution in % over time for the experiments with Tristearin-Polysorbate 65 mixture .....	55
Figure 23: Coefficient plot of the Dissolution after 5 (right) and 30 minutes (left) .....	56
Figure 24: Contour plot for the dissolution after 5 minutes .....	57
Figure 25: Contour plot for the dissolution after 30 minutes .....	57
Figure 26: Examples for the CFD situations with Temperature (left) and Velocity (right) of the fluid flow .....	58

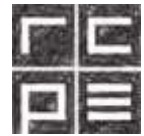


Figure 27: Detail of the fluid flow velocity of the CFD simulation geometry ..... 59

Figure 28: Comparison of the Cumulative distributions of NAC particles in experiment and simulation..... 60

Figure 29: Particle mean velocity magnitude after 1.5 seconds till 7.5 seconds for three different airflow speeds. .... 61

Figure 30 ..... 61

Figure 31: Mean mixing of the particles in radial direction over time ..... 62

Figure 32: Mixing of Case 13 (75m<sup>3</sup>/h) in radial direction after a) 2.20 seconds (initial position); b) 2.50 seconds; c) 2.70 seconds; d) 2.80 seconds; e) 3.00 seconds; f) 3.10 seconds..... 63

Figure 33: Development of the Lacey Index over time for 3 different airflow rates..... 64

Figure 34: Mean mixing of the particles in axial direction over time ..... 65

Figure 35: Mixing of Case 9 (50 m<sup>3</sup>/h) in horizontal direction after a) 3.10 seconds (initial position); b) 3.30 seconds; c) 3.50 seconds; d) 3.70 seconds ..... 66

Figure 36: Mixing of Case 13 (75 m<sup>3</sup>/h) in horizontal direction after a) 3.10 seconds (initial position); b) 3.30 seconds; c) 3.50 seconds; d) 3.70 seconds ..... 66

Figure 37: Change of temperature over time for the Cases 6 and Case 9 (25°C particle initial temperature) and Case 12 (30°C particle initial temperature) at 30°C grid temperature. .... 68

Figure 38: Change of temperature over time for Case 12 (30°C particle initial temperature) at 30°C grid temperature..... 68

Figure 39: Change of temperature over time for the Cases 11 and 8 with 45°C particle initial temperature and 30°C grid temperature for Case 8 and 45°C grid temperature for Case 11. .... 69

Figure 40: Change of temperature over time for the Cases 10 and 5 with 60°C particle initial temperature and 30°C grid temperature & of Case 13 with 60°C initial particle and initial grid temperature..... 70

Figure 41: Change of temperature over time for Case 13 with 60°C initial particle and initial grid temperature..... 71

Figure 42: Change of the temperature over time of the coated particles, uncoated particles and the mean particle temperature in Case 9 (30°C)..... 72

Figure 43: Change of the temperature over time of the coated particles, uncoated particles and the mean particle temperature in Case 12 (30°C) ..... 73

Figure 44: Change of the temperature over time of the coated particles, uncoated particles and the mean particle temperature in Case 8 (45°C)..... 74

Figure 45: Change of the temperature over time of the coated particles, uncoated particles and the mean particle temperature in Case 11(45°C) ..... 75

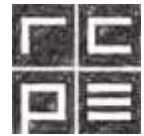
Figure 46: Change of the temperature over time of the coated particles, uncoated particles and the mean particle temperature in Case 5(60°C)..... 76

Figure 47: Change of the temperature over time of the coated particles, uncoated particles and the mean particle temperature in Case 13(60°C) ..... 76

Figure 48: QICPIC analysis of the NAC particle size distribution ..... 85

Figure 49: Cumulative size distribution of the NAC particles ..... 86

Figure 50: WAX study of N18 (45°C). The alpha configuration seen in the DSC could not be confirmed by the WAX. .... 86



### 13 Appendix

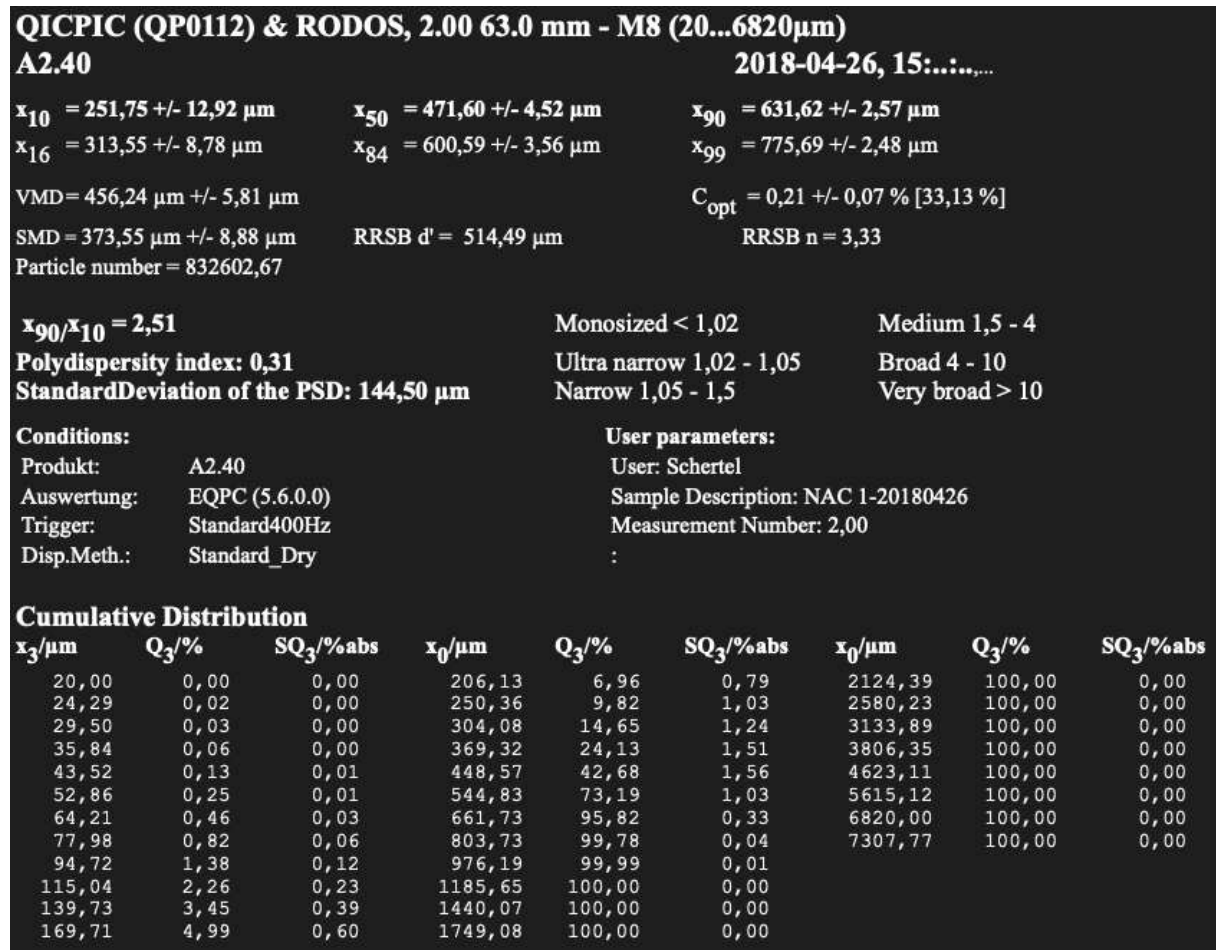
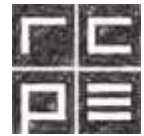


Figure 49: QICPIC analysis of the NAC particle size distribution



## CFD-DEM Simulation of a Hot Melt Fluidized Bed Coating Process

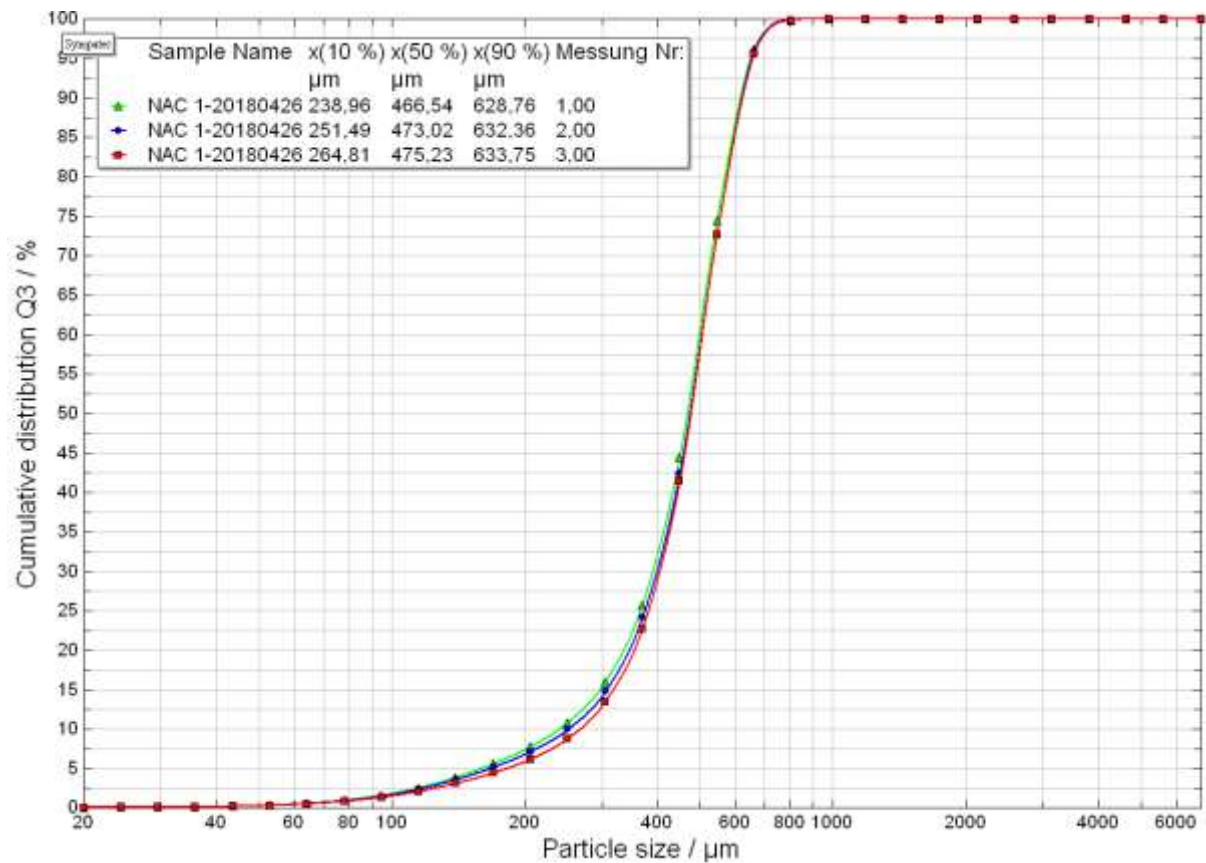


Figure 50: Cumulative size distribution of the NAC particles

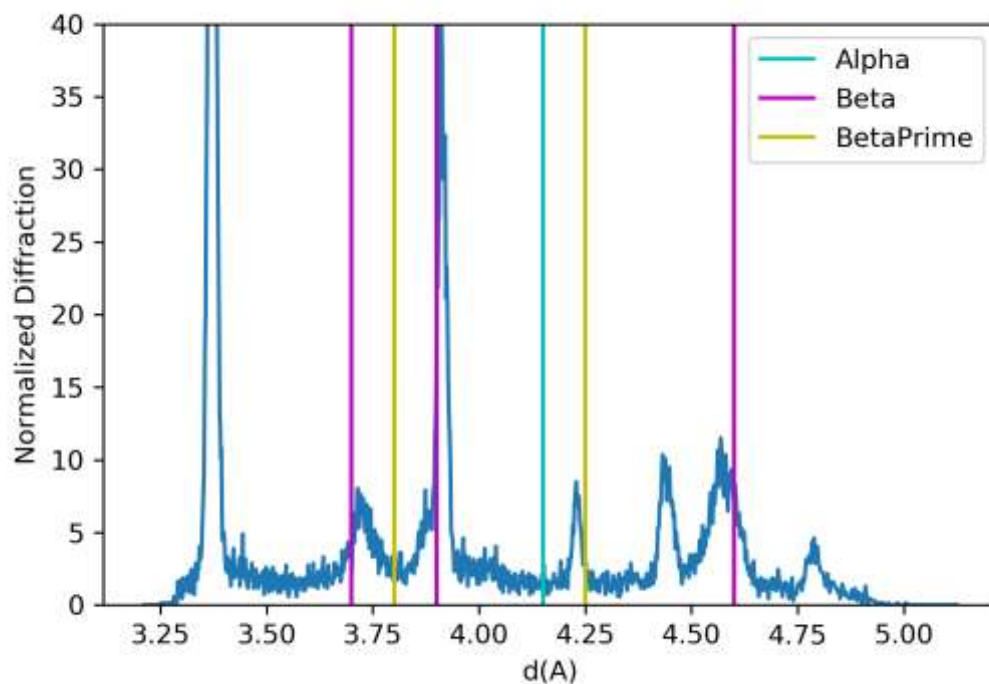


Figure 51: WAX study of N18 (45°C). The alpha configuration seen in the DSC could not be confirmed by the WAX.